Computational Study of Covalency and Complexation in Actinides using Static and Dynamic Simulation and Topological Density Analysis

Ian de Joncheere Kirker

A dissertation submitted in partial fulfillment

of the requirements for the degree of

Doctor of Philosophy

of

University College London.

Department of Chemistry

University College London

June 21, 2013

I, Ian de Joncheere Kirker, confirm that the work presented in this thesis is my own. Where information has been derived from other sources, I confirm that this has been indicated in the work.

Abstract

The separation of minor actinides such as americium and curium from other actinide and lanthanide-bearing components of used nuclear fuel is a necessary part of post-processing and recycling this fuel into storable components and new fuel material. Separation ratios can be optimised using a comprehensive understanding of the differences between these elements and their aqueous chemistry.

This work uses computational simulation to investigate bonding behaviour and covalency differences between the actinides in the (III) and (IV) oxidation states for several ligand systems: first, actinide (III) tris-cyclopentadienyl compounds ($AnCp_3$), comparing with similar work on actinide (IV) tetrakis-cyclopentadienyl compounds, and second, a group of related actinide (IV) betaketoiminate systems ($An(^{Ar}NCRCHCRO)_4$). Multiple methods are used and compared, including common wavefunction-based methods such as Mulliken and Natural Population Analysis, as well as topological density analysis methods based on the quantum theory of atoms in molecules (QTAIM). Common interpretations give misleading results, and QTAIM-based methods more clearly show the decreasing covalent interaction across the actinides.

A study of the aqueous behaviour of plutonium (IV) follows, first obtaining molecular hydrate and hydroxide complex geometries, and then inserting two of these into a dynamic simulated solution. Molecular complex free energies are shown to produce results that are in agreement with experimentally determined coordination number, and matching with trends towards dehydration with increasing hydrolysis degree found in other metal hydroxide complexes. Dynamic simulation results suggest a thermal barrier to equilibration which may be an artifact of the method used. Molecular complexes are also inspected using QTAIM methods, which find an exponential relationship between many of the properties and bond length for the Pu-O bond, and suggest partial multiple bond character.

Acknowledgements

I should first acknowledge the support of the NNL in making this work possible, and in particular Helen Steele and Mark Sarsfield.

Many, many thanks must go to my supervisor, Professor Nikolas Kaltsoyannis, for giving me the opportunity to work in his group, and for the myriad ways he has supported and assisted me over the course of my doctoral studies.

I should also like to thank David Weir, James Weaver, Kathleen Dawes, and many other ex-ICSF members, for discussions, distractions, guidance, gaming, and sanity-sustaining friendships, and to thank my fellow occupants of the G19 office, including especially Andrew Kerridge, Krishna Hassomal Birjkumar, Claire Skipper, and Rosemary Coates, for making it an inviting, interesting, supportive, and occasionally even fun place to work, as well as a frequent source of delicious baked goods.

Thanks also go to Laura Kirker and Bob Slack, for putting up with me more than they really have to.

Finally, I should acknowledge the use of the UCL Legion High Performance Computing Facility (Legion@UCL) and the UCL Chemistry Department's Xenon cluster, which have both been instrumental in the completion of this work. Additionally, this work made use of the facilities of HECToR, the UK's national high-performance computing service, which is provided by UoE HPCx Ltd at the University of Edinburgh, Cray Inc and NAG Ltd, and funded by the Office of Science and Technology through EPSRC's High End Computing Programme.

Contents

List of Figures

List of Tables

Chapter 1

Introduction & Background

Nuclear power generation has, since the first reactors, produced a significant quantity of intermediate and high-level actinide-bearing radioactive waste products – some of which are sufficiently radioactive to make the heat generated a concern, and some of which will remain radioactive for tens of thousands of years. As the pressing need for long-term solutions mounts, understanding the chemistry of the actinides, and the lanthanide fission products which accompany them, becomes vital to the design and implementation of novel methods for producing more manageable waste, both in quantity and quality.

1.1 Lanthanides and Actinides

The early actinides have extremely complex chemistry, the majority having many accessible oxidation states and readily undergoing disproportionation in aqueous solution[1, 2, 3]. Figure 1.1 shows the wide range of oxidation states that are accessible to the actinide series. As the $5f$ shell contracts, fewer states are available, approaching purely hard An^{3+} ionic behaviour, but latter actinides past curium that behave this way are not a major component of waste [2].

When actinide fuel waste is removed from a reactor, it contains a mixture of synthesised elements, of varying levels of radioactivity, and these must be separated and treated according to both their re-usability, and their storage needs. Early actinides can be separated from later actinides, by their different bonding properties, typically removing uranium and plutonium components using a two-phase aqueous/kerosene extraction procedure commonly known as the PUREX process. Lanthanides and so-called 'minor' actinides, americium and curium, however, can be

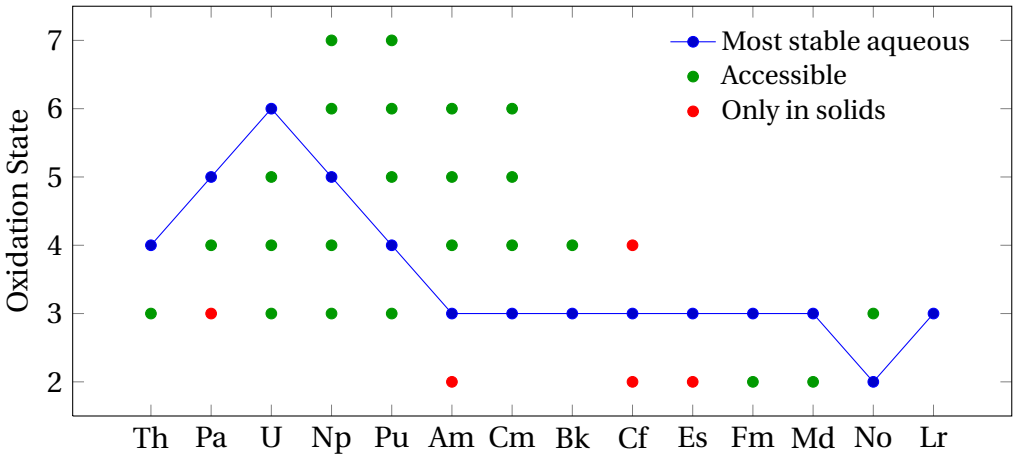

Figure 1.1: Accessible oxidation states for the actinides. Reproduced from [1].

difficult to separate from each other, as they have very similar chemistry. Such separations make it possible to handle differing handling requirements separately: the synthetic lanthanide isotopes are sufficiently radioactive as to generate heat that must be accounted for in storage strategies, while the americium and curium have much longer half-lives (> 100 years, and orders of magnitude longer for the daughter products) and thus warrant longer-term storage methods. These heavy elements are also α emitters, and thus complexities produced by associated radiation and helium generation must be accounted for in storage design.

To attempt to design methods that can be used to separate actinide and lanthanide ions, then, a sound understanding of the differences in chemistry between them must be gained. Lanthanides in most bonding situations are assumed to be strongly ionic, due to the behaviour of the $4f$ orbital set – the lack of radial nodes in the first shell of a given angular momentum results in more highly contracted orbitals than for any of the subsequent shells, which experience a so-called 'primogenic repulsion' from the shells with a lower principal quantum number [4]. The highly contracted $4f$ orbitals are thus spatially confined to a region that makes them largely unavailable for bonding [1], and thus the majority of chemistry involves hard ionic bonding, with Ln^{3+} and Ln^{2+} ions[1], though cerium is known both to be tetravalent and to engage in bonding with slightly more complex character [5].

Conversely, the bonding in actinides principally derives from the $5f$ and $6d$ orbitals. These are much more available for bonding, especially in the early actinides,

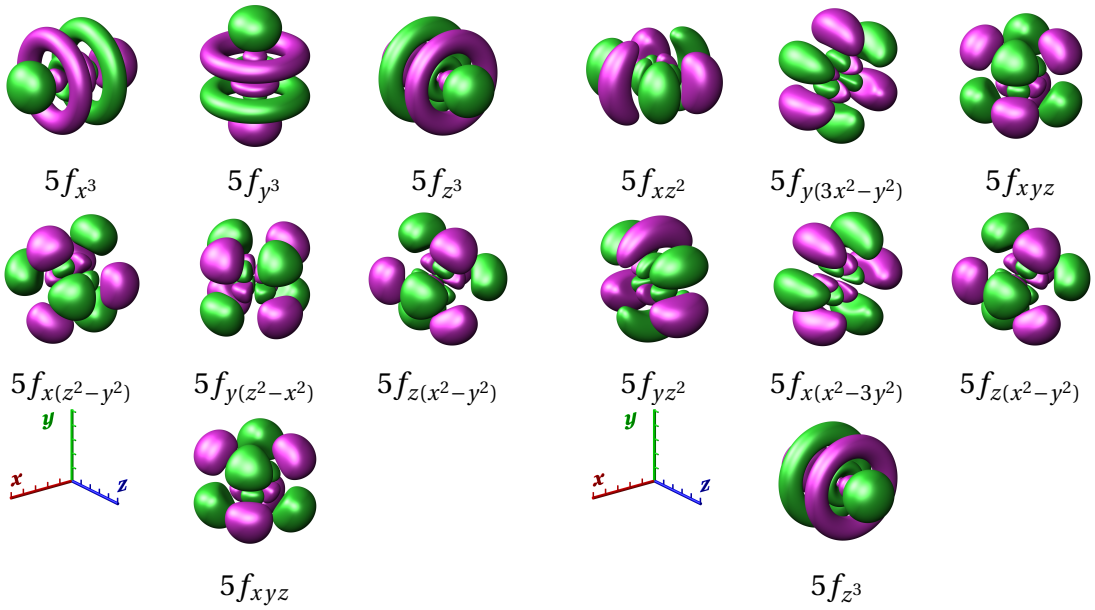

(a) The cubic set **(b)** The general set

Figure 1.2: The two common ways of forming the 7 hydrogenic ($Z = 1$) $5f$-orbitals: the cubic set, and the general set. Note that several orbitals are shared between the two, and that all the orbitals have one radial nodal surface, and three angular nodal surfaces. Green represents the positive phase surface, and purple the negative phase surface, $\phi(x, y, z) = \pm 0.0015$. Axis ticks mark 10 Bohr increments.

allowing the more complex array of chemistry [1, 6]. Uranium in particular is known to be able to form more covalent bonds using both the $5f$ and $6d$ orbitals in bonding where a lanthanide would, in most cases, bond essentially ionically.

The use of f orbitals for bonding generates some bonding modes unique to these elements – while octahedral geometries seen in transition metals are possible, coaxial alignment of the three nodal surfaces (see *e.g.* $5f_{y(3x^2-y^2)}$, figure 1.2) also promotes hexagonal planar and bipyramidal geometries, and other arrangements involving hexagonal arrangements.

The 8-lobed orbital forms shown in figure 1.2 also allow the 'uranocene'-type D_{8h}-symmetric structure shown in figure 1.3, which is unique to elements with f-valence orbitals, and forms by the interaction of the 8-lobed cubic f orbitals with the various harmonics of the π system of the ring. These compounds are observed for both lanthanides and actinides, and the complex multiconfigurational character of the cerium complex, $Ce[\eta^8\text{-}C_8H_8]_2$, has made it the focus of much computational study [5]. In experimental actinide studies, these compounds are known to be accessible for actinides from thorium through plutonium [1].

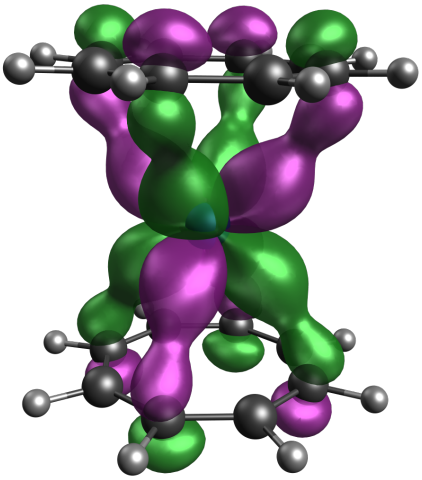

Figure 1.3: An actinide 'sandwich' structure with two octatetraenyl anions, showing one of the possible orbitals composed of an 8-lobed f orbital and two ligand orbitals.

In separating minor actinides from earlier actinides, ligand design typically uses soft, polarisable ligands that emphasise covalent bonding character, to maximise non-ionic differences in bonding strength. Examples of extractants in use include the ligands known as BTBP (figure 1.4a) which uses soft aromatic nitrogen atoms as the chelating atoms, and TODGA (figure 1.4b), which uses steric characteristics and slight differences in metal-oxygen binding to enhance selectivity. Complexes formed with these can then be extracted from an aqueous into an organic phase[2].

As all waste used with radioactive isotopes itself becomes radioactive waste, a common design goal in such design efforts is to use only carbon, hydrogen, oxygen, and nitrogen, as such substances can be incinerated without leaving either radioactive solid waste which would then have to be contained and managed, or gaseous waste containing elements which would present an environmental hazard. This excludes elements which would otherwise be excellent choices for soft, possibly discriminatory bonding donors, such as sulphur or phosphorus, as well as yet heavier elements such as selenium, germanium, or even tellurium, all of which are known to form covalent bonds to actinides [7, 8, 9, 10]. Phosphate in particular is a long-standing staple of plutonium and uranium extraction processes – tri(n-butyl) phosphate ((n−BuO)$_3$P=O) has been used to great effect since very early work with plutonium in 1944 [2], and is a key part of the PUREX process.

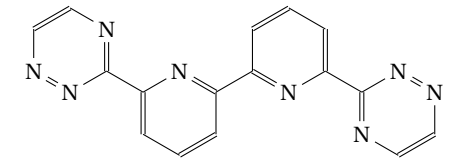

(a) BTBP

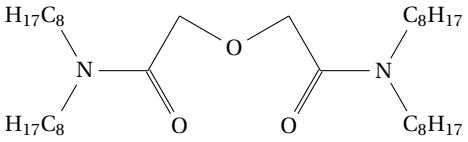

(b) TODGA

Figure 1.4: Two notable extractant molecules – *bis*-triazinyl bipyridine (BTBP), and tetraoctyl diglycolamide (TODGA).

Even with the extensive study of the actinides for uses in nuclear energy, the combination of difficulties in working with actinides experimentally, the relatively recent synthesis of the majority of elements in this group, and their multifaceted complex valence orbital behaviour, result in actinide chemistry still having much unexplored territory. For example, mechanistic studies for common reactions [3, 11, 12], discovery and analysis of new ligand bonding modes, and refining techniques for spectroscopic probing of actinide compounds [13] remain very much current concerns, along with even, as seen later in this work, relative bonding behaviour of these elements, instrumental to the design of new extractants.

As recently as this year, in the field of actinide bonding modes, the first non-matrix-isolated synthesis was published of a U(V)≡N bond, a highly reactive moiety that required significant steric coverage (figure 1.5) and dry nitrogen atmosphere to remain stable[14]. This represents the opening of a significant new avenue in multiple bonds to uranium, which is vastly dominated by uranyl ($[O{=}U{=}O]^{+/2+}$) chemistry due to the propensity for uranium to form this species in aqueous solution. Additionally, the uranium-nitrogen bond in this compound is thought to be similar to that in solid uranium mononitride, which has been used as a nuclear fuel [15] and has many desirable properties for wider use in reactors [16].

Actinides are also a fertile ground for several burgeoning fields, including molecular magnets, due to their spatially extensive orbitals that can propagate spin-polarisation and superexchange over an extended bond network[17], yielding new types of extended continuously covalent bond structure, going from

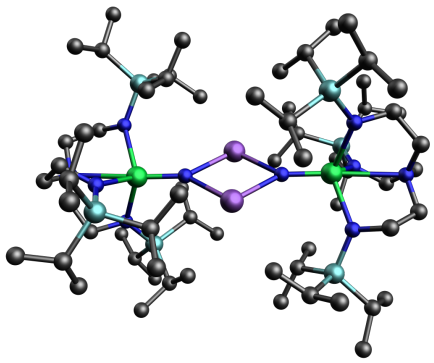

Figure 1.5: $[U(\mu{-}N)(\mu{-}Na)(Tren^{TIPS})]_2$, the first room-temperature molecular species produced with a formal triple UN bond [14]. Uranium atoms are coloured green, sodium purple, nitrogen blue, silicon cyan, and carbon grey. Hydrogen atoms are omitted for clarity.

actinide–ligand–actinide interactions [18] to actinide–ligand–transition metal–ligand–actinide structures [19]. Some even more exotic compositions have been suggested, such as nanoparticles composed entirely from fullerene-like structures of uranyl peroxide currently only extant in simulations [20].

For a broader background of actinide chemistry, recommended texts include *"The f-Elements"* (1999, OUP, [1]) for a general overview, and *"The Chemistry of the Actinide and Transactinide Elements"* (2006, Springer, inc. [2]) for comprehensive and in-depth review of actinide chemistry and use.

1.2 Computational Motivation

A significant number of factors combine to make actinide chemistry difficult to perform, from both a technical and bureaucratic point-of-view: while thorium is fairly obtainable, and depleted uranium can be obtained for scientific work, getting hold of quantities of other actinides is extremely difficult. Once the actinide material is obtained, the radioactivity and toxicity of actinide compounds means that extremely strict safety precautions must be followed, involving negative-pressure glove-boxes, the use of Geiger counter sweeps when entering and leaving the laboratory, and the careful management of *all* laboratory waste.

Radioactivity also makes work more difficult in other ways – for example, particle emission within a lattice degrades crystalline products, amorphising and weakening them, as well as creating previously excluded elements that can frustrate attempts at characterisation.

Actinides in metallic form are pyrophoric, strongly reducing, and generally very reactive, and actinide compounds are frequently air and/or water-sensitive which can make preparation, transport, and analysis of samples problematic.

Clearly for the optimisation of separation chemistry, a good understanding of actinide and lanthanide behaviour in both aqueous and organic phases is required, but equally clear is that any factor that could aid in focusing the direction and aiding the analysis of experimental actinide work is even more beneficial than in other fields of chemistry. Much computational work therefore focuses on actinides, at various scales and levels of accuracy ranging from excitation simulations of the uranyl cation [21], to dynamic force-field-based systems approximating aqueous actinide solutions[11, 22].

The following chapter contains description of the computational methods and tools necessary for and used in the studies of actinide chemistry contained in this work.

1.3 EXAFS

Later in this work, experimental extended X-ray absorption fine structure (EXAFS) results are compared with results obtained from simulation. A full discussion of EXAFS techniques is beyond the scope of this document, however, briefly, it involves obtaining the X-ray absorption spectrum for a wide-range of frequencies, and looking at the fine structure of the spectrum near sudden maxima in the absorption – known as 'edges'. Analysis of the periodicity, frequency, and amplitude of the absorption structure in this region can give information about ligation, in particular the number of coordinating atoms to a central ion, their distance from that ion, the sphericity of the bonding environment, and the oxidation state of the central ion [23].

This technique has particular advantages over other analytical techniques with regards to actinides, as samples can be in any phase, and can be present in very low concentration.

1.4 Objectives

The goals of the work presented in this thesis were two-fold:

- To study the differences in covalent behaviour between the actinides using a variety of computational techniques, in order to ascertain whether trends observed in study of tetravalent actinide tetrakiscyclopentadienyl compounds could be observed in other related species, how these trends manifest in various observables, and how they relate to bonding behaviour relevant to extraction and separation chemistry. This work is discussed in chapters 3 and 4.

- To obtain an understanding of aqueous plutonium speciation with a view to applying similar techniques to wider dynamic actinide ligation simulation. This work is discussed in chapter 5.

Chapter 2

Computational Chemistry Methods

As previously discussed, computational work can be even more beneficial to discovery and analysis in this field than in other areas of chemistry. However, this is also not without difficulty. To accurately model actinide-containing chemical systems, methods to obtain an approximate wavefunction and density – the electronic structure – of that system are used. The dense electric fields in the region of the actinide atom require at least approximate treatment of electron correlation, not present in simple and computationally inexpensive electronic structure treatments, while symmetric actinide compounds can also often contain degenerate f-based orbitals or degenerate ground states which also require more advanced methods to elucidate correctly. The actinide core orbitals also have extremely high curvature and thus kinetic energy, which results in their being strongly affected by relativistic effects. These effects are commonly neglected for lighter elements, but can be extremely important for modelling actinide behaviour correctly, as these core orbitals influence all other electronic behaviour in the region of the atom.

This chapter attempts to give an overview of the various techniques required to model electronic structure used in this work, including specialist methods required for modelling heavy atoms.

2.1 Wavefunctions and Density

To produce accurate models of molecules with complex electronic behaviour, one can attempt to model either the electronic wavefunction, or the electronic density. These two functions are linked in the derivation of density functional theory, which demonstrates that a ground state wavefunction is uniquely defined by a ground state

density[24].

Ideally, a solution to the time-independent Schroedinger equation would be obtained, giving the exact nuclear and electronic wavefunctions for a given species. However, this resolves to a quantum many-body problem, which has no general solution. Instead, then, it is necessary to obtain approximate numerical solutions, applying several additional approximations to make the calculations tractable.

2.1.1 The Born Oppenheimer Approximation

This approximation, also known as the adiabatic or "clamped nuclei" approximation, assumes that motion of the nuclei and motion of the electrons are separate – that the electrons, being much lighter than the nuclei, re-optimise in response to nuclear motion essentially instantly. This lets us treat the nuclei essentially classically, either as point charges or as three-dimensional Gaussian-function shaped smears of positive charge, moving in a force field generated by the electrons. In turn, the electrons are treated as being affected by a general Coulombic nuclear potential.

2.1.2 The Hartree-Fock Approximation

The Hartree-Fock approximation expresses a Schroedinger-like equation in terms of a set of one-electron orbital functions, using as an approximation to the wavefunction the expression for the determinant of a matrix. This matrix contains the orbital functions ϕ_i on the coordinates of each electron r_i, as shown in eq. 2.1. Commonly known as the Slater determinant (usually denoted as Φ), this expression gives a wavefunction that is antisymmetric with respect to electron exchange, obeying the Pauli exclusion principle. This property arises mathematically from the property of matrix determinants to change sign when any pair of rows or columns are exchanged, which in its use as a description of the wavefunction is equivalent to exchanging two electrons.

$$\Phi = \frac{1}{\sqrt{N!}} \begin{vmatrix} \phi_1(r_1) & \phi_2(r_1) & \dots & \phi_N(r_1) \\ \phi_1(r_2) & \phi_2(r_2) & \dots & \phi_N(r_2) \\ \vdots & \vdots & \ddots & \ddots \\ \phi_1(r_N) & \phi_2(r_N) & \dots & \phi_N(r_N) \end{vmatrix} \tag{2.1}$$

$$\hat{H}_{HF}\Phi = E\Phi \tag{2.2}$$

$$\hat{H}_{HF} = \hat{T}_e + \hat{V}_{ne} + \hat{V}_{ee} + \hat{V}_{nn} \tag{2.3}$$

The Hamiltonian for Hartree-Fock theory originates from converting the rather general expression shown in eq. 2.3 containing terms for the electronic kinetic energy T_e and the various potentials for the forces generated by the nuclei and electrons V, to a set of one- and two-electron operators on the one-electron orbitals $\phi_i(\mathbf{x})$ that compose the Slater determinant: $\hat{h}$, the orbital energy component accounting for kinetic energy and the nuclear potential (commonly known as the one-electron core Hamiltonian); $\hat{J}$, Coulombic repulsion between the electron in the orbital and the other electrons; and $\hat{K}$, the exchange operator . In the Born-Oppenheimer approximation, V_{nn} remains constant for a given set of nuclear positions. The resulting expression is shown in eq. 2.7.

The core Hamiltonian is dependent only on the orbital form of the orbital it operates on and the position and charge of each of the nuclei, $\mathbf{x}_A$:

$$\hat{h}\phi_i(\mathbf{x}) = \hat{T}_e + \hat{V}_{ne} = -\frac{1}{2}\nabla^2\phi_i(\mathbf{x}) - \sum_A \frac{Z_A}{|\mathbf{x}-\mathbf{x}_A|} \tag{2.4}$$

The Coulomb and exchange operators, however, rely on the functional forms of a second orbital. For orbital functions ϕ_i and ϕ_j:

$$\hat{J}_j\phi_i(\mathbf{x}) = \phi_i(\mathbf{x})\int |\phi_j(\mathbf{x'})|^2 \frac{1}{|\mathbf{x}-\mathbf{x'}|}\mathrm{d}\mathbf{x'} \tag{2.5}$$

$$\hat{K}_j\phi_i(\mathbf{x}) = \phi_j(\mathbf{x})\int \phi_j(\mathbf{x'})^*\phi_i(\mathbf{x'}) \frac{1}{|\mathbf{x}-\mathbf{x'}|}\mathrm{d}\mathbf{x'} \tag{2.6}$$

Then, for a given Slater determinant Φ with orbitals $\{\phi_0, \phi_1, ..., \phi_{N_e}\}$ with a number of electrons N_e:

$$E = \sum_i^{N_\mathrm{e}} \int \phi_i^*(\mathbf{x})\,\hat{h}\phi_i(\mathbf{x})\,\mathrm{d}\mathbf{x} + \frac{1}{2}\sum_i^{N_\mathrm{e}}\sum_j^{N_\mathrm{e}}\left(\int \phi_i^*(\mathbf{x})\,\hat{J}_j\phi_i(\mathbf{x})\,\mathrm{d}\mathbf{x} - \int \phi_i^*(\mathbf{x})\,\hat{K}_j\phi_i\mathrm{d}\mathbf{x}\right) + V_{nn} \tag{2.7}$$

Or in the commonly used bra-ket notation:

$$E = \sum_{i}^{N_e} \langle \phi_i | \hat{h} | \phi_i \rangle + \frac{1}{2} \sum_{i}^{N_e} \sum_{j}^{N_e} \left(\langle \phi_i | \hat{J}_j | \phi_i \rangle - \langle \phi_i | \hat{K}_j | \phi_i \rangle \right) + V_{nn} \tag{2.8}$$

These expressions can also be re-written as operations of vectors and matrices, and the Roothan-Hall reformulation then allows the orbitals to be expressed in terms of a set of linearly combined basis functions, the coefficients of which can then be adjusted to minimise the Hartree-Fock energy iteratively as a general optimisation problem. Because the evalulation of the energy expressions at each iterative step involves using the orbitals generated in the last step, this is commonly known as a *self-consistent field* or SCF approach, and the value of the electronic energy it gives may be referred to as the SCF energy.

The Hartree-Fock approximation has many useful properties, however, its results suffer from its complete neglect of electron correlation, due to only considering electron-electron repulsions as an interaction of each electron with a mean field. Consequently, density-functional theory has largely superceded it as the method of choice for single-determinant calculations. It has many uses as part of more complex methods, however: sets of one-electron orbitals created by an initial Hartree-Fock calculation may be used in perturbational treatments such as Møller-Plesset theory, as well as more expensive methods that use many one-electron configurations to include electron correlation, and the exchange operator in the Hartree-Fock equation may also be used in density-functional theory.

One of the useful properties of Hartree-Fock calculations, that is not present in density-functional theory, is that due to the exact nature of the terms used and the lack of any approximate terms, the system energy resulting serves as an upper-bound to the true energy. This property is known as the variational principle, and applies to any such generated wavefunction that is free of approximate terms, i.e. that only omits energy contributions, rather than substituting them for simplified expressions.

2.1.3 Relativistic Approximations

The Schroedinger equation is a nonrelativistic equation, as is the Hartree-Fock approximation to it. For a full treatment of special relativity in a chemical environment, it is necessary to instead turn to the time-independent Dirac equation (2.9).

$$\left(c\vec{\boldsymbol{\alpha}}\cdot\hat{\mathbf{p}}+\boldsymbol{\beta}mc^2\right)\boldsymbol{\Psi}=E\boldsymbol{\Psi} \tag{2.9}$$

c is the speed of light, m is the mass of the electron, $\vec{\boldsymbol{\alpha}}$ is a vector of matrices constructed from the Pauli spin matrices $\boldsymbol{\sigma}_{x,y,z}$, as shown in (2.10), $\boldsymbol{\beta}$ is the 4×4 unit matrix $\mathbf{I}_4$, and $\hat{\mathbf{p}}$ is the momentum operator.

$$\vec{\boldsymbol{\alpha}}_{x,y,z}=\begin{pmatrix}\mathbf{0}_2 & \boldsymbol{\sigma}_{x,y,z}\\ \boldsymbol{\sigma}_{x,y,z} & \mathbf{0}_2\end{pmatrix} \tag{2.10}$$

$$\boldsymbol{\sigma}_x=\begin{pmatrix}0&1\\1&0\end{pmatrix},\boldsymbol{\sigma}_y=\begin{pmatrix}0&-i\\i&0\end{pmatrix},\boldsymbol{\sigma}_z=\begin{pmatrix}1&0\\0&-1\end{pmatrix}$$

A full discussion of the relevance of each part of the Dirac equation is beyond the scope of this document, however, three important aspects should be noted.

- It includes a full theoretically sound basis for electron spin, with the use of the Pauli spin matrices in the construction of $\vec{\boldsymbol{\alpha}}$ and $\boldsymbol{\beta}$. This allows the inclusion of non-collinear spins, as the Pauli matrices provide a complete spatial basis for spin. This fuller description of electron spin also allows for the description of spin-orbit coupling.

- The wavefunction described by the Dirac equation is a four-component spinor rather than a scalar function.

- The Dirac equation includes solutions involving negative energy eigenstates via coupling with positronic eigenstates. The presence of these includes the effect of quantum electrodynamic effects at high energies, and means that the energy spectrum is symmetric about the 0 energy point, with continua of energy levels at m_ec^2 and $-m_ec^2$. This means that methods that minimise the energy can obtain an infinitely negative energy value (known as *variational*

collapse).

In the non-relativistic Schroedinger equation, the energy of a free electron is 0, while in the Dirac equation, it is mc^2 as previously noted. To re-align the two, the matrix $\boldsymbol{\beta}$ may be replaced by $\boldsymbol{\beta}'$, shown in (2.1.3).[25]

$$\boldsymbol{\beta}' = \begin{pmatrix} \mathbf{0}_2 & \mathbf{0}_2 \\ \mathbf{0}_2 & 2\mathbf{I}_2 \end{pmatrix}$$

The four components in the wavefunction produced by the Dirac equation make calculations much more complex to perform. In addition, spin-orbit coupling effects make analysis more complex due to the double point groups they introduce to the orbital symmetry, and are often small enough to be negligible. To alleviate these difficulties while retaining the accuracy of the majority of spin-orbit coupling effects, there are a number of approximate Hamiltonians based on the Dirac equation, of which two are most commonly used: the Zeroth-Order Relativistic Approximation (ZORA), and the Douglas-Kroll-Hess (DKH) Hamiltonians. Both of these options allow either the inclusion or neglect of spin-orbit coupling.

The ZORA and DKH Hamiltonians both approximate the Dirac equation in a way that reduces the four-component form to a two-component form, the two components being the alpha and beta spin orbitals in the scalar form. (In the spin-orbit coupled model, where spins are not necessarily collinear, alpha and beta labels are no longer applicable.) This greatly reduces the complexity of the calculation and the basis sets required[26].

Since programs commonly implement only one of ZORA or DKH, the choice of which to use is usually not available within a code.

2.1.4 Relativistic Effective Core Potentials

An alternative to these relativistic approximations is to assume that all relativistic effects are confined to the core electrons rather than the valence regions of the atoms, and then replace a number of the core electrons with a potential field, for example, in the 'small-core' actinide RECPs by the Stuttgard-Dresden group[27], 60 core electrons (up to the 5d orbitals) are removed. This also allows the omission of these electrons from the self-consistent field construction, and lowers the nodality required of

the remaining basis set functions.

If the orbitals the core potential replaces are relatively unperturbed by the valence orbitals still modelled, the removal of the core electrons from consideration can both greatly speed up simulation and remove the need for explicit consideration of relativistic effects in the Hamiltonian, at the cost of reduced accuracy, and the impossibility of modelling effects that rely on explicit electronic behaviour at the nucleus.

2.1.5 Density-Functional Theory

Density-functional theory (DFT) arises from a result of Hohenberg and Kohn, that the ground state wavefunction is uniquely defined by the ground state density[24]. While, in theory, this allows the definition of an expression for the energy in terms of that density alone (eq. 2.11), in practice it has proven so far impossible to obtain accurate expressions for the electronic kinetic energy, exchange energy, and electron correlation energy, from the density alone.

$$\rho = \sum |\phi_i|^2 = \Psi^* \cdot \Psi$$

$$E\left[\rho\right] = T\left[\rho\right] + V_{ne}\left[\rho\right] + J\left[\rho\right] + E_{XC}\left[\rho\right] \tag{2.11}$$

The Kohn-Sham form instead expresses the density in terms of a Slater determinant for a system of non-interacting electrons [28]. The method used to obtain this result separates the terms of the Hamiltonian into two groups. The first comprises the zero- and one-electron terms for the non-interacting electrons: the nucleus-nucleus potential V_{nn} and the same core Hamiltonian $\hat{h}$ as in Hartree-Fock theory (eq. 2.4). The kinetic energy produced by the core Hamiltonian here is approximate despite using the exact operator, however, as an artifact of the construction of the non-interacting electron system: as the orbitals produced tend towards the eigenvectors of the exact density matrix, so the kinetic energy will tend towards the exact kinetic energy [25].

The second group covers all interactions between electrons, through two terms: the same classical (Coulombic) electron-electron repulsion $\hat{J}$ as in Hartree-Fock theory (eq. 2.5); and a potential-like term that in principle covers exchange, any interac-

tion correction to the kinetic energy, and non-classical correlation, E_{XC}, also called the exchange-correlation functional.

By definition, then, the E_{XC} term includes all energy terms that deviate from the non-interacting system, making density functional theory exact. However, the exact form is not known, and even if it were, it is expected to be extremely computational intensive. For these reasons, various approximations to E_{XC} are available, and due to the (albeit approximate) inclusion of electronic correlation, these approximate functionals are capable of yielding better results than Hartree-Fock theory. Additionally, many functionals do not contain any operators as computationally intensive as the exchange operator in the Hartree-Fock method, which involves many multi-centre two-electron integrals.

Because the functional now depends on the orbitals used to construct the density (commonly referred to as the Kohn-Sham orbitals), essentially the same techniques can be applied to solve this equation as for the Hartree-Fock method, and in fact a Hartree-Fock solver may be implemented as a Kohn-Sham density functional theory solver with the exchange-correlation functional only including the exchange operator from eq. 2.6.

Functionals

There are a wide range of functionals, and the considerations for use tend to differ between the exact requirements of the calculations being performed – for molecular ground state geometry optimisations, the simplest functionals can give reasonable coordinates, but in excitation energy calculations, for example, results can vary wildly between functionals.

A common system for labelling the main categories of functionals includes the categories listed below, in approximate order of complexity. Exchange and correlation terms for functionals are usually specified separately, and are commonly given short labels that include the authors of the specification along with the year if necessary. These are often ranked in order of accuracy and (frequently correlated) computational expense, into what has been termed a “Jacob’s Ladder of density functional approximations” with the least accurate at the bottom and the ideal exact functional at the top [29].

- *Localised Density Approximations* (LDAs) – This type of functional was the first to be developed for the purpose, and uses only the localised density value to calculate the energy density at a point.

- *Generalised Gradient Approximations* (GGAs) – The generalised gradient approximations advance the theory by including a correction to an LDA dependent on the gradient of the density.

- *Meta-GGAs* – The functional form can be further complicated by including a term dependent on the kinetic energy density term, and functionals of this type are known as meta-GGAs.

- *Hybrid Functionals* – Any of the above classes of functionals can be modified to include the exact exchange operator from Hartree-Fock theory, however, because the orbitals obtained from density-functional theory are not the same as those from Hartree-Fock theory, the exchange term obtained this way remains approximate in a similar fashion to the kinetic energy term. For this reason, hybrid functionals use a linear combination of the Hartree-Fock exchange and another term for the exchange. Very generally, this technique tends to result in better energies for delocalised systems, but the Hartree-Fock exchange term is computationally expensive and so may not be practical for large systems.

While there is no systemic way to improve a functional's accuracy, above these, more sophisticated (and expensive) methods can be applied to either tailor the functional to a specific set of conditions, or to introduce the random-phase approximation, analogous to the application of Møller-Plesset theory to Hartree-Fock calculations.

2.1.6 Basis Sets

When selecting a set of basis functions for a calculation, there are several issues to consider. For molecular calculations, typically basis functions centred on each atom of the system are used. For periodic systems, with infinitely repeating motifs and typically less empty space, plane wave basis sets are more common.

2.1.6.1 Atom-Centred Basis Functions

There are two common forms of atom-centred basis function in widespread use – the Slater-type, and Gaussian-type orbital functions (STOs and GTOs). These can be separated into an angular and a radial component, and when expressed in polar form, only the radial component differs between the two functional forms, shown in eq. 2.13 and 2.14 respectively. In this format, r is the scalar radius, θ and ϕ are the two angular coordinates, R is the radial component, Y is the angular component, A is a normalisation coefficient, ζ is the exponent that determines the steepness of the function, n is the orbital principle quantum number, and l is the orbital angular momentum.

The Slater-type orbital function is based on a functional fit to the hydrogenic solution to the Schroedinger equation. The main advantage of this type of orbital is that it models the density quite accurately, especially around the nucleus where it has the predicted cusp behaviour, so relatively few functions are needed to obtain a good fit. Unfortunately this comes at the cost of computational expense – integrating overlaps between STOs centred on different atoms is a significantly more difficult problem than for GTOs. Additionally, STOs decay too slowly, which can produce problems if interactions depend on accurate modelling of diffuse regions of density.

$$\varphi(r,\theta,\phi) = R(r)\,Y(\theta,\phi) \tag{2.12}$$

$$R_{STO}(r) = Ar^{n-1}e^{-\zeta r} \tag{2.13}$$

$$R_{GTO}(r) = Ar^{2n-2-l}e^{-\zeta r^2} \tag{2.14}$$

GTOs, conversely, decay too quickly, due to the dependence on e^{-r^2} rather than e^{-r}, as shown in eq. 2.14. The curvature of these functions, particularly near the nuclear centre, does not model the orbital behaviour very accurately, but because they are much less computationally expensive to perform multicentre integrals for, a collection of Gaussian functions can be used to approximate a Slater-type basis function. The computational gains made this way, despite using more basis functions than an equivalent quality STO basis set, have resulted in codes using GTOs and published GTO basis sets being much more common.

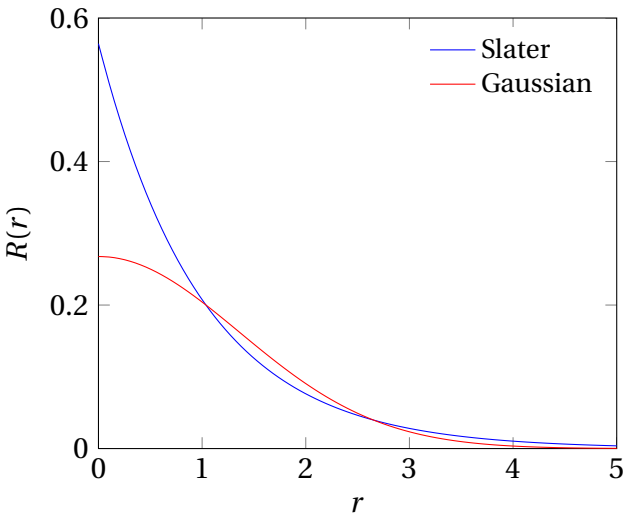

Figure 2.1: A Slater-type basis function (blue), and the fitted Gaussian-type basis function that approximates it (red).

Figure 2.1 shows the difference in functional form between STOs and GTOs. Note the cusp at the nucleus, which the STO and the accurate solution for the hydrogen atom present, but which is not present in the GTO. The actual cusp is an artifact of the use of point charge nuclei, however actual nuclear radii are several orders of magnitude smaller than electronic orbitals, so the difference in effect is small.

Because of the relatively poor fit of single Gaussian-type functions to actual orbitals, it is common to group together several such functions into a single function that more accurately describes atomic density, giving them fixed coefficients and then scaling the group as opposed to each separately. This is termed 'contraction', and basis sets have two common methods of employing it. A basis set employing segmented contraction contains a group of contracted functions modelling the core region, and then lesser degrees of contraction for valence regions. A basis set employing general contraction contains a set of functions that is contracted several times with different coefficients.

For Slater- and Gaussian-type basis sets, the general quality is denoted by the number of separately variable functions at the valence level; due to the ζ values in the basis functions, this is called the zeta level of the set. Additionally, functions one angular momentum quantum higher than the highest each atom has in its atomic orbitals are usually added to allow directional polarisation in the valence region. For anions or other systems with unusually extended density components, more diffuse

functions can be added to model these regions. Basis sets that include such functions are usually termed 'augmented'.

2.1.6.2 Plane Wave Basis Functions

As mentioned above, plane wave basis functions are frequently used in periodic systems; the matching periodic nature of the basis function and the environment allows a number of optimisations in the SCF algorithm, involving performing a Fourier transform on the matrices and calculating integrals and properties in momentum space.

Plane waves take the form shown in equation 2.15, described by a wave vector $\vec{G}$, that can be related to the kinetic energy of the wave, and $\vec{k}$, a vector related to a given lattice symmetry operator. Plane wave basis sets are typically described by a cut-off energy, which sets the maximum magnitude of $\vec{G}$. Increasing this energy allows higher energy waves, decreasing the wavelength and thus increasing the resolution of the modelled density.

$$\varphi(\vec{r}) = e^{i(\vec{G}+\vec{k})\cdot\vec{r}} \tag{2.15}$$

Electronic density tends to be orders of magnitude higher in the core regions of the atom, and orbitals near the nucleus exhibit high energy nodal behaviour, which would require the use of plane waves much higher in energy than those used to describe the valence region. To avoid this, calculations using plane waves typically also use pseudopotentials to model the core regions of each atom and eliminate the nodes present in the true wavefunction. The plane waves then only need to model the valence region and any deformation of the core.

In this work, only 'ultra-soft' pseudopotentials have been used, which model not only the core region, but a part of the valence region, allowing the use of a lower maximum energy for the basis set than for a 'harder' pseudopotential which would only model the core region. Their construction also removes the requirement that the wavefunction produced from the calculation performed with pseudopotentials and the 'true' wavefunction integrate to the same number of electrons (density norm conservation), a property which is important for simulation of some effects, especially those involving scattering or the density around the nucleus.

2.1.7 Molecular Dynamics

As well as obtaining the energy of a system with DFT, for most functionals it is also possible to calculate analytically the derivatives of the energy with respect to the nuclear coordinates. This allows us to calculate the forces exerted on the nuclei by the overall potential, and thus to model motion of the atoms. Complex dynamic processes may be modelled in this way, e.g. phase transitions[30], and information may be obtained about macroscopic parameters of compounds that would be otherwise extremely difficult to model or experimentally determine.

In QM MD methods one can distinguish between methods that re-optimise the electronic wavefunction or density each step, retaining the Born-Oppenheimer approximation mentioned above, or those which also model dynamics of the electronic degrees of freedom, approximating the ground state continuously as the nuclei move. In this work, the former technique has been used, as the latter requires the electronic and nuclear degrees of freedom to be well separated. This can lead to problems when simulating water due to the low mass of the hydrogen atoms – their fast vibrations can couple to the electronic motion.

In the molecular dynamics methods that employ the Born Oppenheimer approximation, it is still necessary to be careful when simulating light atoms, as using too long a time-step between wavefunction re-evaluations can lead to skipping over the period of hydrogenic vibrations. The absorption spectrum of liquid water has infrared peaks at a wavelength of approximately 750 nanometres [31], which converts to a vibrational period of 2.5 femtoseconds. Any simulation which hopes to model water accurately must take care to put sufficient samples within this period to ensure proper hydrogenic behaviour.

Fortunately, it is not necessary to repeat the orbital optimisation at each step, as wavefunction extrapolation techniques can not only use the previous timestep's wavefunction as an initial guess, but also to alter it in a way that may represent a more accurate guess. This can greatly reduce calculation and time requirements.

2.1.7.1 Thermostats

If treated as a closed system, a molecular dynamics simulation will conserve the total energy, the volume, and the number of particles, in what is known as the micro-

canonical ensemble. To model a system that maintains a constant temperature, as in a system which represents a solution, the canonical ensemble is used, which conserves the number of particles, the volume, and the temperature. In the minuscule cell, this is performed by applying a thermostat algorithm to maintain the simulation temperature, calculated as a sum over the atomic kinetic energies, around a fixed value. In the simulations performed in this work, a Nose-Hoover thermostat chain has been used, which periodically applies restoring forces to the system towards a kinetic energy associated with the temperature desired [32]. The actual measured temperature of the system then oscillates around that value.

2.1.7.2 Radial Distribution Functions

In a molecular dynamics simulation, a large number of atomic coordinates corresponding to different time steps may be obtained. Radial distribution functions, commonly labelled $g(\vec{r})$, represent a relatively simple way to extract geometric data from these, and may be related to a number of properties of the system in the simulation.

To calculate these from a set of atomic coordinates, two classes of atoms must be selected: the references, and the targets. Histogram bins of distances from the reference to the target atoms are then filled for all configurations, and the finished bins are normalised. This gives a plot indicating the distance correlation between the two classes, as well as how variable the distance is in time due to, for example, vibrational modes, or ligand exchange. The integration of this plot can be used further to give the number of atoms in a 'shell'.

2.1.8 Geometry Optimisation

To obtain a geometry of a molecule or other system of atoms, it is necessary to minimise its energy with respect to the nuclear geometric degrees of freedom. While this can be done by altering Cartesian coordinates directly, in aperiodic systems, it is usually more efficient to instead construct a set of redundant 'internal' coordinates which represent a scaffolding of interatomic distances and angular separations.

There are then a number of options as to algorithm. Since at an optimal geometry, the forces on the atoms are reduced to zero, damped molecular dynamics can be used. This allows the system geometry to relax in the direction of the forces on

the nuclei produced by the electrons, until it reaches a stable point. This can work well for periodic systems and systems containing no light atoms, but may not for molecules with, for example, hindered rotors, or extended chains, due to the low curvature of the potential surfaces for the movements of these sections.

The more common option for molecular systems is to use one of a number of quasi-Newtonian algorithms, in which the gradient of the energy with respect to the possible alterations of the geometry is calculated, and then an approximation of the derivative of the gradients is made, and an alteration to the geometry made based on those. The most commonly used algorithm of this type is the Broyden–Fletcher–Goldfarb–Shanno algorithm, which iteratively improves an approximation to the matrix of the second derivatives of the energy (the *Hessian*) at each step. Construction of a more exact Hessian, while possible, is far more computationally expensive than this type of method, and is generally only used for geometric optimisation when cheaper methods fail to produce good results.

One of the possible such failure cases for this type of optimisation is the convergence to an nth-order saddle-point, rather than a stable potential well. While all the energy gradients fall to zero at a minimum, this is also true for saddle-points, and the common convergence criteria, the absolute change in energy and the norm of the energy gradient, will not distinguish these. The method used to distinguish these to is to calculate the Hessian for the quadratic approximation to the possible vibrations of the molecule (see section 2.1.9). At a true energy minimum, the Hessian eigenvalues are all positive or zero, meaning that any further alteration of the geometry would raise the energy. At a saddle-point, one or more eigenvalues will be negative, indicating that the alteration corresponding to that vibrational mode lowers the energy of the molecule. Because the vibrational frequency is dependent on the square root of the force constant eigenvalue from the Hessian, a negative force constant produces an imaginary frequency value.

2.1.9 Vibrational Frequency Calculation

Close to a stable potential well with respect to all geometric coordinates, *i.e.* an optimal geometry, it may be assumed that the energy behaves approximately harmonically. This can be used to calculate vibrational frequencies for a molecule, by trans-

forming the coordinates into a set of mass-weighted coordinates and constructing an eigenvalue problem for the second derivative of the energy. From the square root of the eigenvalues, the frequencies are obtained, and the eigenvectors indicate the modes of vibration for the system.

As stated above, at a stable optimal system geometry, all the vibrational frequencies thus calculated should be zero or positive. The zero values are obtained from the transformational and rotational modes, and may not be exactly equal to zero due to numerical error.

2.1.10 Solvation Models

For quantum mechanical calculations, there are a number of possible solvent models that are applicable to static systems. However, each suffers from certain limitations.

COSMO (the COnductor-like Screening MOdel) is one of the more commonly used members of a set of methods which represent the solvent as a continuum which presents a surface to the solute[33]. In practice, this takes the form of a set of point or disc charges distributed across a surface around the solute, which balance the charge density of the system, and may be scaled by a factor representing the dielectric constant of the solvent. The surface is typically constructed using a grid mapped across a set of overlapping atom-centred spheres with some algorithm to remove sharp intersections. The main weakness of this type of method is that it precludes the possibility of the movement of electron density onto the solvent, as may occur with strongly interacting solvents like water, and so it will tend to underestimate solvation energies in this type of system [34]. Charged species are modelled especially poorly, for the same reason – these species are much more likely to cause significant density movement to or from the solvent, rather than mere polarisation.

Other models based on non-quantum mechanical approaches to the solvent, such as the hybrid Quantum Mechanics/Molecular Mechanics (QMMM) model that uses a forcefield approach to modelling solvent molecules and presents their effect on the QM system as an overall charge field, suffer similar issues, while approaches that do model the full solvent explicitly in a static system suffer from having to make arbitrary choices about the number of solvent molecules or their configurations, and

may also be significantly more computationally expensive.

COSMO has been used in this study only to obtain approximate relative energies of static structures. Due to the varying charge in the systems studied, it is expected that unpredictable errors in energies will be present when comparing structures with differing charges, however, between structures with the same overall charge the error should decrease slightly in magnitude for larger structures, as the charge is more dissipated.

2.1.11 Computational Analysis Techniques

There are available a wide array of techniques to analyse either the orbitals or the density of a simulated molecule. To gain chemical insight, commonly some partitioning of density is employed to allow the comparison of values between systems, or to transform the orbitals to make them more closely resemble two or three-atom bonding or antibonding orbitals.

2.1.11.1 Mulliken analysis

Mulliken analysis is the most common member of a set of techniques based on extracting information from the density and overlap matrices produced by a single-determinant calculation using atom-centred basis functions[35]. In this work, results have been presented from the Mulliken formulation for charges and net spins.

The charges are obtained by multiplying the density matrix and the overlap matrix elements for each pair of basis functions, and assigning half the resultant density to each of the atoms at the centre of those basis functions. Net atomic spin values may then be found by obtaining the difference of the charges for alpha and beta spin orbitals.

The usefulness of values obtained this way is often criticised, as they are highly basis-set dependent. Extended orbitals centred on one atom but with density that extends into the region of another may not be treated correctly, and for this reason calculations of this type with smaller basis sets may give more accurate portrayals of the density localisation.

Regardless of the commonly discussed problems, many programs that perform SCF calculations perform Mulliken analysis by default because it requires very little additional computational effort.

2.1.11.2 Atoms In Molecules

Atoms in Molecules (also known as *The Quantum Theory of Atoms in Molecules*, AIM or QTAIM) is a technique devised by Richard Bader[36] for dividing the electronic density of a molecule into regions representing distinct atoms within the molecules, using topological analysis. The space around the molecule is divided into atomic basins, each containing one nuclear attractor critical point (NACP) – maxima of the density usually coincident with the nuclear coordinates. The basin boundaries are defined by surfaces comprised of points at which there is no electronic density gradient component perpendicular to the surface; these are known as zero-flux surfaces. (See figure 2.2). These basins have many useful properties as components of the system, among which is that the density can be integrated over atomic basins to obtain a measure of the quantity of electronic charge most attracted by a particular atomic nucleus.

In addition to atomic basins, the topological analysis involved yields a number of other useful features: 'bond paths', lines of maximum density between two nuclear attractor critical points, and three types of critical point in addition to the NACPs - bond, ring, and cage critical points, with topological properties as shown in table 2.1.

Because the properties at a bonding critical point are representative of the properties of the density along a bond path, and the properties of the density along a bond path are closely related to the properties of the loosely-defined 'chemical bond', we can use them to make inferences as to certain properties of the bonding between atoms.

Analysing degrees and properties of bonding at the bond critical point, values commonly quoted are those of the Laplacian of the density, or $\nabla^2\rho$, and the Cremer energy density H.

The Laplacian of the density at a given point shows the degree of local accumulation or depletion of density. Negative values of the Laplacian, indicating accumulation, may be correlated with the covalency of the bond. Topological analysis of the Laplacian itself rather than the density may be performed, which gives critical points commonly associated with Lewis-model electron pairs.

The Cremer energy density is a little more complex, being a sum of G, the local

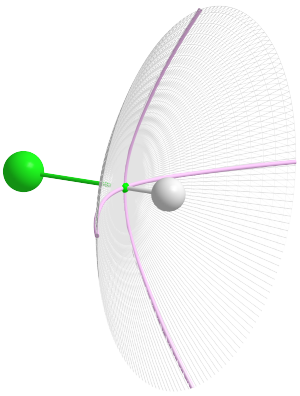

Figure 2.2: The atomic basin boundary in HCl, showing the larger basin of the chlorine (green) due to its much larger density contribution.

Type	Density Hessian Trace	Represents
Nuc. Attract.	3	An atomic centre
Bond	1	Minimum ρ on a bond path
Ring	-1	Minimum ρ within a ring of bonds
Cage	-3	Minimum ρ at the centre of a cage of bonds

Table 2.1: Types of Critical Point

kinetic energy density (+ve), and V, the local potential energy density (-ve), it represents to what extent the confining, attractive forces on the electrons are balanced by the dispersive, repulsive forces. An overall negative value represents a point where the attractive forces exceed the repulsive ones, and thus where electronic density is attracted to overall. Negative values of H at the bond critical point are therefore also associated with covalent character.

The AIMAll code[37] has been used throughout this work to perform analyses based on the QTAIM on molecular systems.

Density Catastrophes

In an ideal triatomic ring, three bond critical points and one ring critical point would be found. However, due to asymmetry either in the geometry or the atomic types, a ring critical point and a bond critical point can combine and annihilate. This leads to no bond path being found between two atoms where one would be expected, and often also with one of the bond paths in the ring being significantly curved into the ring [38].

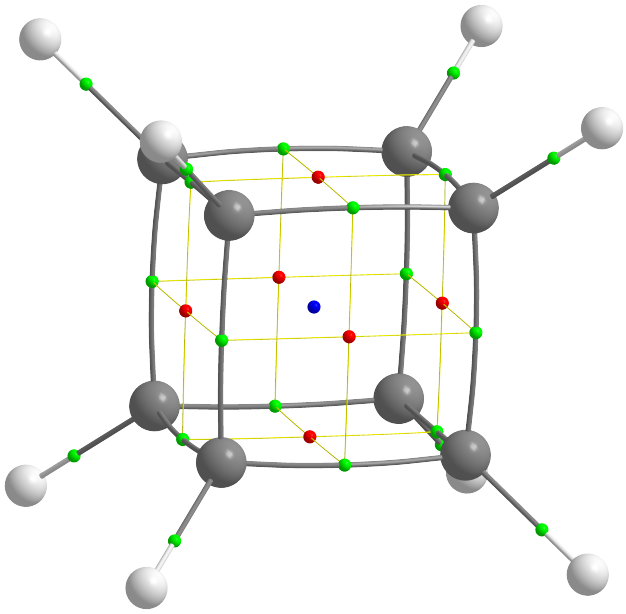

Figure 2.3: Density critical points, bond paths, and minimum gradient paths between bond critical points and ring-critical points in cubane.

This is an especially common situation around high-valence centres, or in regions of very low density with long bonds [39].

2.1.11.3 Natural Population Analysis

There are a number of analyses based on diagonalising the density matrix from an SCF calculation, either in whole, to obtain charge information, or in sub-blocks, to obtain bonding information. Natural Population Analysis (NPA) gives charge and orbital type occupancy by producing basis orbitals that are not only orthogonal, but that are orthogonal between nuclear centres – localised to one atom. By summing the occupations of these for each atom, atomic charges may be obtained [40]. Unfortunately, the orthogonalisation process can be sensitive to the choice of which orbitals should be designated "core", "valence", and "Rydberg", as orbitals labelled "Rydberg" are partitioned separately and allowed to vary significantly to obtain higher core and valence orbital occupations. This can lead to problems in compounds with non-trivial orbital shell usage, such as transition metal and actinide compounds[41].

2.2 Codes

2.2.1 ADF

The Amsterdam Density Functional (ADF) package provides programs for performing molecular QM calculations and various post-processed analysis[42, 43]. It is unusually capable in transition and *f* metal chemistry, having included complete basis sets for atoms up to the transactinic elements, with optional pre-set frozen cores, as well as relativistic treatments at both the scalar and spin-orbit-coupled levels. It uses Slater-type basis functions only, with density fitting functions to accelerate calculations.

Unfortunately, many analysis codes that use orbital or density information from other packages are not capable of handling input using Slater-type functions, so for these, ADF output is not suitable.

2.2.2 Gaussian

The Gaussian package provides the capability to perform many different types of molecular or solid-state structure calculation, from parameter-based molecular mechanics methods to configuration interaction and coupled-cluster methods [44]. For QM calculations, it uses Gaussian-type functions and, due to its popularity and longevity (the first version of the Gaussian code was released in 1970), many analysis codes are specifically able to handle Gaussian output.

2.2.3 Turbomole

The Turbomole suite provides a similar range of functionality to Gaussian, and, although not quite as comprehensive in its list of available techniques, is more performance-focused. Like Gaussian, it uses Gaussian-type functions, but is notable for early implementation of a technique known as "resolution of identity DFT" to reduce the number of calculated integrals needed with negligable impact to accuracy[45, 46].

2.2.4 CASTEP

The CASTEP code is designed to perform DFT calculations on periodic systems, using plane wave basis sets and pseudopotentials[47]. It includes facilities for both optimisation and molecular dynamics, as well as a wide range of property calcula-

tions specialised for periodic systems.

2.2.5 AIMAll

AIMAll is a package specifically for performing QTAIM calculations and computing other properties based on QTAIM information [37]. It takes a file containing Gaussian-type-function-based SCF wave function information as input.

2.2.6 Others

A number of other codes have been used to prepare results and figures, including Avogadro and POVRay for pictures of molecules and isosurfaces [48, 49], VMD for RDF calculations from CASTEP output and the generation of randomised cells of water molecules [50], and Python and bash scripting for a wide range of post-processing calculations and data extraction [51, 52].

Chapter 3

Covalency in Actinide Complexes I: Tris-cyclopentadienyls

This chapter focuses on work performed to investigate the covalency of trivalent actinide triscyclopentadienyl complexes, comparing them to previous similar work performed within our research group on the tetravalent actinide tetrakiscyclopentadienyl analogues, and studying the effectiveness and clarity of various computational analysis techniques for this purpose; in particular, comparing commonly used and implemented techniques to the relatively underused QTAIM techniques.

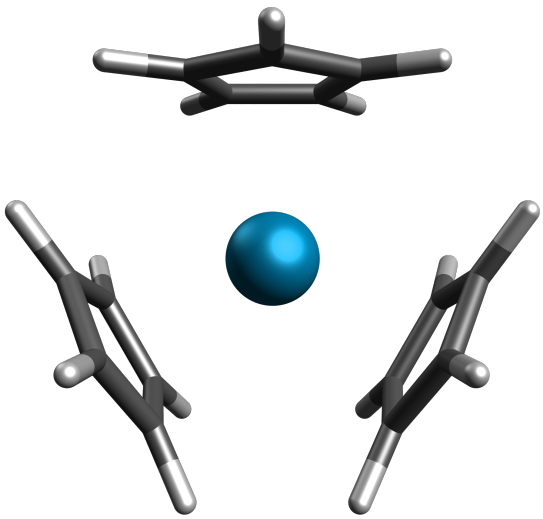

Figure 3.1: $ThCp_3$ complex, with C_{3v} symmetry.

3.1 Introduction

Cyclopentadienyl (Cp) compounds have a long history of use in investigating bonding in metal complexes, primarily because of their steric bulk, and tendency to be unreactive and noninterfering. Computational studies have focused on actinide Cp compounds in particular since the initial synthesis of such compounds in 1955 [53]. That work focused primarily on the synthesis of a tetravalent uranium chloride tris-Cp compound $(\eta^5-C_5H_5)_3UCl$, which was determined to contain bonds with covalent character by its failure to react with ferrous chloride to produce ferrocene.

Studies have since attempted to analyse the molecular orbital composition of such compounds to attempt to determine the trends and factors affecting their covalency [54], which may be transferable to other actinide complexes. The ability to predictably create compounds which have a significant difference in bonding character between different actinides and between actinides and lanthanides may be used in such processes to separate lanthanide and actinides [55], an important component of long-term waste management. Am (III) and Cm (III) in particular have very similar reactivity and ionic radii to a number of lanthanide (III) ions, but very different radioactive decay rates and daughter products, which necessitates different storage, handling, and designed storage lifetimes for the different active lifetimes of the materials. Several studies have focused on attempting to use soft ligand donors such as sulphur, to utilise the slightly higher perceived tendency for covalent character in bonding with actinides over lanthanides[56, 57, 58, 8]. Unfortunately from a reprocessing perspective, this is at odds with a common design goal of only using carbon, hydrogen, oxygen, and nitrogen, to minimise additional waste generation through easy and clean combustion. Work continues to probe new ligands and their bonding differential capability, with much current interest being focused on chelating ring-based systems with nitrogen donors, such as BTP[59] and BTBP[60, 61], in particular to attempt to determine the cause for the high selectivity of BTP for americium and curium.

It was therefore of some interest when a study into $M[N(EPR_2)_2]_3$ (M=La, Ce, Th-Cm, E=group 16 element, R=Ph, ^{i}Pr) showed that the greatest orbital mixing in this series of compounds occurred not with the uranium, as might be expected by the conventional view of actinide bonding via spatial overlap of the extended *f* or-

Figure 3.2: Qualitative valence orbital interaction diagram for an $AnCp_3$ in C_{3v}. (Adapted from [62].)

bitals, but with the americium[8]. However, it was concluded that this mixing was not due to orbital-overlap-based covalency but rather a coincidental energy matching between orbitals of ligand and metal, and that the radial contraction observed across the actinides would preclude significant overlap with americium.

Similar conclusions were reached in a study by Strittmatter and Bursten in an earlier investigation performing DFT calculations upon the actinide tris-Cp systems UCp_3−$CfCp_3$[62]. Unexpectedly large metal contributions were found in the a_2 valence orbitals expected to be almost entirely localised upon the Cp ring, and were similarly attributed to near-degeneracy between the 5*f* and ligand levels.

The valence orbitals of $AnCp_3$ are shown schematically in figure 3.2. C_{3v} symmetry splits the six $\pi_{2,3}$ orbitals into e, e, a_1, a_2, and due to being antibonding between ligands, the a_2 orbital is highest in energy. The a_1 orbital is lowest in energy in the Cp_3 system, but due to weaker interaction of this orbital with the actinide, it is less stabilised in the final $AnCp_3$ species than the *e* orbitals, which interact strongly with the actinide *d* orbitals. The a_2 ligand and *f* actinide orbital may mix if spatial overlap and energetic proximity allow, to the extent that the study in [62] found in one system over 55% actinide character in what was in other $AnCp_3$ systems a ma-

jority ligand-based orbital.

A study by Prodan and co-workers found a similar trend in solid-state actinide dioxides, AnO_2, An $\in$ {Th-Es}, where the $5f$ actinide and $2p$ oxygen orbitals become close in energy in analogous fashion to the above systems, however, combined with a trend in spin densities, they conclude that this effect *is* an increase in covalency[63].

Work by Tassel and Kaltsoyannis attempted to further elucidate the trends in these systems by studying $AnCp_4$ systems for thorium to curium, with Mulliken analysis, NPA, and with topologically obtained bond critical point (BCP) data, and found that while NPA was somewhat unclear, orbital decomposition and topological data strongly disagreed, with orbital decomposition showing the same rise in metal component in ligand orbitals around near degeneracy, while BCP data showed a marked decrease in covalency-correlated factors from uranium to curium.

This work attempts to take the comparison of all the previous indicators and topological analysis further, extending this to additional quantitative QTAIM data, and making comparison of spin density data with those obtained for the solid state actinide dioxides to assess their similarity. Also included is a comparison of different NPA partitioning schemes to investigate the reliability and behaviour of this analysis with differing partitioning schemes, and a brief inspection of the effect of exact exchange added to the PBE functional upon the data obtained.

3.2 QTAIM and Covalency

With the ever-increasing use of computational chemistry and DFT methods in particular to analyse bonding structure, ever more variety in types of bonding is being studied, from chromium-chromium quintuple bonds[64], to helium-helium magnetic bonds[65]. Along with this comes the desire to characterise these bonding interactions quantitatively, and many methods that attempt to do so have been formulated: bond order analyses, ELF, ELI-D, and more. However, as these methods grow more conceptually complex, their usefulness is diminished, as it becomes more difficult to explain what a value actually represents, and becomes less clear in what cases a method might give unexpected or unusual results. Many of these techniques attempt to assess the degree of covalency or locate covalent bonds, but unfortunately chemical bonding and covalency in particular are not rigorously defined

concepts. The original formation of the concept has been overloaded by decades of chemistry discussion, and strong disagreements may occur over the nature of bonding in difficult systems[66].

Interest in QTAIM for performing bonding analysis has been slowly growing, and it has many commendable properties: the critical features hinge only on relatively simple concepts, it gives results that can at least heuristically be connected with bonding characteristics, and it can be connected to the simple VSEPR theory through the valence shell charge concentration method (VSCC). Many studies focus purely on the critical points, and while bond critical points do not necessarily indicate what many chemists would think of as a bond, they are sufficient to indicate a bonding interaction – an attractive force between two atoms. Evaluating additional properties at the critical points may give further indications of chemical behaviour, but still, this is a very limited view of the environment, and may omit pertinent qualities.

Performing the full QTAIM integration over the atomic basins – a time-consuming process for large molecules, especially with heavy elements – yields quantities less trivially explicable: most temptingly, the delocalisation index calculated over QTAIM atomic basins, which describes how much of the electronic exhange-correlation pair density in the basin of atom A is shared or exchanged with atom B, and which can be correlated directly with bond order between atoms with a common contact surface. This takes the form shown in equation 3.1, where $S_{i,j}(\Omega_A)$ is the overlap integral between spin orbitals χ_i and χ_j within the basin Ω_A for atom A, and $\delta(A,B)$ is the resultant delocalisation index between atoms A and B. While this moves slightly away from the density-only ideal of QTAIM's topological approach, it does promise a clean and relatively simple ideal of electron sharing that would satisfy most views of covalency, and a quantitative bond index for complex systems. A 2005 paper by Bader and Cortés-Guzmán[67] was somewhat scathing of many attitudes to chemical bonding, but noted:

> The exchange of one or more pairs of electrons between bonded atoms is the mechanism essential to the notion of 'covalent bonding'. Thus, the delocalisation index $\delta(A,B)$, since it determines the number of pairs exchanged between two atomic basins, may be used to gauge the degree

of covalency. In the theory of atoms in molecules 'covalency' is replaced with the term 'shared interaction', one that invokes the role of sharing, i.e., the exchange of electrons between bonded atoms. What is important is that the delocalisation index, defined as the expectation value of the exchange operator over two atomic basins, provides a quantitative measure of the number of electrons exchanged in any given interaction thus quantifying 'covalency' for those who wish to retain the term.

$$\delta(A,B) = -2\sum_{i,j}^{N} S_{i,j}(\Omega_A)\, S_{i,j}(\Omega_B) \tag{3.1}$$

In formulation, the delocalisation index appears quite similar to the expression for Mayer bond order[68], but by partitioning using the atomic basins rather than the atomic basis function assignments, an expression that is more independent of basis set is produced. Note that this expression is dependent only on the basins and the overlap matrix, and is not dependent on the energy of any orbital.

Specialised software packages to perform QTAIM have become efficient and well-developed, however those available in this research are not yet sufficiently parallelised, or oriented towards cluster-based computing, to perform the computations required to calculate integrated properties in a short enough quantity of time to make it a routine post-processing step. Heavy atoms such as actinides also present a particular problem when calculating integrated properties, in that often care must be taken to use a sufficiently dense and extensive spatial integration grid to account for the long bonds and high density curvature near the nucleus, which further increases the computational effort. These issues mean that obtaining integrated values such as delocalisation indices is still uncommon for computational investigations, and make QTAIM in general more of a niche tool, despite the relative superficial simplicity of the technique. Most relevantly to this work, they have resulted in documented use of QTAIM for actinide compounds being extremely sparse among the literature.

When looking for covalent behaviour in a system, this work looks for a transferable, measurable trend towards an increase in density in the internuclear region, and other observable behaviour that indicates stabilisation of a polyatomic system over

its purely electrostatic attraction. This aims to be an improvement upon approaches seen in other work which attempt to infer covalency through orbital mixing or other metrics related to it which may be strongly affected by orbital energy proximity, and numerous techniques are shown below, to contrast the two approaches. It is the belief of the author that fully founded bonding trends based on spatial overlap and accumulation of internuclear density are more likely to be more widely useful and transferable than coincidental orbital energy matches between metal and ligand, and thus we expect such trends to be more useful in ligand design and selection.

3.3 Computational Details

Geometries were optimised using Gaussian 03, with the PBE functional and using the Stuttgart-Bonn relativistic effective core potentials and their associated TZP basis sets for the actinides [69, 27], and the Dunning cc-pVDZ basis sets for carbon and hydrogen. As we were primarily interested in the orbitals and wavefunction properties, we opted to fix the symmetry of the systems during the optimisation at C_{3v}. This enforces separation of the valence orbitals into the same identifiable irreducible representations, shown in figure 3.2, as in previous work. Preliminary optimisations without symmetry constraints gave differing optimal forms between actinides, but the small energy differences between forms suggest thermal rotation of the Cp rings is possible.

To prevent density catastrophes in the QTAIM results, the G03 optimal geometries were then altered, to set all the An-C distances to the mean value for each species, as in the $AnCp_4$ study. The maximum difference between mean and optimal An−C distances was 0.028 Å (for $PuCp_3$).

NPA charge and orbital analyses were performed, with the same basis sets as for the optimisations, using NBO 3.1 in both Gaussian03 and Gaussian09, as the orbital partitioning scheme differs between the version of the NBO code integrated in these two versions. The default partitioning scheme in Gaussian09 places the $5f$, $6d$, $7s$, and $7p$ for actinide atoms in the valence partition, which we have labelled Scheme 1. We have also tested a modified scheme, labelled Scheme 2, in which the $7p$ is instead placed in the Rydberg partition, as suggested by Clark et al.[41] The default partitioning scheme in Gaussian03, Scheme 3, places the actinide $6d$ and $7p$ orbitals

in the Rydberg portion of the basis.

To obtain more detailed Mulliken analysis than available in Gaussian09, single point calculations were also performed using ADF 2009, using ZORA to include scalar relativistic effects, with the ZORA TZ2P basis sets and frozen cores of [1s] for carbon atoms, and [1-5s, 2-5p, 3-5d, 4f] for actinides. The integration quality parameter was increased to 4.5 for these calculations.

To obtain wavefunction files usable for AIM analysis, we performed all-electron single-point calculations in Gaussian09, using ANO-RCC basis sets for the actinide, reduced to TZP quality using the designers' recommended method[70], and 6-31G** for carbon and hydrogen[71]. The second-order Douglas-Kroll-Hess Hamiltonian was used to include scalar relativistic effects. AIM calculations were then performed on the output from these using AIMAll, requiring the highest density quadrature on the actinide to achieve acceptable accuracy, defined as reducing the integrated value of the Lagrangian over the basin to less than 0.002 au.

Highest multiplicity in each species has been assumed throughout: 1 unpaired electron for Th(III), to 7 for Cm(III). No significant spin-contamination was found in any of the calculations, the highest being 0.002 deviation of $\langle S^2 \rangle$ from expected for $AmCp_3$ in the optimisation calculation. In reality, spin-orbit coupling effects may create non-collinear spin effects that become difficult to interpret in the later actinides, but we still expect these to be high spin, and this has been borne out in previous studies, e.g. [72].

3.4 Results

3.4.1 Geometry

Mean An-C lengths under C_{3v} symmetry are shown in figure 3.3. Unfortunately optimised geometries for the protactinium and neptunium species proved difficult to obtain; for these, interpolated geometries have been substituted, using the mean of the An-C distances for the preceding and following actinides. We suspect this difficulty is due to degeneracy near or at the optimal geometry, as shown by the half-occupied *e*-symmetric HOMO level for each in figure 3.5.

As in the $AnCp_4$, the C−C bonds of the Cp rings vary in length very little over the series, with a range of less than 0.003 Å. This implies that back-donation from

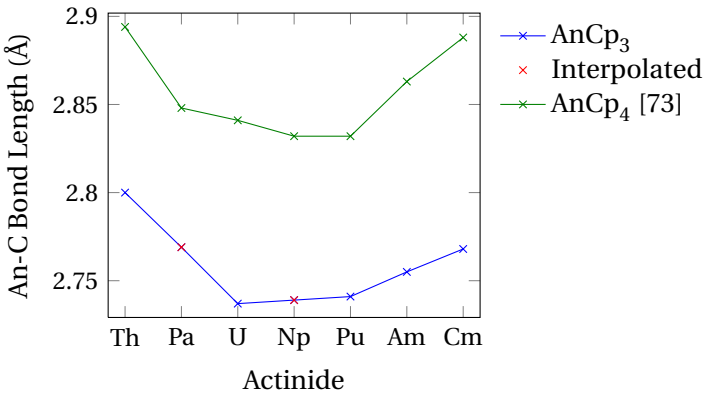

Figure 3.3: Mean actinide-carbon bond lengths for $AnCp_3$ and $AnCp_4$ (from [73], and the interpolated bond lengths used for the complexes for which optimal geometries could not be obtained.

An	An-C (mean)		An-Cp centroid		C-C (mean)		$r_{An^{3+}}$
Th	2.800	*2.894*	2.523	*2.563*	1.427	*1.417*	
Pa	2.769	*2.848*	2.481	*2.580*	1.428	*1.417*	1.04
U	2.737	*2.841*	2.453	*2.572*	1.428	*1.418*	1.03
Np	2.739	*2.832*	2.456	*2.563*	1.427	*1.418*	1.01
Pu	2.741	*2.832*	2.458	*2.563*	1.427	*1.416*	1.00
Am	2.755	*2.863*	2.474	*2.597*	1.426	*1.417*	0.98
Cm	2.768	*2.888*	2.488	*2.624*	1.427	*1.418*	0.97

Table 3.1: Selected bond lengths (Å) from $AnCp_3$ under C_{3v}, $AnCp_4$ under S_4 symmetry (in italics, from [73]), and ionic radii for the 6-coordinate An^{3+} ion (from [74]).

the actinide does not heavily affect the ring, the variance of which would be a good indication of significantly differing covalent behaviour. We do see a lengthening of approx. 0.01 Å of the bonds as compared to those in the tetravalent species, however. This could be due to slight donation of density into antibonding orbitals, or it could be due to the greater ionic attraction to the more highly charged An (IV) compressing the rings.

The An-C and An-centroid distances in table 3.1 clearly show a large deviation from the trend in ionic radii, highlighting a corresponding deviation from linear ionic behaviour. The bond lengths are also shorter for the tris-Cp than for the tetrakis-Cp, which one would expect if these distances were governed by covalent bonding, or steric hindrance between rings, but not if they were purely ionic.

3.4.2 Valence Orbitals and Orbital Decomposition

The valence orbitals of $AnCp_3$ are well-studied, as discussed above; we can locate the orbitals shown in figure 3.2 and trace their alteration across the actinides.

Figures 3.5 and 3.6 show the valence alpha orbitals for C_{3v} $AnCp_3$, as calculated with the PBE and PBE0 functionals respectively. The ligand valence orbitals shown in figure 3.2 are labelled, and excluding those in the curium species for PBE, and the americium for PBE0, they are relatively unaltered across the series. The actinide $5f$ levels stabilise across the series, however, and it is the effect of the near-degeneracy with the ligand orbitals in the two systems mentioned that causes a significant change to the orbital structure. The $6d$ orbitals do not appear to stabilise similarly due to their greater spatial extent – the orbital with highest $6d_{z^2}$ character is indicated on the diagrams and in fact appears to initially rise in energy. Although the $5f_{z^3}$ might at first appear to be a good comparison to this, it is not of the correct parity to bond well with the with the axial planar pseudo-nodal ligand orbitals, while the $6d_{z^2}$ combines readily with these.

In the PBE orbitals, as previously mentioned, the actinide orbital stabilisation increases regularly across the series, bringing the $5f$ orbitals into close energetic proximity with the ligand orbitals in the curium complex – and placing the actinide orbitals *below* the ligand orbitals in energy. This confuses attempts to track orbitals' behaviour by symmetry, as, for example, while the ordering of symmetric orbitals would suggest that the HOMO was the same a_2 orbital seen in the other species, this is in fact the corresponding anti-bonding orbital, as shown in figure 3.4b, that has been becoming progressively more stabilised and is only occupied in the curium species. The bonding a_2 orbital form (shown in figure 3.4a) followed across the series resides much lower in energy in the curium species, and is the lower of the two occupied a_2 orbitals shown in 3.5. Similarly, the highest a_1 symmetry orbital, while bonding between the rings in all cases, is anti-bonding between the actinide and the rings in $CmCp_3$ and $AmCp_3$. This occupation of strongly anti-bonding orbitals contributes to the lengthening of the An-C bonds in these species.

The PBE0 orbital diagram is more erratic than for PBE – the inclusion of exact exchange appears to have caused the f orbitals to become less closely spaced in energy, and to stabilise more rapidly, bringing them close in energy to the ligand

orbitals earlier in the series, at plutonium. The americium species orbitals are very closely spaced, over approximately 1.5 eV, with mixed ordering. By curium, the set of f orbitals are approximately 2 eV below the ligand set, and as in the PBE calculations the HOMO is now of anti-bonding character.

Mulliken decomposition for the ligand valence orbitals by symmetry is shown in table 3.2. Where the choice of orbital to include was unclear, as in the curium species, we have chosen the orbital which appeared not to be following the f orbital trend, e.g. in the PBE curium species we display values for the anti-bonding orbital, as this appears to contain the same ligand components despite having different character.

The percentage metal character shows several results; firstly, $1a_2$ orbital, which only takes metal f character, gradually rises in metal contribution to americium, as the mostly metal-based and mostly ligand-based orbitals become closer in energy. There is a small peak at protactinium, which may be ascribed to the high An f and d character orbitals being similar in energy and both readily occupied. The f and p accepting $1a_1$ orbital shows little change except for at curium in the PBE orbitals, and americium in the PBE0 orbitals – this being correlated with the point at which the trend puts the sets of metal orbitals and ligand orbitals at approximately the same energy. A similar trend is shown in the $2e$ orbital and, much smaller in magnitude, in the $1e$. The degeneracies definitely appear to be affecting the character, however the small protactinium peaks may be due to orbital overlap instead.

The metal component orbital type, as in the related $AnCp_4$ study, remains separated into mainly f-type in the $1a_1$ and $1a_2$ levels and d in the $1e$ and $2e$, optimising overlap between the differing orbital forms – the d orbitals forming more diffuse orbitals which accommodate the e combinations, and the f orbitals being more readily able to create 3-fold symmetric orbitals.

It seems clear that the anti-bonding character orbitals that become populated in the americium and curium complexes should cause a lengthening of the An-C bonds for these systems, and this is apparent in the bond lengths shown in figure 3.3. The origin of the bond shortening from Th to U could similarly be explained by an increase in population of bonding orbitals. The effect of the orbitals filled from U to Pu is less clear – they are of mixed bonding/anti-bonding character, but the

overall effect appears to be to slightly lengthen the bonds, given that the ionic radii, shown in table 3.1, monotonically decrease from Th to Cm.

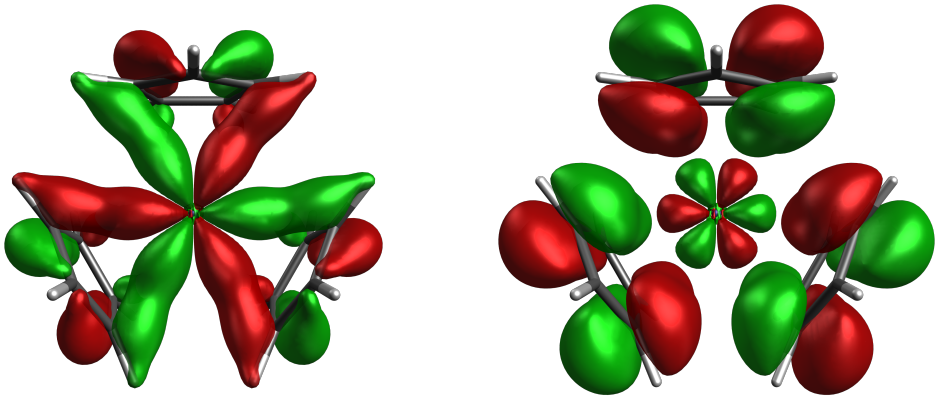

(a) **(b)**

Figure 3.4: The a_2 bonding (a) and anti-bonding (b) valence orbitals in $CmCp_3$.

Irreducible representation	Metal orbital component	Population						
		Th	Pa	U	Np	Pu	Am	Cm
$1a_2$	*f*	11.9	16.0	15.2	16.1	18.5	25.8	15.3
		11.0	*14.1*	*10.7*	*11.9*	*12.5*	*17.4*	*7.7*
$1a_1$	*f/p*	5.5	7.5	7.2	7.6	8.0	7.6	12.4
		6.1	*6.5*	*5.4*	*5.9*	*5.4*	*25.7*	*5.8*
$2e$	*d/f*	13.8	13.9	13.0	13.1	14.5	13.4	21.7
		13.6	*15.5*	*13.2*	*14.5*	*18.0*	*31.0*	*15.2*
$1e$	*d/f*	11.4	13.3	13.4	11.0	10.5	10.9	13.5
		11.9	*14.7*	*13.5*	*11.7*	*14.1*	*16.8*	*10.8*

Table 3.2: Percentage metal character in the four ligand valence orbitals. PBE values are shown in normal text, PBE0 values in italic.

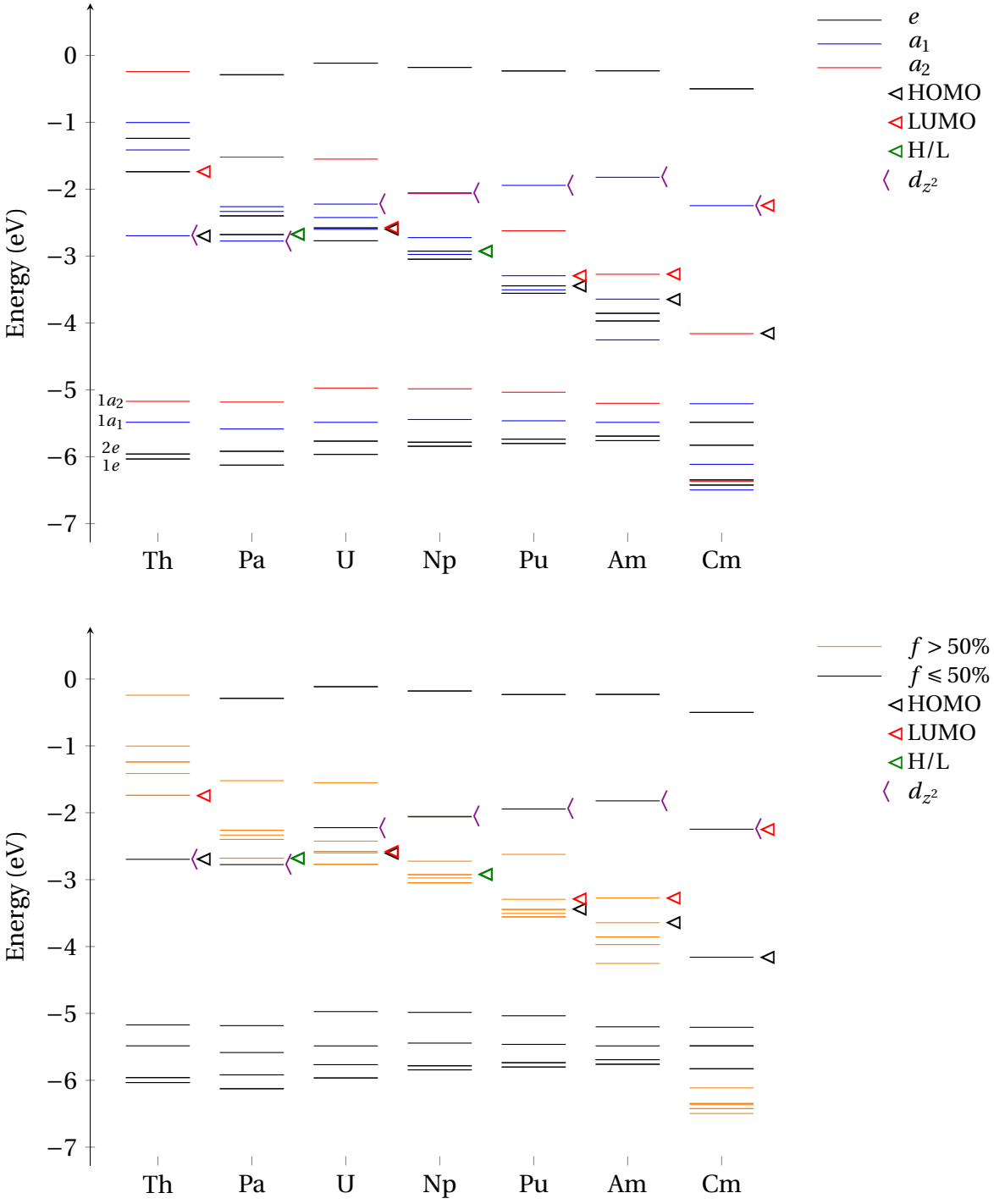

Figure 3.5: Quantitive orbital diagram for the alpha orbitals of C_{3v} $AnCp_3$, from the ADF single-point calculations at the PBE level with the TZ2P basis set, coloured by symmetry (top) and by $\%f$ orbital character (bottom). Occupied orbitals corresponding to the ligand orbitals shown in figure 3.2 are labelled for the thorium set, and the valence orbital with the highest percentage of d_{z^2} character is also indicated. HOMO and LUMO orbitals are indicated except in the case of the split HOMO/LUMO in the protactinium and neptunium results, which has been labelled H/L.

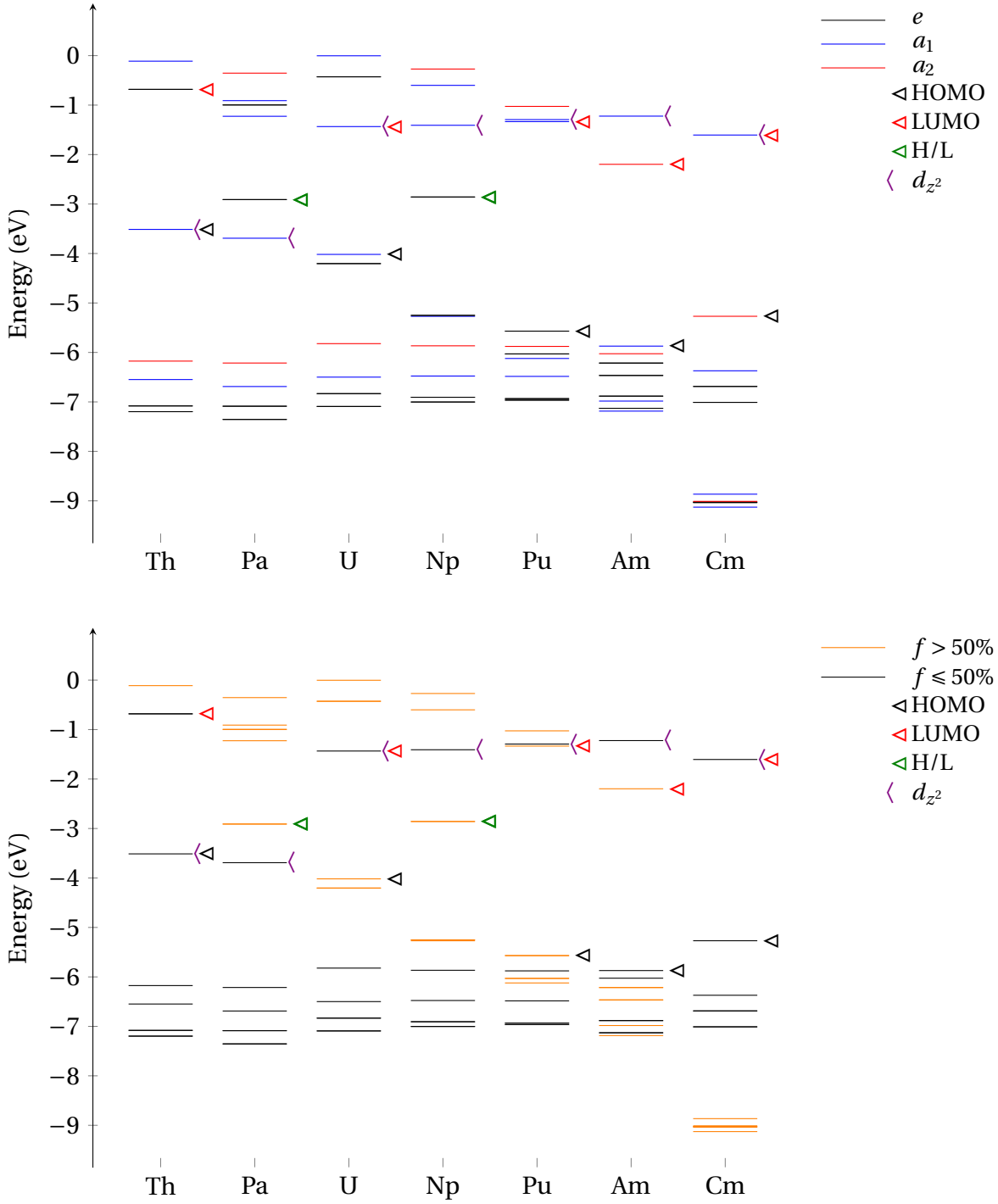

Figure 3.6: Quantitive orbital diagram for the alpha orbitals of C_{3v} $AnCp_3$, from the ADF single-point calculations at the PBE0 level with the TZ2P basis set, coloured by symmetry (top) and by $\%f$ orbital character (bottom). The valence orbital with the highest percentage of d_{z^2} character is also indicated. HOMO and LUMO orbitals are indicated except in the case of the split HOMO/LUMO in the protactinium and neptunium results, which has been labelled H/L.

3.4.3 NPA

NPA populations and charges are shown in figure 3.7. Several results can be taken from these: firstly, that scheme 3 is not an accurate representation of the actinide – including the $6d$ orbitals in the valence partition alters the assigned actinide charge significantly, much more so than adding the $7p$ orbitals. Figure 3.7b suggests that a significant quantity of density is being added into orbitals with actinide $6d$ character, consistently across the series, which is not reflected in scheme 3. Notably, this is the scheme used in the tetrakis-Cp study, suggesting that the values in that study may be artificially low also. The change from schemes 1 and 2 to scheme 3 in the $7p$ population, and the $7s$ population for thorium, would suggest that some of the density that would go toward the $6d$ population is being attributed to these orbitals, and the rest is being attributed to the ligands.

Correlating the charge on the metal, or lack thereof, with greater covalent contribution of density towards ion stabilisation, backs up the commonly accepted trend, indicating that protactinium and uranium receive the most additional density from the ligands, decreasing to curium.

The population values for protactinium contain some complex off-trend results – a higher $7s$ occupation under scheme 1, a similarly increased occupation in $5f$ for the other schemes, and an unexpectedly low charge under scheme 3. These appear to be due to the much higher use of the $6d$ orbitals for bonding in this complex, which is mis-assigned in different ways by the two schemes which assign the $6d$ orbitals to the Rydberg partition.

Certainly it seems clear that the $6d$ orbitals cannot be excluded from the valence region for the earlier actinides, and the $7p$ orbitals are also assigned a similar quantity of charge in the latter actinides and should be included.

Generally, these results show how dependent on the partitioning scheme NPA analysis can be; this is less of a problem in lighter elements, where the orbitals occupied at the valence level typically do not vary between compounds, but here, as the $6d$ becomes less occupied in favour of the $5f$, the valence orbitals are mixed and less well-defined, which makes the NPA's strict tripartite orthogonalisation process less justifiable.

It is also worth noting here that a basic interpretation of these data would seem

to suggest that the metal centres have been formally reduced – an additional electron is being added to the metallic natural orbitals over what is expected. While further analysis of the orbitals and time-dependent behaviour could reveal more complex effects, it is the assumption of this work that these systems regardless behave as An(III) systems, and that the excess density is bound in a number of interactions that cannot simply be aggregated – the oxidation state model, while useful, remains a simplistic one.

		Population - formal+deviation								
	Charge	5f		6d		7s		7p		Scheme
Th	0.88	0	0.45	1	0.92	0	0.24	0	0.28	1
	1.12	0	0.47	1	0.91	0	0.24	0	0.01	2
	2.17	0	0.50	1	-0.38	0	0.48	0	0.01	3
Pa	0.70	1	0.82	1	0.70	0	0.20	0	0.32	1
	0.93	1	0.49	1	0.71	0	0.56	0	0.01	2
	0.99	1	0.81	1	0.68	0	0.20	0	0.01	3
	1.73	1	1.38	0	0.44	0	0.17			*a*
U	0.70	3	0.47	0	1.19	0	0.13	0	0.35	1
	1.02	3	0.46	0	1.19	0	0.14	0	0.01	2
	1.94	3	0.45	0	0.33	0	0.13	0	0.01	3
	1.82	2	1.50	0	0.41	0	0.15			*a*
Np	0.81	4	0.58	0	1.04	0	0.12	0	0.35	1
	1.12	4	0.58	0	1.05	0	0.12	0	0.01	2
	1.92	4	0.59	0	0.30	0	0.10	0	0.01	3
	1.69	3	1.72	0	0.36	0	0.16			*a*
Pu	0.92	5	0.57	0	1.00	0	0.11	0	0.32	1
	1.22	5	0.57	0	1.01	0	0.11	0	0.01	2
	2.00	5	0.57	0	0.28	0	0.10	0	0.01	3
	1.75	4	1.75	0	0.32	0	0.14			*a*
Am	1.09	6	0.51	0	0.93	0	0.10	0	0.31	1
	1.37	6	0.51	0	0.94	0	0.10	0	0.01	2
	2.10	6	0.52	0	0.25	0	0.10	0	0.01	3
	2.13	5	1.44	0	0.29	0	0.13			*a*
Cm	1.30	7	0.22	0	1.00	0	0.11	0	0.31	1
	1.59	7	0.22	0	1.00	0	0.11	0	0.01	2
	2.34	7	0.22	0	0.30	0	0.11	0	0.01	3
	2.30	6	1.26	0	0.31	0	0.13			*a*

Table 3.3: Natural charges and populations for $AnCp_3$ (schemes 1-3) and $AnCp_4$ (*a*).

3.4.4 Spin Density

In the spin densities, shown in figure 3.8, there are very similar trends to those seen in the actinide dioxide solids studied by Prodan *et al.*[63], though shifted by the

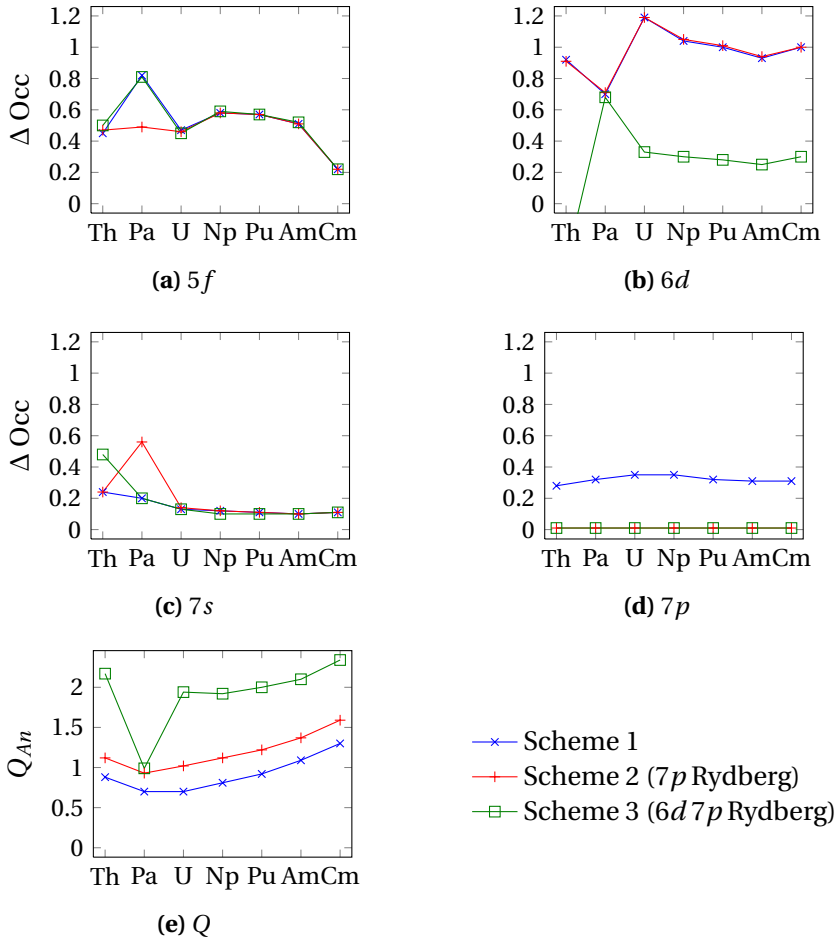

Figure 3.7: NPA actinide charges (Q) and deviations from formal occupations (Δ Occ) for the three partition schemes, using the PBE functional. Note that this assumes Th(III) is formally $5f^0 6d^1$, Pa(III) is $5f^1 6d^1$, and that other actinides are $6d^0$.

change in oxidation state. Initially in the series, there is a decrease in spin density assigned to the actinide to a minimum at protactinium, followed by an increase up to the americium species, and finally a sudden decrease to almost the formal value is observed at curium, as the complete formal $5f^7$ configuration precludes the addition of spin density. (Compare this to figure 3.7a, which shows a similar reversion towards the formal occupation.)

Before the QTAIM spin analysis was performed, it was tempting to appeal to the commonly blamed basis set dependence in Mulliken analyses, and assert that the more spatially extensive actinide-based valence orbitals could be assigned an artificially low spin density due to the equal division of charge in the calculation method (see 2.1.11.1). However, the trend in the Mulliken spin densities, albeit not the absolute values, is perfectly reproduced by the spin densities calculated from the

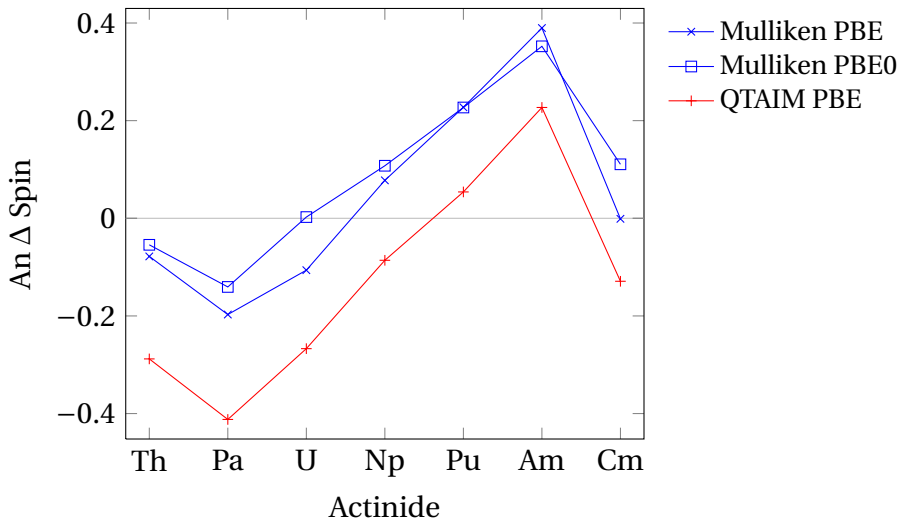

Figure 3.8: Deviation from formal integer net electronic spin (Δ Spin) on the actinide, shown by Mulliken analysis and integration of the QTAIM basins, in the $AnCp_3$ complexes. (Mulliken data taken from the all-electron calculations in G09.)

QTAIM spin basins. The overall lower values of the QTAIM spin data, however, may be assignable in part to the extension of the actinide orbitals into the carbon regions, which the actinide basins will not cover but which will be included in the actinide contribution by the Mulliken analysis.

In the actinide dioxide study, the trend seen here was attributed to the transfer of spin density from the oxygen to the actinide, the increase in which is made possible through an increase in orbital mixing across the series; they cite the orbital mixing term from first-order perturbation theory as $\frac{t_{fp}}{\epsilon_f - \epsilon_p}$, where t_{fp} is the transfer integral between the f and p orbitals. Under this scheme, the denominator becomes close to zero in near-degeneracy, despite the decrease of t_{fp} with the contraction of the orbitals with increasing nuclear charge.

While the trend shown here fits this strictly orbital-overlap-based model of covalency peaking at americium, results obtained from topological analysis show rather differing evidence.

3.4.5 Topological Density Analysis

The critical point analysis involved in performing a QTAIM calculation provides an ideal inspection of the bonding density behaviour in these systems – as they are essentially identical save for the actinide and do not vary significantly in shape, the critical point data are directly comparable. Table 3.4 shows the density (ρ), Lapla-

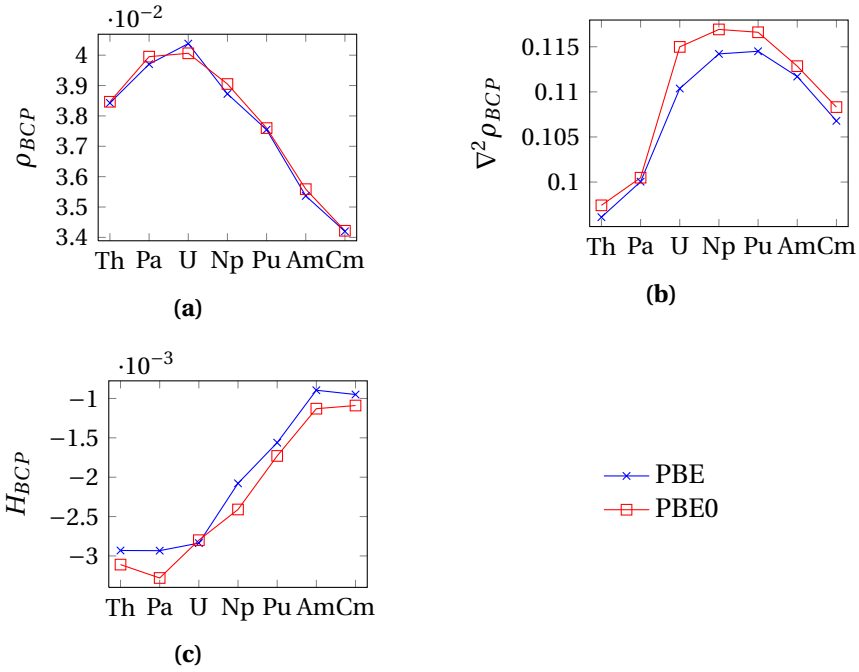

Figure 3.9: QTAIM bond critical point data plots for An-C bonds in $AnCp_3$. All quantities are in atomic units.

cian of the density ($\nabla^2\rho$), ellipticity (ε), and total energy density (H) at the critical points for the carbon-carbon bonds, and the metal-carbon bonds, for not only the $AnCp_3$ systems but also the $AnCp_4$, $LaCp_3$ and lone Cp^- ring for comparison. For ease of visualisation, figure 3.9 plots these quantities for the $AnCp_3$ set.

In contrast to the $AnCp_4$ set, the $AnCp_3$ carbon-carbon bond information shows very little deviation from the Cp^-, suggesting that the presence of the metal does not strongly perturb the bonding in the ring, however, the slight change in the ellipticity at the bond critical points does suggest the extension of the π-bonding system in the direction of the metal.

The actinide-carbon bond critical point data show several trends – firstly and most obviously, the densities at the critical point (figure 3.9a) follows a trend that corresponds very closely with the conventional view of the trend in actinide covalency. Figure 3.10 gives a more complete image of how the density varies along the An-C line, showing several distinct regions – the first being within approximately 1.1 Å of the actinide, where the density appears to be governed simply by that actinide, showing ordering purely according to the formal number of electrons on the ion (see expanded view, bottom left). Beyond that, there appears to be an interaction region,

where the density is more strongly affected by bonding characteristics than by only one atom. This region is expanded in the middle insert, showing the minima close to the critical points (the actual critical points lie slightly off the straight line path). In the limit of a long ionic bond, the density should fall to zero, and the deviation from this seen in figure 3.10 appears to give very similar behaviour overall for all the actinides in this respect. However, it also does not appear to demonstrate any behaviour which would lead to a conclusion that the later actinides were involved in a more covalent bond.

	$LaCp_3$	$ThCp_3$	$PaCp_3$	UCp_3	$NpCp_3$	$PuCp_3$	$AmCp_3$	$CmCp_3$
C-C								
ρ	0.285	0.287	0.278	0.287	0.288	0.288	0.288	0.288
$\nabla^2\rho$	-0.689	-0.683	-0.637	-0.681	-0.691	-0.689	-0.690	-0.689
ε	0.218	0.237	0.234	0.237	0.236	0.235	0.233	0.236
H	-0.268	-0.268	-0.251	-0.267	-0.270	-0.270	-0.270	-0.270
An-C								
ρ	0.031	0.038	0.040	0.040	0.039	0.038	0.035	0.034
$\nabla^2\rho$	0.090	0.096	0.100	0.1103	0.114	0.114	0.112	0.107
ε	3.81	2.78	2.25	1.16	1.89	1.92	2.20	2.64
H	0.00006	-0.00293	-0.00293	-0.00284	-0.00208	-0.00156	-0.00090	-0.00095

Table 3.4: QTAIM Bond Critical Point data calculated with the PBE functional for $AnCp_3$ systems, as well as $LaCp_3$ from [73].

	$ThCp_3$	$PaCp_3$	UCp_3	$NpCp_3$	$PuCp_3$	$AmCp_3$	$CmCp_3$
C-C							
ρ	0.289	0.280	0.289	0.291	0.290	0.291	0.290
$\nabla^2\rho$	-0.714	-0.667	-0.711	-0.721	-0.719	-0.720	-0.719
ε	0.249	0.245	0.253	0.251	0.250	0.247	0.249
H	-0.274	-0.258	-0.274	-0.277	-0.276	-0.276	-0.276
An-C							
ρ	0.038	0.040	0.040	0.039	0.038	0.036	0.034
$\nabla^2\rho$	0.097	0.100	0.115	0.117	0.117	0.113	0.108
ε	3.108	2.369	1.308	1.791	2.263	2.532	2.979
H	-0.00311	-0.00328	-0.00280	-0.00241	-0.00173	-0.00113	-0.00109

Table 3.5: QTAIM Bond Critical Point data calculated with the PBE0 functional for $AnCp_3$ systems.

	Cp^-	$ThCp_3$	$PaCp_3$	UCp_3	$NpCp_3$	$PuCp_3$	$AmCp_3$	$CmCp_3$
C-C								
ρ	0.286	0.287	0.278	0.282	0.289	0.286	0.284	0.289
$\nabla^2\rho$	-0.677	-.689	-0.640	-0.661	-0.699	-0.683	-0.672	-0.703
ε	0.278	0.221	0.216	0.212	0.213	0.209	0.215	0.203
H	-0.268	-0.269	-0.251	-0.258	-0.271	-0.265	-0.262	-0.271
An-C								
ρ		0.033	0.034	0.034	0.033	0.032	0.029	0.027
$\nabla^2\rho$		0.079	0.088	0.089	0.094	0.094	0.089	0.084
ε		3.61	3.35	2.11	2.65	2.30	2.62	2.90
H		-0.00175	-0.00137	-0.00101	-0.00074	-0.00019	0.00037	0.00047

Table 3.6: QTAIM Bond Critical Point data calculated with the PBE functional for $AnCp_4$ systems and the Cp^- ring, reproduced from [73].

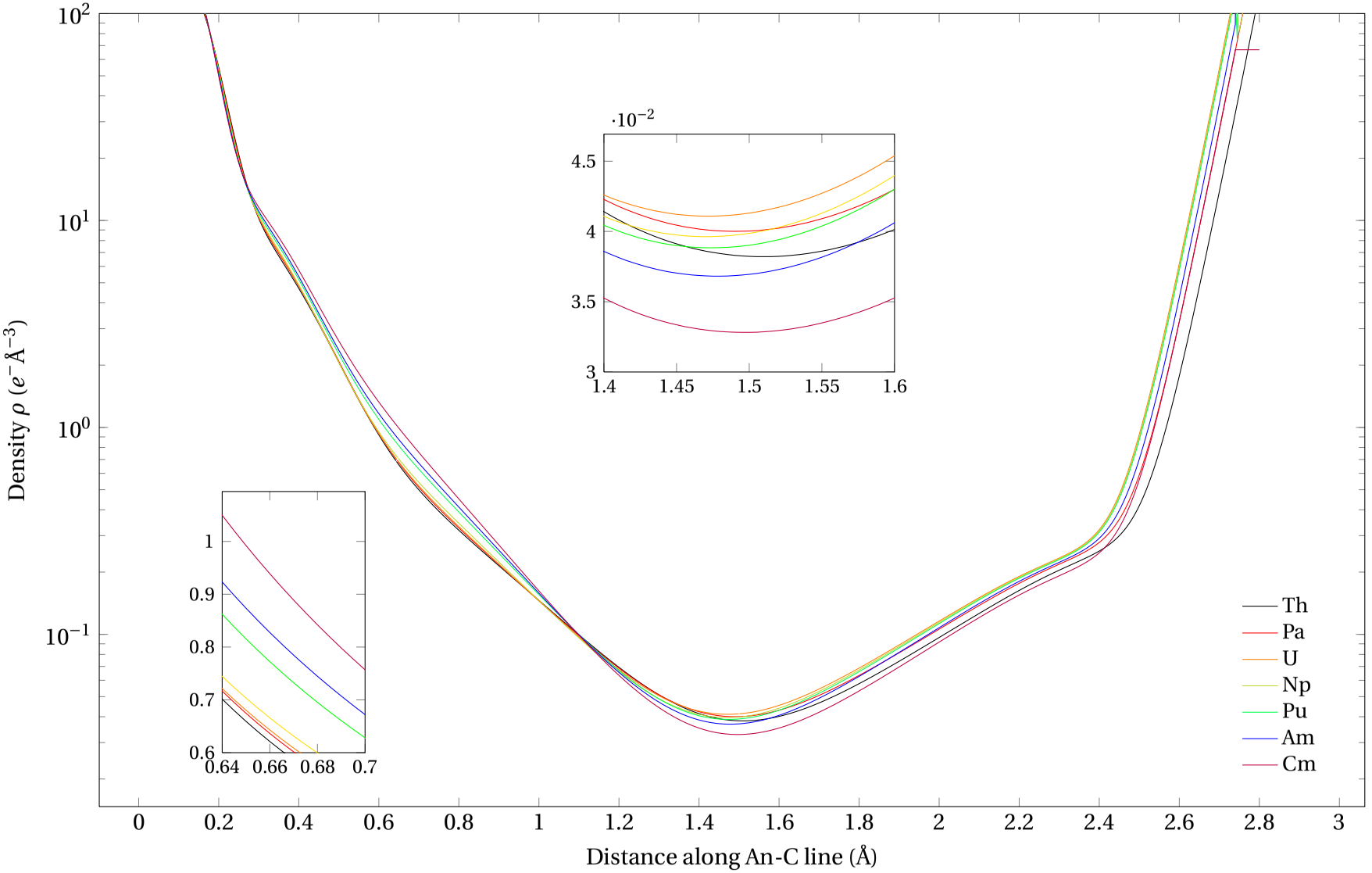

Figure 3.10: Density plotted along the vector from the actinide to the middle-top carbon of the Cp ring.

As expected, the actinide-carbon bond critical point density is also uniformly lower in the $AnCp_4$ systems compared to the $AnCp_3$ analogues.

Inspection of the values of the Laplacian, and the potential, kinetic, and total energy densities yields further information on the environment around the bond critical point. While the point-wise behaviour of the Laplacian can be unelucidating in systems with atoms beyond the second period[75], the similarity of these systems should still ensure that this value is at least usefully comparable. The values for the An-C bond critical points are positive, which indicates a degree of charge depletion in the centre of the bond. However, it is expected that these bonds will be of mixed character, so this is not surprising. Comparison between the values across the series serves to show that the mid-early-actinides, neptunium and plutonium, have the highest curvature, however this may be due to a lack of charge present generally or a local depletion, hence the drop off at each end. The differences between the values of the Laplacian are very small, however.

While clearly the total energy density (H) values at the An-C bond critical point are much smaller than those in the strong, homonuclear carbon-carbon bond, they are negative, in contrast to those of the more ionic lanthanum-carbon bonds, showing that the density in this region is more confined by attractive forces than it is repelled by electron-electron repulsion for all the species investigated here. However, this decreases across the series, meaning that this metric suggests a reduction in covalency from uranium to americium, as net forces contributing to the movement of density into the internuclear region weaken.

As previously stated, the values for each An−C bond are still much smaller than those for the a more classical example of a covalent bond, the C−C in the Cp ring, and both the values and the variation shown in them are smaller than in bond types common in organic chemistry, indicating that the overall variations in bond character are small. However, the An−C bond is also much longer than the typical organic bond, and the large spatial extent of the bonding density in these systems will produce lower densities, curvatures, and energy densities.

The final arbiters in QTAIM for bonding nature are the localisation and delocalisation indices[67]. The delocalisation index gives a physically meaningful measure of the number of electron pairs shared between two atomic basins, and in a perfectly

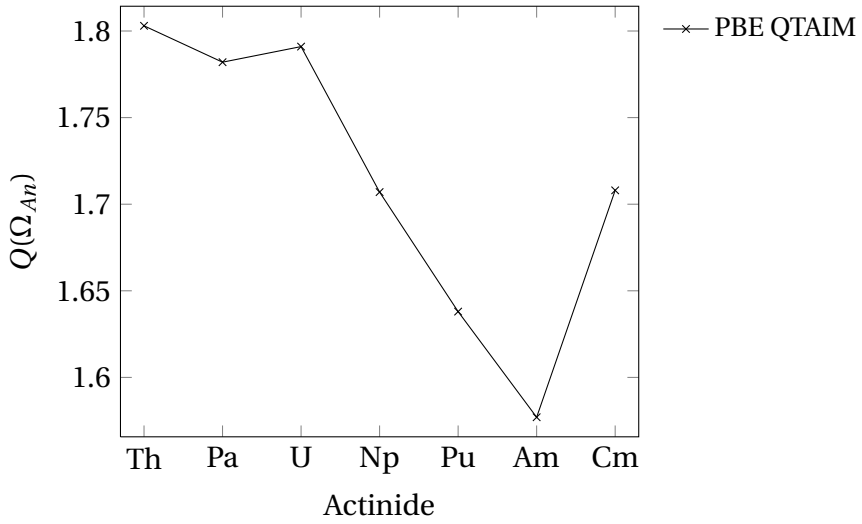

Figure 3.11: Net charge obtained by integrating the density within the actinide QTAIM atomic basin in the density of the $AnCp_3$ complexes obtained with PBE.

symmetric bond (e.g. a homonuclear diatomic) can be shown to be the equivalent of the Lewis bond order. The deviancy from the expected bond value thus gives a measure of how polar a bond is, and by summing over the delocalisation indices for the actinide with each carbon, a total for the actinide can be obtained. These values are displayed in figure 3.12 and show that, in fact, the most covalent bonding is exhibited in the protactinium species, and the later actinides exhibit more polar (and thus less covalent) bonds than thorium, presumably due to their contracted *f* density. That we see lower density at the bond critical point for protactinium than for uranium is presumably due to protactinium's larger atomic basin volume, as shown in figure 3.13.

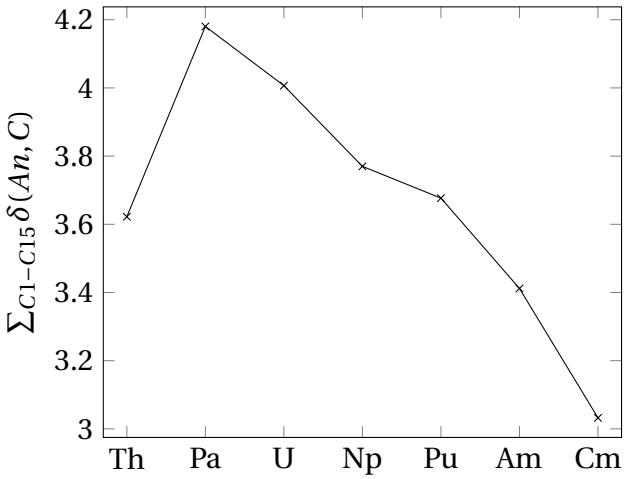

Figure 3.12: Delocalisation indices for the An-C bonding interactions summed over all An-C pairs in each $AnCp_3$ system, calculated with the PBE functional. (See eq. 3.1 for definition.)

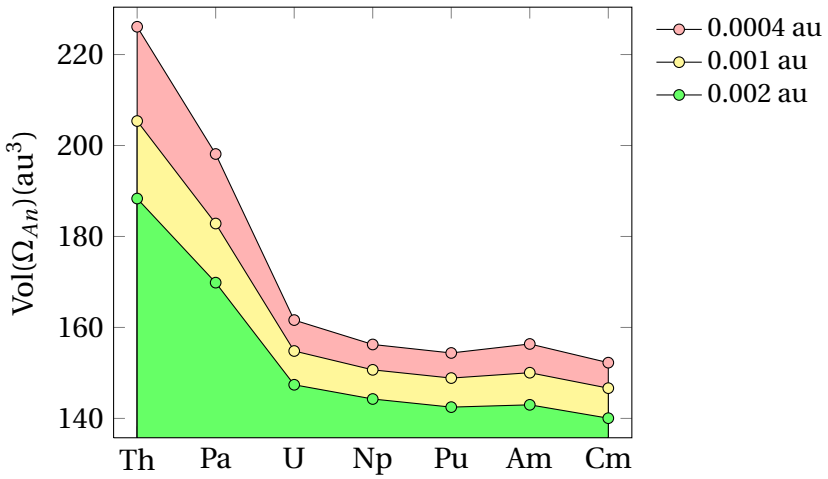

Figure 3.13: Volume of the QTAIM actinide atomic basin in $AnCp_3$ calculated with PBE, bounded by successive isodensity envelopes.

3.5 Conclusions

These compounds appear to be a somewhat pathological case for many forms of analysis – MO-based analysis methods are less clear than usual due to a combination of effects: the mismatch in atomic basis size, which causes equipartitioning to fail and induces basis set superposition problems; the change across the series in the relative energies of the d and f orbitals, which makes analysis of the orbital usage more complex, confusing the NPA and requiring careful choice of partitioning to obtain any consistent data; and strong orbital mixing in the americium and curium induced by close energy matching, which confuses issues of attempting to determine bonding and behaviour based on mixing, especially in near-edge XAS where more discriminatory data may not be available.

There certainly appears to be a complex phenomenon at play here, due to this enhanced mixing in the mid-actinides, however, it does not appear to significantly affect trends obtained from density-based analysis, which leads to the hypothesis that it may not affect bonding energies, either. Unfortunately, accurate measurement of bonding energies for this type of system in solution (the environment desired for actinide extraction) is currently extremely costly computationally (see chapter 5).

For now, it must suffice to note that commonly used methods to infer types of bonding may not give unambiguous results or follow common assumptions for this variety of system, and great care should be taken when drawing conclusions from incomplete data.

The QTAIM technique appears to give results that follow commonly understood trends here – that is not sufficient to confirm either as an accurate reflection of reality, however QTAIM's sound physical basis, emphasis on rigorously defined physical concepts, and more direct linkage to concepts like covalency often inferred using other data leads to the conclusion that it should be a reliable technique for these and other systems that prove otherwise difficult to characterise conclusively.

Fortunately, an opportunity arose to verify and employ these techniques to investigate a related system with similar degeneracy-based mixing, which is the subject of the next chapter.

On a less general note, it appears that protactinium may be able to form the

highest-order bond due to the use of both d and f orbitals in bonding, closely followed by uranium. The delocalisation indices point towards at least one whole Lewis-type bond per ligand across the series, which is indicative of an actinide-ligand bond with significant covalent character, although the density is extremely widely spread. Unfortunately, due to difficulties involved in the experimental use of protactinium, it seems unlikely that the relative bond strengths of these two complexes will be tested within the foreseeable future.

Obtaining experimental bond energies for these and other full ranges of early actinide compounds could certainly help elucidate correlations which may be present between the calculated computational parameters presented here and practical measurables, and more direct comparison between experimentally and computationally obtained crystal densities could also help pave the way in this regard.

3.6 Publishing Notes

Work included here was published in: Ian Kirker and Nikolas Kaltsoyannis. Does covalency really increase across the 5f series? A comparison of molecular orbital, natural population, spin and electron density analyses of $AnCp_3$ (An = Th-Cm; Cp = $\eta_5-C_5H_5$). *Dalton Transactions*, 40(1):124+, 2011.

Chapter 4

Covalency in Actinide Complexes II: β-Ketoiminates

This study extends work performed in collaboration with experimentalists at the University of California, Santa Barbara and the Los Alamos National Laboratory[77], in which a series of actinide compounds of the form $An(^{Ar}acnac)_4$, An ∈ {Th, U, Np, Pu}, ^{Ar}acnac = $(tBu_2)PhNC(Ph)CHC(Ph)O$ as shown in figure 4.1a (systematic name: N-(3,5-tBu-phenyl)-1,3-diphenyl-3-hydroxyl-propaniminate) were synthesised, and analogous systems inspected computationally, with the aim of identifying bonding trends across the actinides. Subsequently, the range of actinides used computationally was expanded, and this chapter investigates trends arising from the resultant wider series of compounds.

4.1 Introduction

Building on the investigation of the tris-cyclopentadienyl compounds, this study uses similar methods to probe the bonding in a series of novel actinide (IV) compounds. The ^{Ar}acnac ligand has been used previously with actinides to make $AnI_2(^{Ar}acnac)_2$ for uranium and plutonium[78], however to obtain a range of similar compounds, the relatively simple and powerful synthetic method used here (salt elimination) allows application to a range of actinides. Experimentally, $An(^{Ar}acnac)_4$ was obtained for thorium, uranium, neptunium, and plutonium, however, structural information on the neptunium complex could not be obtained due to the rapid degradation of the crystals.

This type of ligand in particular provides an opportunity to inspect two of the

principal bond types featured in the separation of actinides in aqueous waste, An−N and An−O. It is expected in this comparison that an actinide-nitrogen bond would respond more strongly to changes in bonding, due to its proclivity for softer bonding, giving also both expected 'hard' and 'soft' bonds to the actinide in the same ligand.

In the $AnI_2(^{Ar}acnac)_2$ work, it was expected that the the harder oxygen binding would likely follow a trend closely related to the ionic radius of the actinide, while the softer nitrogen donor in the An−N bond might exhibit behaviour based on more sophisticated bonding trends. In fact, both bond types exhibited unexpected patterns, with the U−O and Pu−O distances being the same to within the experimental error, and the U−N and Pu−N distances displaying only slightly more shortening than the corresponding actinide ionic radii. Use of computational methods including Natural Resonance Theory led to the attribution of the trend in An−O bond to higher orbital overlap in the uranium compound, creating a stronger and shorter bond than expected from a predominantly ion-governed bonding model, and a lack of evidence of large bonding differences in the An−N bond led to the conclusion that the shortening was simply due to actinide contraction.

Much experimentation on actinide ligand coordination focuses on the An(III) ion to due the desire to separate out these from Ln(III), e.g. [59, 60]; however, wider information on other oxidation states may allow easier, cleaner, or more refined separation techniques. The number of oxidation states the early actinides present combined with the difficulties of working with them mean that any opportunity to make a computational link with experimental data is valuable, allowing extension and validation of techniques on both sides.

Computational analysis is especially important in this type of study, as drawing conclusions about covalency based on structural information may be unreliable due to low-curvature potential surfaces associated with bonds in molecular actinide complexes [79].

Unfortunately due to the scaling behaviour of DFT and the limits of the resources available, for the more expensive model systems it was necessary to remove some sections of the ligand used in the experiment that were thought not to play a significant role in the bonding. The larger ^{Ar}acnac ligand used in the experiment is shown in figure 4.1a, while the smaller ^{Ph}beki ligand used for the majority of the

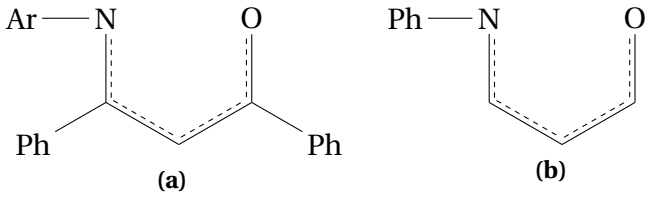

Figure 4.1: The [^{Ar}acnac]$^-$ ligand used experimentally (a), and the simplified [^{Ph}beki]$^-$ ligand used for the majority of the calculations (b), both in deprotonated form.

computational investigation is shown in figure 4.1b. For initial work, a partially trimmed ^{Ph}acnac ligand was used, missing only the ^{t}Bu groups on the *N*-arene group of the experimental ligand.

In the structure of An(^{Ar}acnac)$_4$, the phenyl ring geminal to the nitrogen is twisted out of the N-O annular plane (see figure 4.2), so should contribute very little to the delocalised ligand orbitals of the metal-ligand bonding region of the ligand, while the ^{t}Bu groups on the N-arene are expected to have primarily steric effects upon the structure. This does mean that many steric interactions and possible π-stacking interactions may not be observed in the smaller ligands, but should not drastically affect the bonding around the actinide unless steric effects cause large changes in the large ligand system. The removal of the phenyl ring coplanar to the N−O is more likely to alter the energies of orbitals bonding to the actinide, however, and thus the effect of simplifying the ligand is examined below.

4.2 Computational Details

Optimisations were performed under C_2 symmetry, using the ADF 2010.02 code[42, 43], with only the PBE functional for the ^{Ph}acnac compounds, and the PBE and PBE0 functionals for the ^{Ph}beki compounds. The ADF Slater-type basis sets were used, at TZP quality, with 5*d* and lower orbitals frozen for the actinide, and DZP quality for other atoms, with 1s orbitals frozen for carbon, oxygen, and nitrogen. Relativistic effects were included using the scalar ZORA method. Mulliken analyses including spin density data and orbital compositions were obtained from these calculations. Fermi smearing across 0.002 au was used to aid SCF convergence and to allow convergence of potentially multiconfigurational systems. An integration parameter of 4.5 was used to slightly increase the accuracy of the density model at minor computational cost.

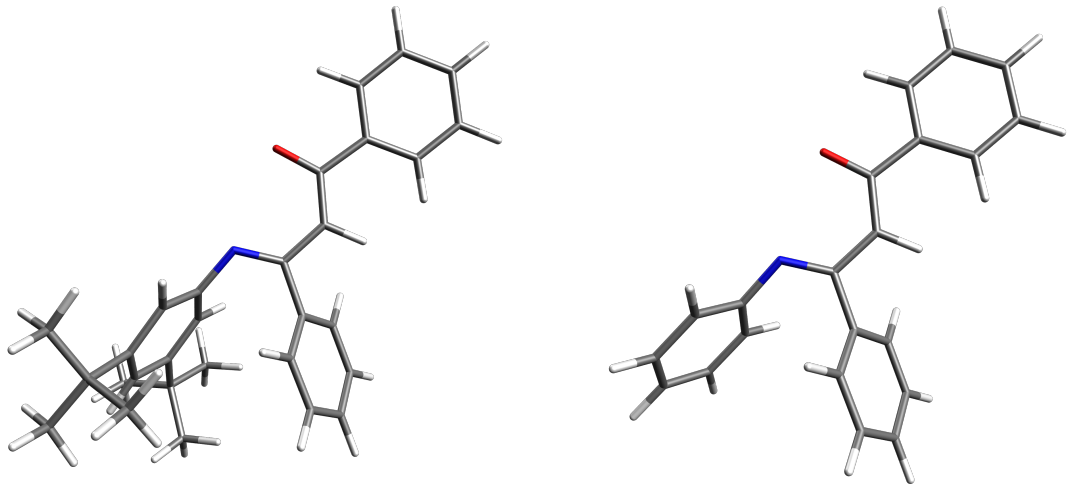

(a) **(b)**

Figure 4.2: The ^{Ar}acnac (a) and ^{Ph}acnac (b) ligand geometries from the plutonium complex, showing the deviation from planarity in the *N*-substituent and adjacent rings.

Single point calculations were performed upon both sets of optimised geometries, using the same functional, in Gaussian09, with the SARCP TZP-quality basis set on the actinide ([9s]20s[8p]12p[7d]9d[6f]6f1g)[80], and 6-31G** on all other atoms[71]. Point nuclei were used with the SARC basis set, as recommended, rather than the default Gaussian nuclei. NPA was also performed at this step. 'Ultrafine' integration grids were used to ensure sufficiently accurate quadrature around the actinide nuclei. Output wavefunction files from these calculations were then used with AIMAll to perform QTAIM analysis.

The initial PBE optimisations and AIM calculations upon the An(^{Ph}beki)$_4$ complexes were performed by N. Kaltsoyannis rather than this author and obtained with no attached analysis.

As in the previous chapter, high spin states for the actinides have been assumed: from 0 unpaired electrons in the thorium complexes to 7 in the berkelium.

4.3 Results

4.3.1 Ligand Comparison

To demonstrate the validity of the use of simplified ligands, the An−O and An−N bond distances for the experimental structures (with the ^{Ar}acnac ligand), the struc-

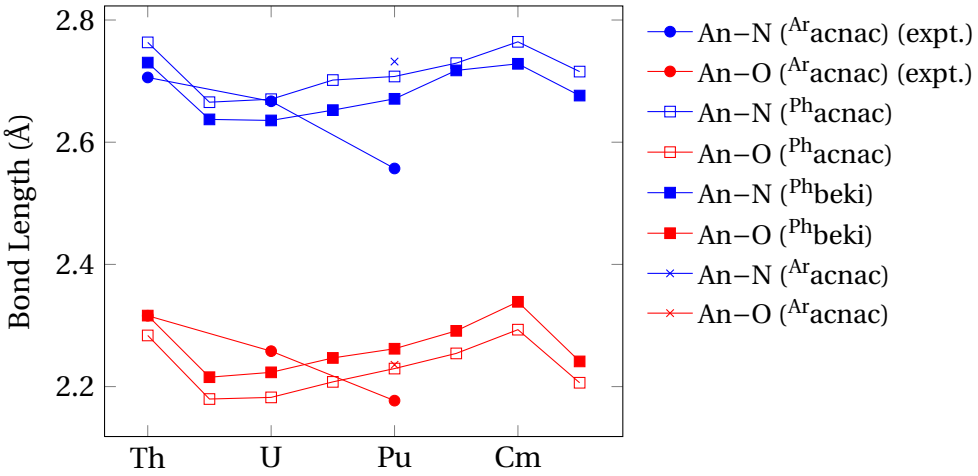

Figure 4.3: Average An−N and An−O bond length comparisons for actinide complexes with the ^{Ar}acnac ligand, measured experimentally, and the complexes optimised computationally with PBE with ligands ^{Ph}acnac, ^{Ph}beki, and ^{Ar}acnac.

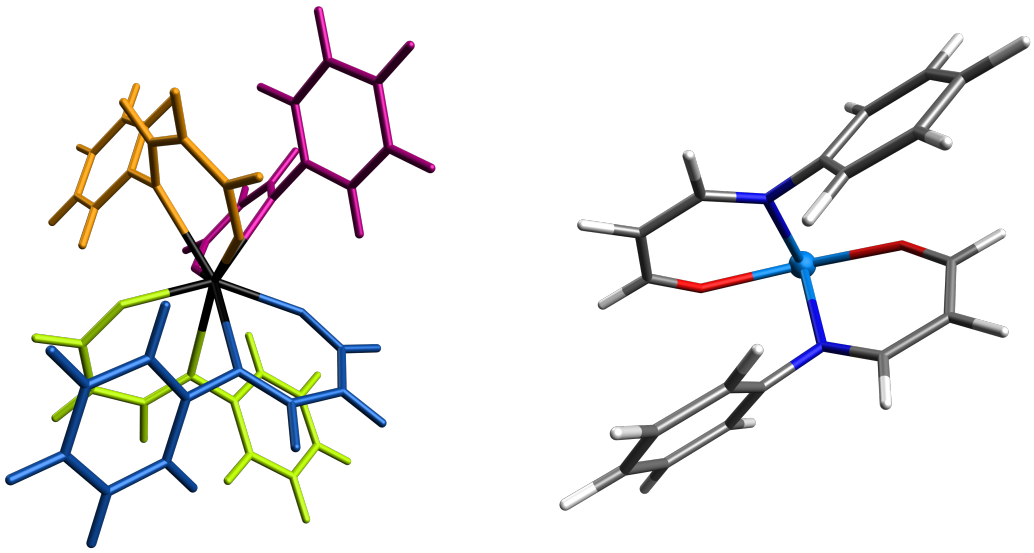

(a) **(b)**

Figure 4.4: The general An(^{Ph}beki)$_4$ structure as exemplified by the geometry for the uranium complex, in (a) with ligands block-coloured to show each, and in (b) with two of the ligands removed to show the structure more clearly.

tures with the ^{Ph}acnac ligand, and the structures with the ^{Ph}beki ligand are shown in figure 4.3, optimised with the PBE functional. The geometries obtained are approximately S_4 symmetric, however ADF does not include the option to maintain this symmetry group, hence the use of the C_2 subgroup. In each geometry, the ligands are arranged as shown in figure 4.4, with two sets of two counter-stacked ligands, forming a distorted pseudo-tetrahedral arrangement.

From the ^{Ph}acnac complexes to those with ^{Ph}beki, the arrangement of the ligands appears to alter to make the two bonds to the metal more similar in length, without altering the average of the two significantly. The overall trend in bond lengths does not appear to be altered, suggesting that any differences in bonding characteristics should be reproduced.

It is clear, however, that while the the trend in bond lengths is unchanged between the two computational model ligands, the experimental trend is not reproduced in either case. This suggests a failure of the PBE functional to accurately reproduce the density characteristics for these systems, prompting a re-evaluation of the functional used. GGA functionals in general are known to over-delocalise orbitals due to the one-electron exchange term (e.g. [81]), and including a component of exact Hartree-Fock exchange may remedy this and give better results. Particularly suggestive of this is that the best matching between bond lengths occurs in the thorium compound, which should have the simplest electronic interaction due to the thorium (IV) ion's tendency to form more ionic bonds than uranium and plutonium. In addition, the previous work on uranium and plutonium mixed halide/^{Ar}acnac complexes using an unspecified hybrid functional obtained bond length differences from changing the actinide that matched those obtained from experiment, albeit with uniformly ~0.03Å longer An−O bonds and ~0.06Å longer An−N bonds[78], suggesting that these calculations may at least model the difference but may generally underbind. To include a component of exact exchange, then, the step was made to the PBE0 functional.

As an additional test that the initial ligand pruning is not responsible for the deviation from experiment of the bond lengths, a single optimisation using the full ^{Ar}acnac ligand was performed for the plutonium complex, and is also shown in figure 4.2. The resulting structure shows that using the full ligand does not improve the agreement with experiment for the PBE functional.

Unfortunately, the PBE0 functional is too computationally expensive to use for the optimisation of the complexes with ^{Ph}acnac here, so data with the PBE0 functional have been obtained for the ^{Ph}beki complexes only.

The valence orbitals of the [^{Ph}beki]$^-$ and [^{Ph}acnac]$^-$ were also inspected to determine how the simplification would affect the ligand orbitals. To do this, the geome-

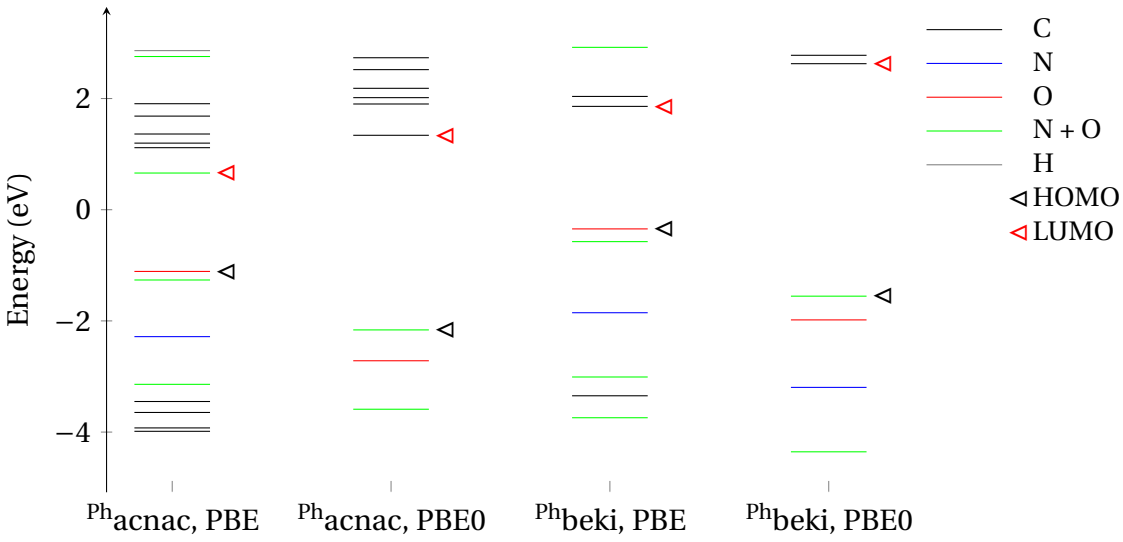

Figure 4.5: Ligand valence orbital energies for ^{Ph}acnac and ^{Ph}beki, coloured by significant atomic orbital components.

tries for each of the ligands were cut from the uranium complex structure optimised with the PBE functional, and single-point calculations were run with both PBE and PBE0. The resulting valence orbital energies are shown in figure 4.5.

4.3.2 PBE0 Geometries

Unfortunately, two of the ^{Ph}beki complexes, the neptunium and americium variants, proved too difficult to optimise using PBE0 – the standard BFGS methods that proved effective for the other systems oscillated between two geometric configurations, neither of which was a stable geometry. Modifications to the method to attempt to smooth the potential surface and to reduce the magnitude of the geometry changes both proved ineffective, as did altering the initial geometry of the complex. Due to the high computational cost of PBE0 and the lack of success of these modifications, it was decided to abandon these two complexes and focus on the other data.

The averages of An−O and An−N bond distances for the experimental structures and the ^{Ph}beki complexes optimised with PBE and PBE0 are shown in figure 4.6. The use of PBE0 appears to bring several of the bond lengths closer to the experimental data, significantly improving the Pu−N bond length match, but it also produces a less good match for the U−N bond length. Table 4.1 shows the mean absolute deviations for the calculated values for the two bond lengths from the three

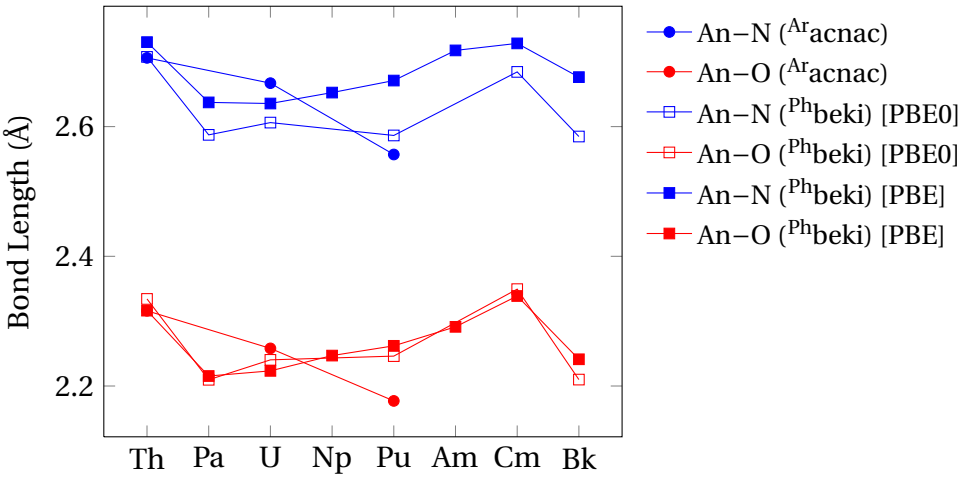

Figure 4.6: Average An−N and An−O bond length comparisons for the experimental ^{Ar}acnac complexes, and the ^{Ph}beki complexes optimised with PBE and PBE0.

	Mean Absolute Deviation (Å)		
Func.	An−N	An−O	Both
PBE	0.057	0.040	0.048
PBE0	0.031	0.035	0.033

Table 4.1: Mean Absolute Deviations from experimental values[78] for the An−N and An−O bond lengths for An ∈ {Th, U, Pu} as optimised with PBE and PBE0.

experimentally determined structures, confirming that overall PBE0 gives more similar bond lengths.

For the uranium and plutonium geometries, the structural alterations also appear to alter the trend in bond lengths in a way that reproduces that seen in the $AnI_2(^{Ar}acnac)_2$ complexes[78], making the An−O bond lengths very similar and the An−N lengths exhibit slight contraction. This breaks with the trend created by the PBE data, and suggests not only that the PBE0 functional is modelling the orbitals involved in the bonding more accurately, especially in the case of the Pu−N bond, but that the Pu−N bond is susceptible to the modifications in orbitals caused by this functional change, hinting at covalent bonding character.

Despite the similarity in average bond length, the curium complex displays a marked difference between PBE and PBE0 geometries – the PBE0 exhibits a marked breaking of the approximate S_4 symmetry. All the geometries display small deviations from S_4 simply due to the maintenance only of C_2 symmetry combined with relatively loose convergence criteria, however, as shown in figure 4.7, by far the

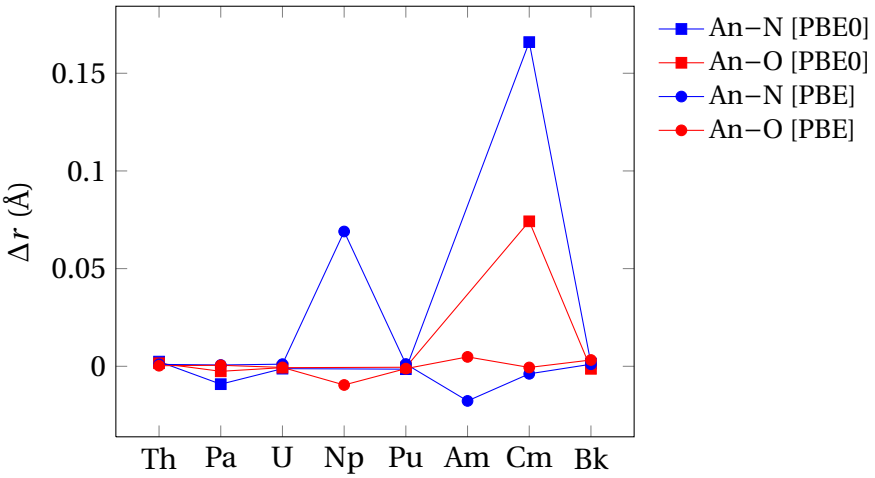

Figure 4.7: The difference between the sets of bond distances for the two pairs of ligands in the ^{Ph}beki complexes. (Sign preserved to show correlation.)

largest occurs in the curium complex.

Figure 4.8 shows the HOMO (a) and LUMO (b) of this complex, which illustrate this asymmetry. The HOMO and LUMO are a pseudo-symmetric pair, representing the same components on opposite pairs of ligands, and the occupation of only one of the pair asymmetrises the molecule away from pseudo-S_4. To evaluate the energetic benefit of the asymmetrisation, the structure was re-optimised with all the Cm−O bonds constrained as equal. This gave a structure only 5.7 kJ/mol higher in energy, suggesting a low-curvature potential surface for this change.

Single-point calculations with PBE0 were run on altered geometries for the uranium and plutonium complexes, to similarly make an assessment of the energy surface for the bond lengths for which experimental data were available and which were not improved moving from PBE to PBE0. The U−N bond length in the uranium complex was altered to the experimental value, keeping the optimised U−O bond length. This raised the SCF energy of the system by only 1.5 kJ/mol, showing that this geometry is readily flexible.

For the plutonium complex, the geometry was altered, moving each ligand as a block to have the experimental Pu−O bond length, keeping the optimised Pu−N bond length, as the Pu−O distance shows the most deviation from the experimental value and trend (albeit a trend over only three bond lengths). This single-point calculation gave a total bonding energy increase of 9.3 kJ/mol over the optimised structure, larger than that for the uranium and curium complexes but still indicative

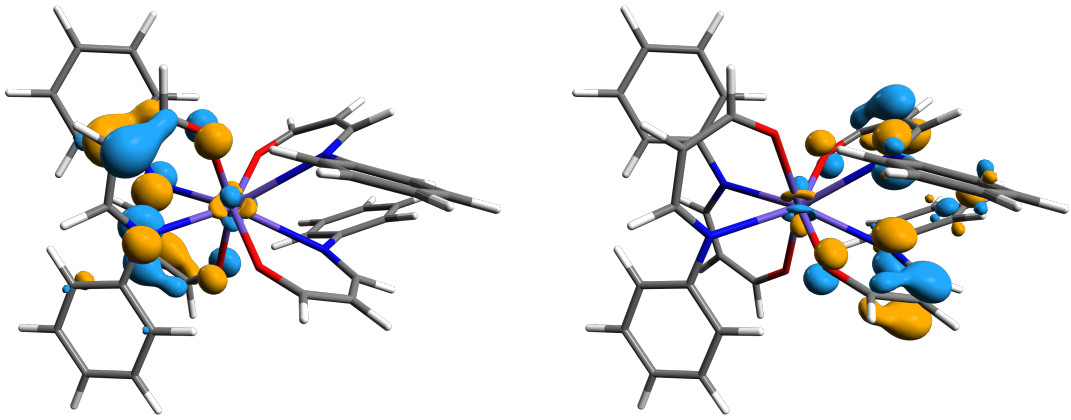

(a) HOMO **(b)** LUMO

Figure 4.8: The HOMO and LUMO of Cm[^{Ph}beki]$_4$, at a high isosurface definition value of 0.06 $e^{\frac{1}{2}}$Å$^{-\frac{3}{2}}$ to aid comparison. The positive phase regions of the orbitals are shown in light blue, the negative phase in orange.

of a flexible structure.

These energy differences highlight the conclusions of Minasian et al. [79] - that the geometries in these structures can easily be changed by slight differences in environment due to the low curvature of the potential surfaces of actinide-ligand bonds in molecular complexes.

4.3.3 Valence Orbitals and Orbital Decomposition

The energies of the valence orbitals and low-lying virtual orbitals for the ^{Ph}acnac complexes with PBE, and the ^{Ph}beki complexes with PBE and PBE0, are shown in figures 4.9, 4.10, and 4.11 respectively.

Similar trends to those seen in the tris-Cp complexes can be observed in the orbitals calculated with PBE, with the actinide f-orbitals becoming more stabilised across the series, and becoming increasingly mixed with the ligand orbitals as the two sets become closer in energy. In the curium ^{Ph}beki complex, as in the previously shown americium tris-Cp complex (and, to a lesser extent, the curium tris-Cp complex), the f-orbitals become strongly mixed with many ligand orbitals, and the energy of the highest occupied ligand orbital is raised in energy above the primarily actinide-based levels. Past curium, in the berkelium compound, the actinide levels

Actinide	Orbital Energy (eV)	Occupation
Am	-4.933	0.56
	-4.928	0.44
Cm	-5.023	0.52
	-5.021	0.48

Table 4.2: Partially occupied orbitals in the An(^{Ph}acnac)$_4$ complexes, calculated with PBE.

Actinide	Orbital Energy (eV)	Occupation
Am	-5.058	0.61
	-5.051	0.39
Cm	-5.092	0.52
	-5.091	0.48

Table 4.3: Partially occupied orbitals in the An(^{Ph}beki)$_4$ complexes, calculated with PBE.

have dropped below the ligand valence levels, which near the HOMO are similarly structured to the weakly-perturbed ligand orbitals from thorium to plutonium.

Interestingly, in the ^{Ph}acnac systems, there is also a block of virtual orbitals that becomes mixed with the protactinium *f* orbitals as they become close in energy. This appears to act to lower the actinide contribution to the HOMO – the HOMOs in the ^{Ph}acnac and ^{Ph}beki PBE orbitals have 35% and 47% Pa character respectively.

It should be noted that in the PBE orbitals, due to the electron smearing technique used and the probable multiconfigurational nature of the compounds, the americium and curium variants have fractionally occupied orbitals as their highest (partially) occupied orbital – these have been marked on the orbital diagrams as occupied, while details are shown in tables 4.2 and 4.3. The symmetry breaking observed in the curium complex PBE0 geometry above is then a consequence of the energetic preference towards integer occupations by the form of the PBE0 energy expression. The difficulties obtaining the geometries of the americium and neptunium ^{Ph}beki complexes with PBE0 are also likely a consequence of this, with forced single determinantal character creating an artificial transition state very close to the optimum geometry.

The energies of the PBE0 orbitals show several marked differences to the PBE orbitals overall. The occupied PBE0 ligand orbitals appear to begin around 1 eV lower in energy than the PBE equivalents, as observed in the ligand-only calculations, and the actinide *f*-based orbitals appear to stabilise more rapidly across the

series, putting them well below the highest lying ligand orbitals in the plutonium system rather than at the HOMO as they are in the PBE orbitals. Despite this, a large mix of highly blended orbitals does not appear in the PBE0 plutonium compound orbitals, which instead combine with only the highest-lying ligand orbitals.

For the berkelium system, no orbitals with significant f character are shown in the diagrams, as the α orbitals with high berkelium f character drop far below the displayed region, in the case of the PBE0 orbitals down to 11 eV. However, while in the other actinide complexes, the f β orbitals do not mix with the occupied ligand orbitals, in the case of berkelium there are three β orbitals with approximately 2% f character, at -6.430, -6.431, and -6.728 eV (HOβMO, HOβMO-1, and HOβMO-3). This serves to demonstrate the magnitude of the energy differences between the α and β actinide $5f$-based orbitals in these compounds, and also indicates that β density present in the actinide valence orbitals will slightly reduce the spin density for the berkelium in this compound.

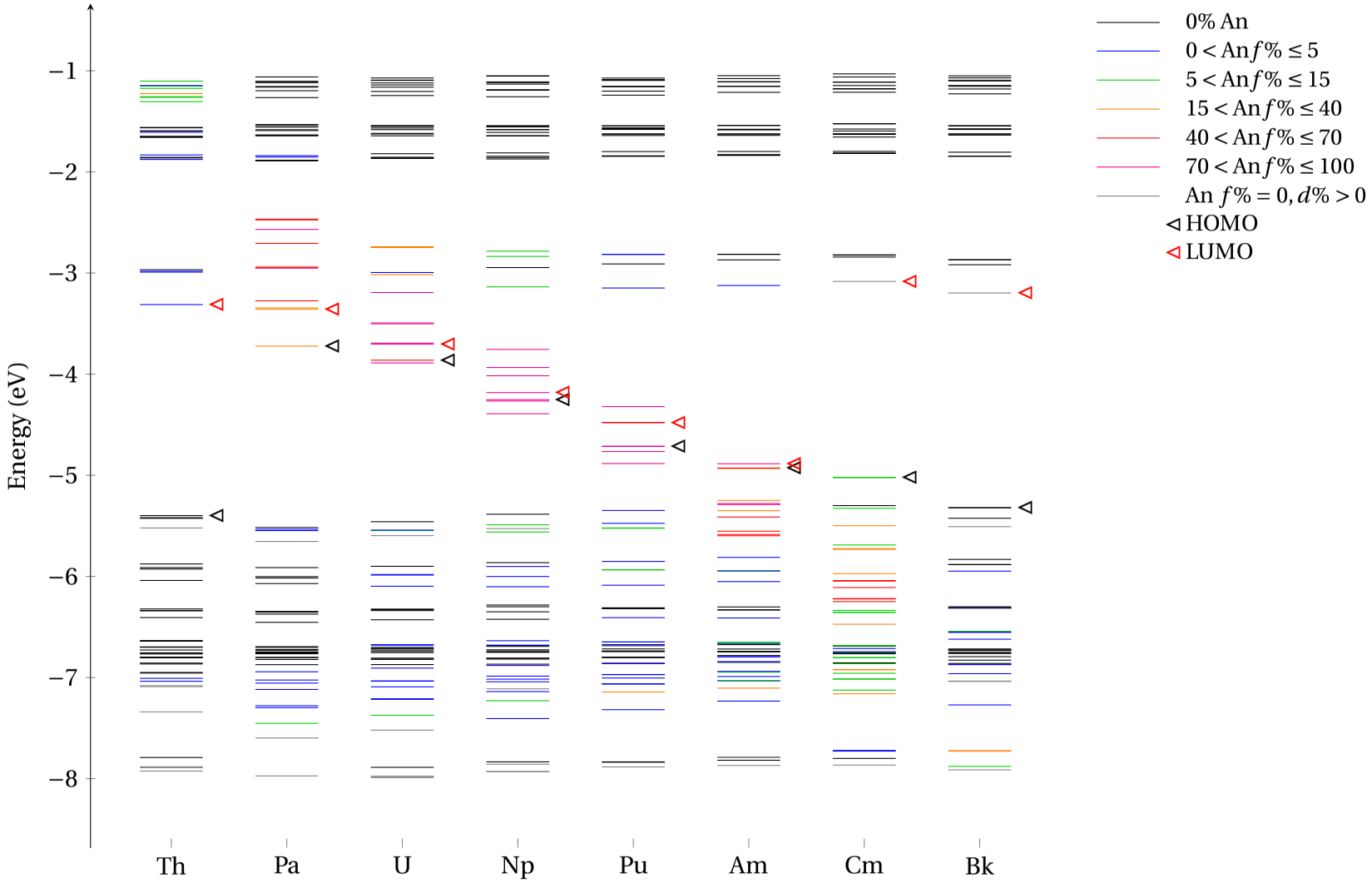

Figure 4.9: Valence α-spin orbitals between −8 and −1 eV for the An(^{Ph}acnac)$_4$ complexes, calculated with PBE, coloured to show the An f character in the orbital.

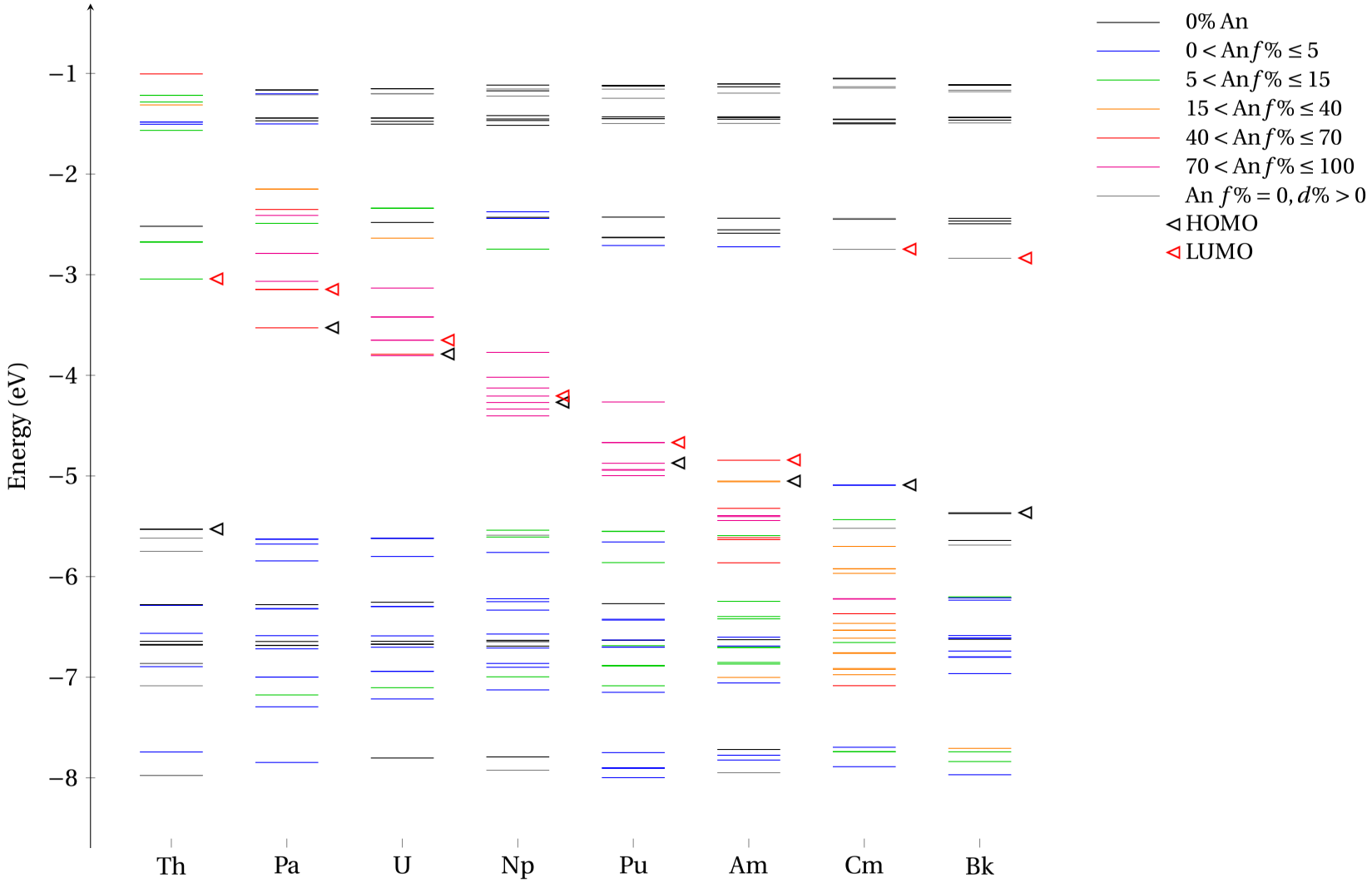

Figure 4.10: Valence α-spin orbitals between -8 and -1 eV for the An(^{Ph}beki)$_4$ complexes, calculated with PBE, coloured to show the An f character in the orbital.

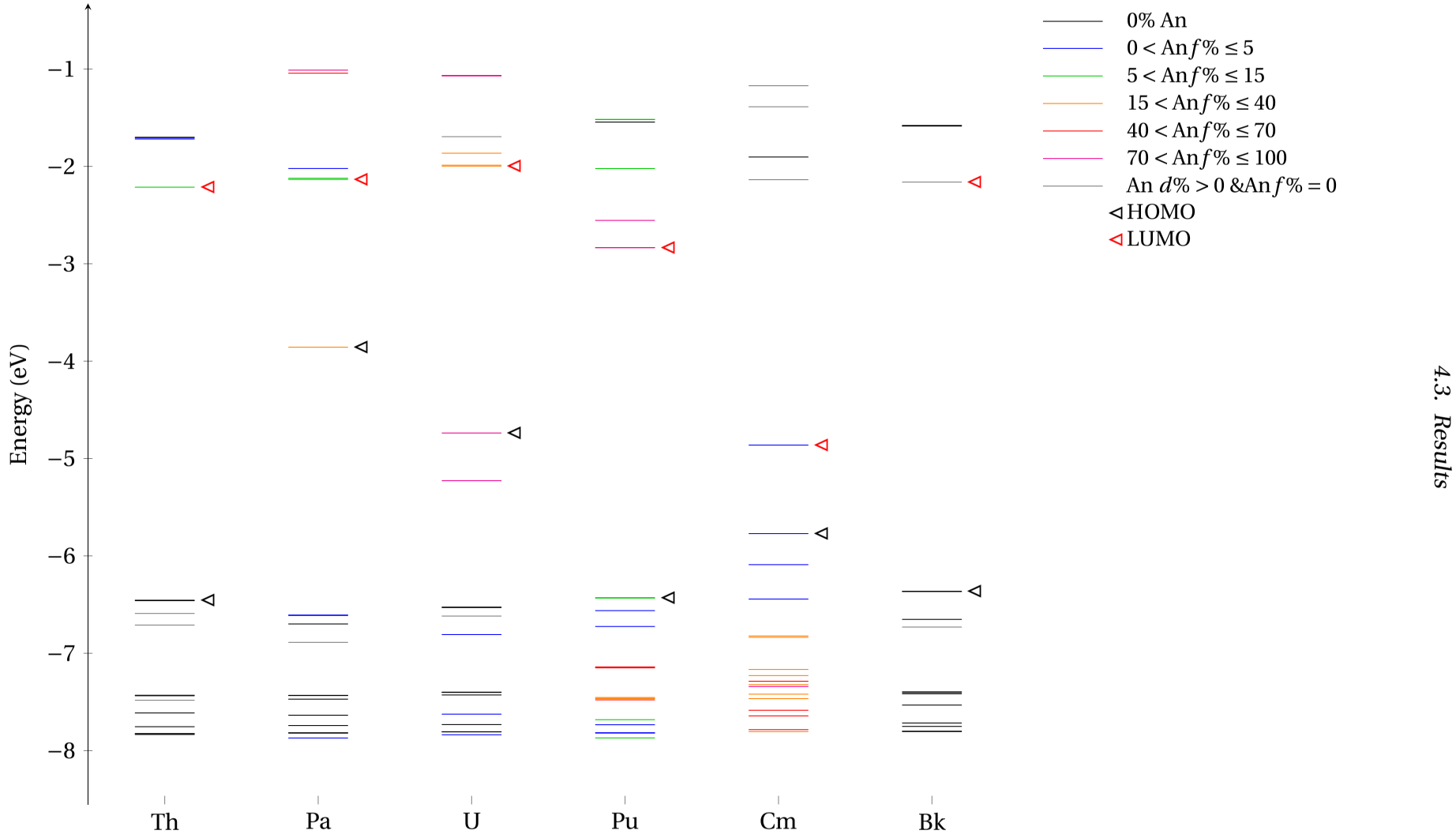

Figure 4.11: Valence α-spin orbitals between −8 and −1 eV for the An(^{Ph}beki)$_4$ complexes, calculated with PBE0, coloured to show the An f character in the orbital.

4.3.4 Spin Densities

Figure 4.12 shows the familiar actinide spin density trend from the tris-Cp systems and the actinide dioxides – the actinide spin density initially decreases, then increases to a maximum at curium, which gains almost a full electron of extra spin density from the ligand over its 6 expected unpaired electrons, and then suddenly decreases as the filling of 7 f orbitals' worth of electrons in the berkelium makes the movement of more α density from the ligand to the metal unfavourable.

In this richer chemical environment, however, the various effects that go into the movement of spin density may be partially deconvoluted, by inspecting the spin densities assigned to the ligand atoms. Figure 4.13 and 4.14 show these for the PBE- and PBE0-calculated systems respectively.

The alternating spin densities across the ligand ring section are indicative of the delocalisation of spin-orbitals in this region – the more localised the orbitals in the system, the less spin polarisation should induce spin polarisation on adjacent atoms. This is particularly noticeable in the difference in the plutonium and berkelium complexes moving from PBE to PBE0, as the more localised PBE0 orbitals reduce the capacity for spin delocalisation between the actinide and the ligand, lowering the spin density deviation on the actinide and the degree of spin polarisation on the ligand.

The relative magnitudes of the spin densities assigned to the nitrogen, oxygen and the carbon in the middle of the N-C-C-C-O loop (C_{back}) may be used to infer orbital properties with regards to delocalisation between the actinide and the nitrogen and oxygen, and the value of the spin density for C_{back} relative to these indicates the balance between localised and delocalised spin shifts. Thus, in the protactinium complex, a large spin polarisation is induced, as shown by the large spin densities on the carbons adjacent to the nitrogen and oxygen, but the spin densities of the nitrogen and oxygen atoms are increased by the delocalisation of the α orbitals of the protactinium onto these atoms through back-donation. For the PBE calculations, the systems for actinides between protactinium and curium appear to have balanced spin densities for nitrogen and oxygen, but an increased polarisation of spin between the actinide and ligand compared to the same system with PBE0.

The curium complex appears to have a large inequality between the oxygen

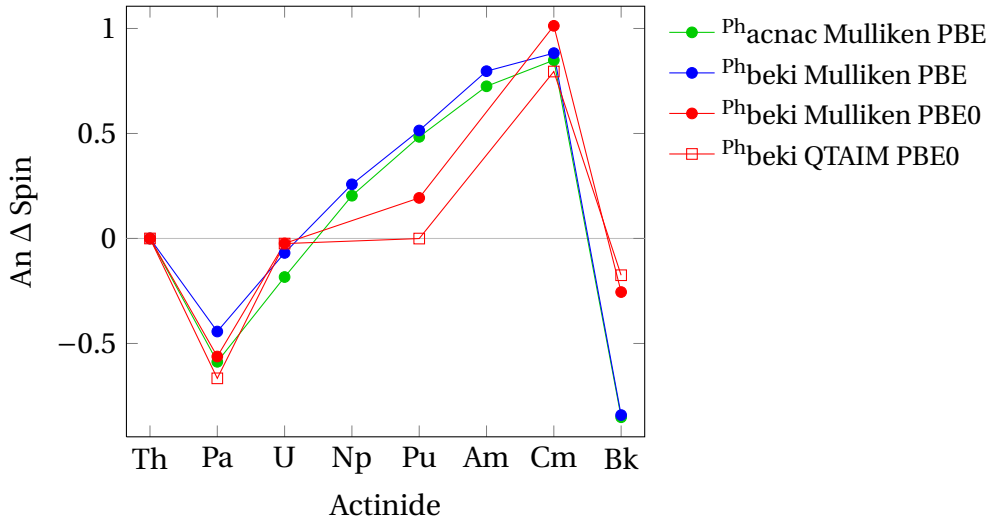

Figure 4.12: Deviation from formal integer spin on the actinide shown in the Mulliken spin density and the QTAIM spin density data, in the An(^{Ph}acnac)$_4$ and An(^{Ph}beki)$_4$ complexes.

and nitrogen, calculated with either functional, and a much larger spin density for the back carbon than for the oxygen, suggesting that the curium is strongly attracting spin density due to its large exchange energy gains per α electron, but that the curium is also delocalising part of that spin onto the oxygen. This fits the degeneracy-based orbital mixing pattern if the curium and oxygen atomic orbitals are significantly closer in energy than the curium and nitrogen atomic orbitals.

Overall, the competition between the spin delocalisation and spin polarisation results in a comparison of actinide spin density across the series of being a poor indicator of any single effect, although the magnitude over the entire series may be a good indicator of the relative capacity for spin delocalisation compared with another series – for example, this series of compounds and the tris-Cp compounds have much higher spin density shifts than those present in the actinide dioxide series[63, 82] (see figure 4.15). This would indicate that this entire series of compounds is more polarisable than the actinide dioxides, unsurprising given the aperiodic *vs* periodic environment, and would indicate a higher degree of orbital mixing to allow these relocations of spin density.

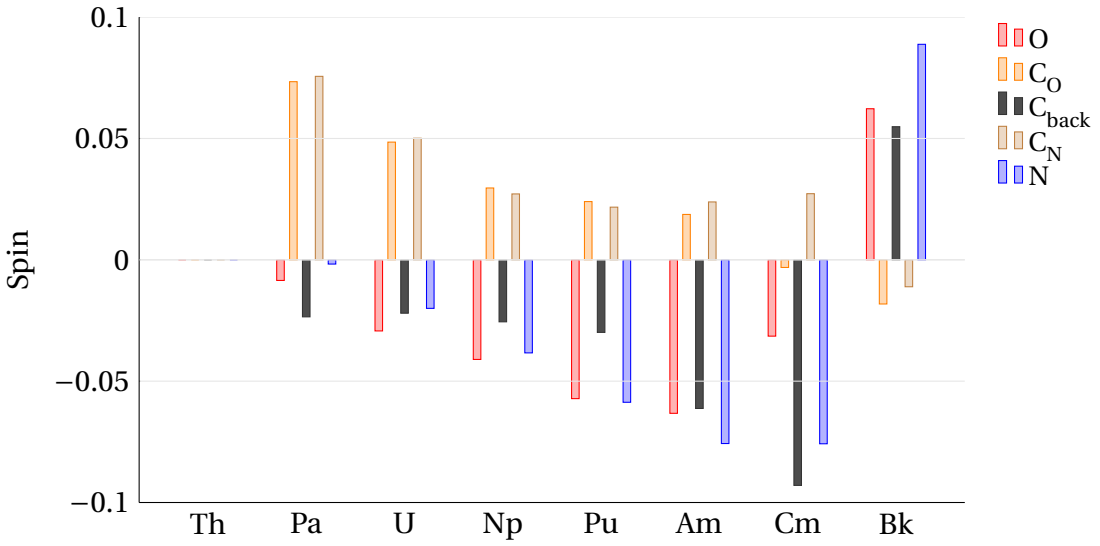

Figure 4.13: Mulliken spin for atoms on the central ligand loop, averaged over the four ligands, in the An(^{Ph}beki)$_4$ systems calculated with PBE.

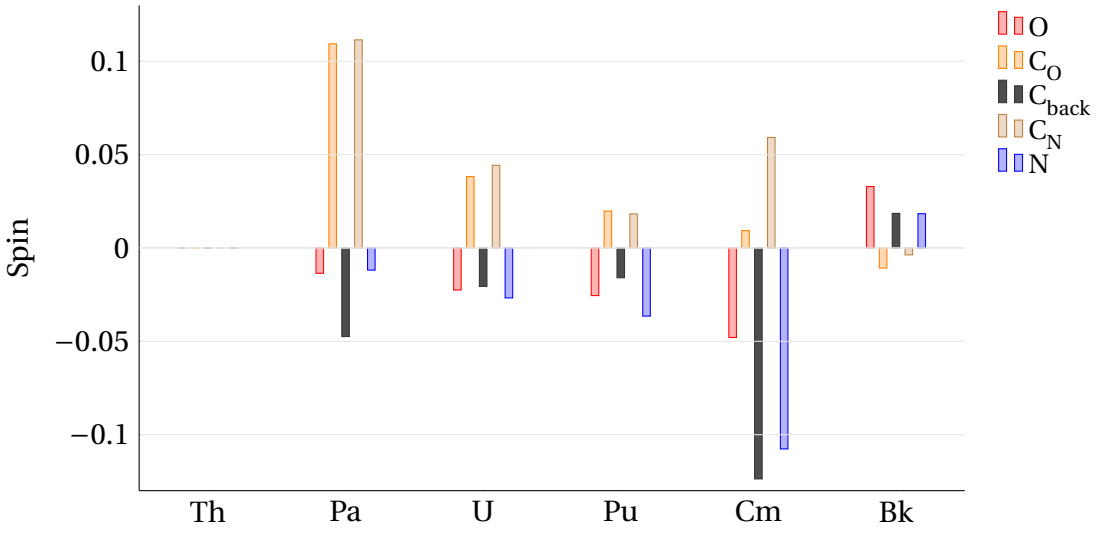

Figure 4.14: Mulliken spin for atoms on the central ligand loop, averaged over the four ligands, in the An(^{Ph}beki)$_4$ systems calculated with PBE0.

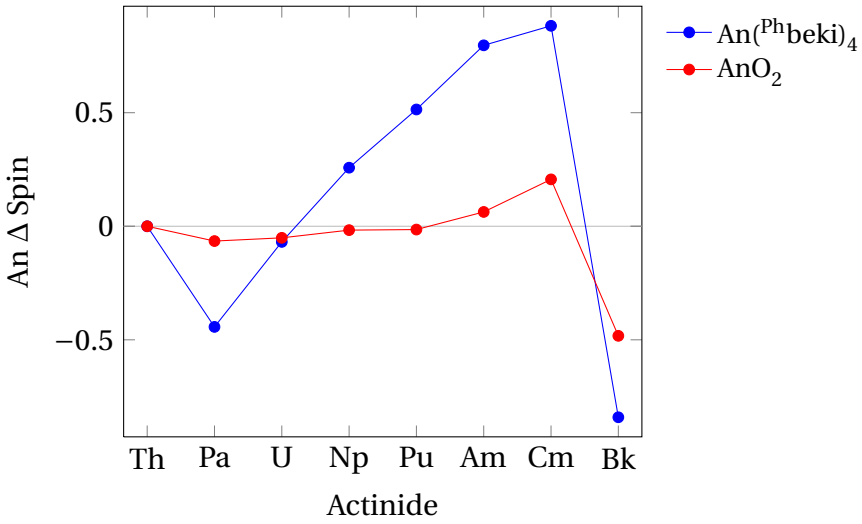

Figure 4.15: Deviation from formal integer spin on the actinide shown in the Mulliken spin density, in the An(^{Ph}beki)$_4$ complexes as compared with the actinide dioxide[82].

4.3.5 NPA

For comparison with the tris-Cp data, the NPA data for these compounds are presented in figures 4.16 (PBE) and 4.17 (PBE0). Only the scheme which includes both the $6d$ and $7p$ orbitals as valence orbitals has been used here. Some of the same trends as in the previous chapter are evident – the lack of change across the series in the actinide $7s$ and $7p$ population components (corresponding with a lack of participation of these orbitals in the valence region), and the mixture of d and f occupation in the protactinium complex, which once again arises from the similarity in energy of these two sets of orbitals in protactinium.

The natural charge is higher than in the tris-Cp complexes, though not by a whole electron due to the increased amount of ligand density to draw upon and higher chelation degree; more notable in the charges, however, is the difference in the actinide with the minimum charge in the series – in the tris-Cp systems, the minimum actinide natural charge occurred in the protactinium, however, here it appears to occur at uranium in the PBE data, and somewhere between uranium and americium in the PBE0 data (allowing for the two missing data). This is likely due to the protactinium having better back-donation due to being able to employ d orbitals, rather than any increase in ionicity.

The natural charges are also approximately 0.2 e higher in each species for the

PBE0 calculations as compared to PBE, showing more evidence of the higher delocalisation present in PBE orbitals.

The effect of a half-full f-orbital set on the ability to gain further electron density can be observed once more in the berkelium complex, where a sharp decrease in the $5f$ component of the actinide natural charge excess can be seen.

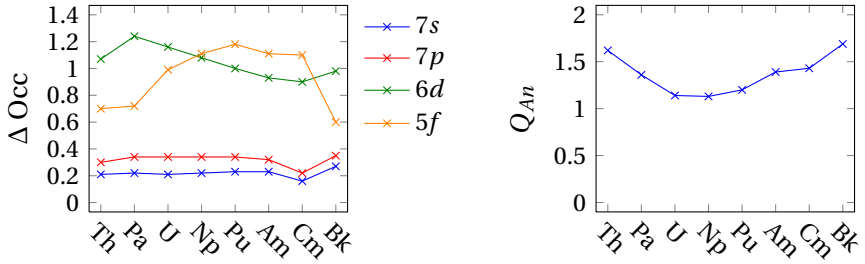

Figure 4.16: NPA actinide charges (Q_{An}) and deviations from formal occupations (Δ Occ) in the An(^{Ph}beki)$_4$ complexes, using the PBE functional. Note that this assumes all actinide (IV) ions are formally $6d^0$.

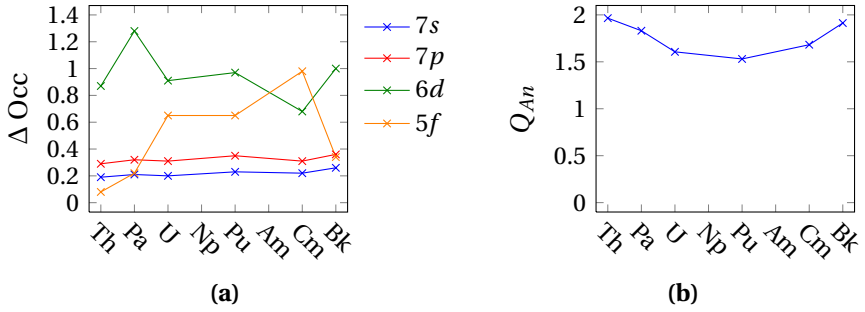

Figure 4.17: NPA actinide charges (Q_{An}) and deviations from formal occupations (Δ Occ) in the An(^{Ph}beki)$_4$ complexes, using the PBE0 functional. Note that this assumes all actinide (IV) ions are formally $6d^0$.

4.3.6 Topological Density Analysis and Integrated Basin Properties

Unlike in the tris-Cp complexes, here the actinide is completely encapsulated by the ligands, leaving no avenue for density to diffuse out into vacuum. This means that the actinide QTAIM atomic basin volume trend almost exactly follows the An−O length trends (see figure 4.18), and there should be no large difference in isodensity envelope volume as was seen for the thorium and protactinium tris-Cp complexes.

The An−N and An−O bond critical point density, Laplacian and total energy density data are shown in figure 4.21. Once again the curium complex appears to

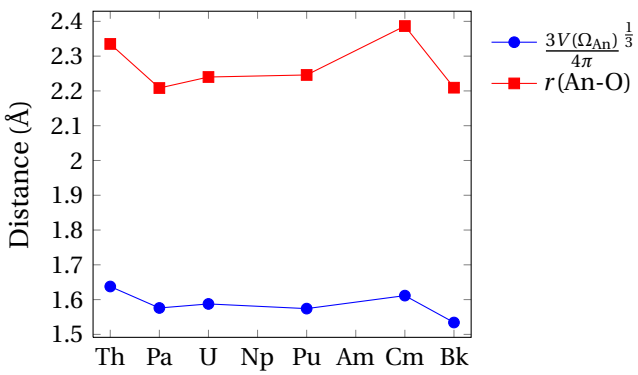

Figure 4.18: Radius for a spherized actinide basin and An-O bond length, using the geometry and density data calculated with the PBE0 functional.

come out as the most ionically bonded by these metrics, having the least density at the BCP, the lowest density curvature excepting thorium (which in the (IV) state is already expected to be largely ionic), and the least potential energy density excess in the total energy density. The protactinium complex, as in the tris-Cp systems, appears to have indicators of the highest degree of covalency of these complexes by comparison, with the highest density values at the BCP, and the most negative H values, with the effect apparently magnified in the PBE0 data by the increased localisation.

The QTAIM basin charges (figure 4.19a) show that, as with the americium complex in the tris-Cp set, the complex with the most mixed actinide-ligand orbitals, the curium complex, also has the lowest basin charge in the set. The delocalisation indices for these complexes, shown in figure 4.19b, still show that the curium complex has the least shared density, however, for both An−N and An−O indices. This suggests that, while curium's enhanced orbital mixing allows the movement of charge, the additional electrons present compared to the earlier actinides forces the population of more orbitals with anti-bonding character which leads to the lowering of many metrics connected with covalent character. The delocalisation indices also show a more covalent bond for An−O than An−N, which suggests that the oxygen in the ring may dominate the bonding simply due to electronegativity. A comparison study using similar ligands with two oxygen atoms and two nitrogens may be instructive in this regard.

As in the NPA charges, the abnormally high protactinium basin charge (higher than in the expected more ionic thorium complex) is likely due to an enhanced abil-

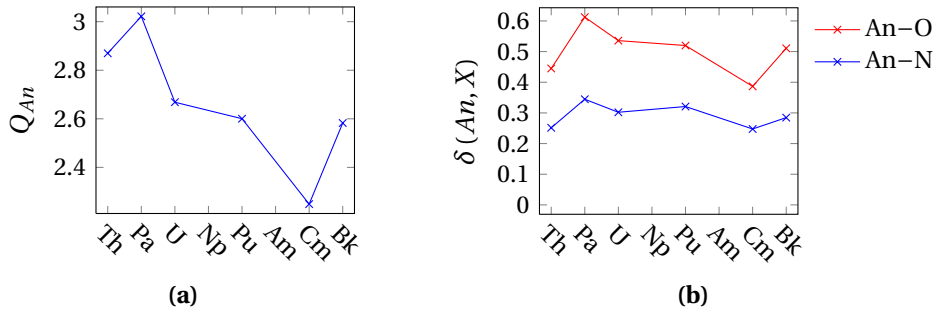

(a) **(b)**

Figure 4.19: Actinide charges (a) and delocalisation indices for the An−O and An−N basins (b) (averaged over the four ligands), with the PBE0 functional.

ity to engage in back-bonding using diffuse d orbitals.

Despite the increasing Z across the series, the increase in bonding metrics from curium to berkelium is not unexpected – aside from any degeneracy-based covalency arguments, berkelium gains significant β density in the valence f orbitals, which produces a shielding effect between the α f density and the nucleus, and thus produces more diffuse f orbitals, producing mid-period break behaviour.

4.3.6.1 Inter-Ligand Bonding

Unrelated to the actinide-ligand bond, the topological analysis also shows evidence of inter-ligand interactions, in the molecular graph – the linking of bond paths of maximum density from atoms to BCPs. The graph for the uranium ^{Ph}beki complex is shown in figure 4.20, showing bond-paths between the ligands in expected π-interaction locations, as well as a path between two sterically close hydrogen atoms, a phenomenon often seen in organic molecules[83].

Low-density pseudo-hydrogen-bond bond paths also appear between the oxygen and one of the phenyl hydrogen atoms in configurations that are not shown in figure 4.20, however these are exceptionally difficult to display usefully due to the perspective and atoms involved.

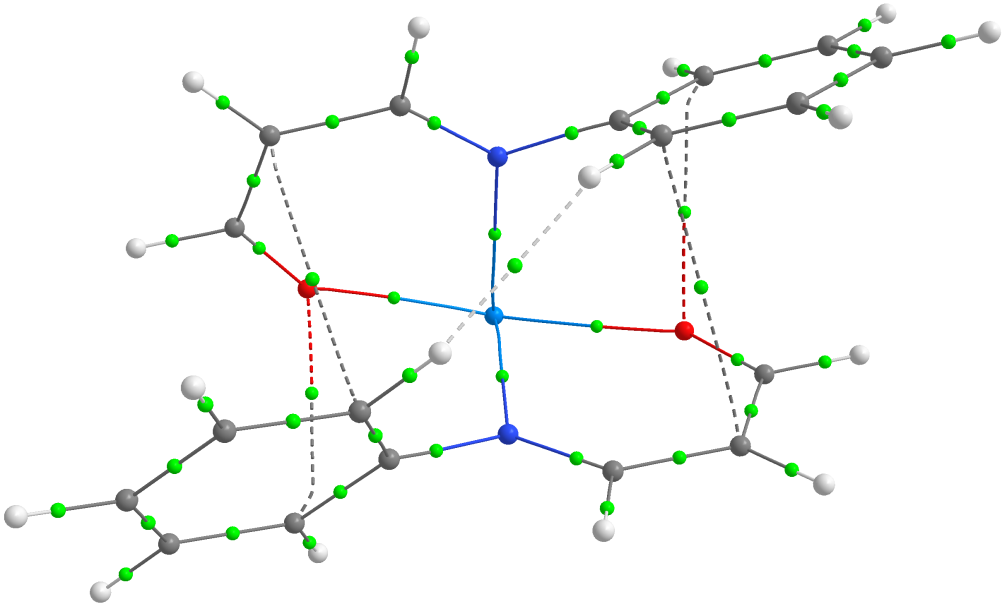

Figure 4.20: The molecular graph for U(^{Ph}beki)$_4$ calculated from the density obtained with the PBE0 functional, with two of the ligands omitted for clarity. The dashed lines indicate bond paths that lead to bond critical points with a density of less than 0.025 au, and, in this case, the inter-ligand bond paths.

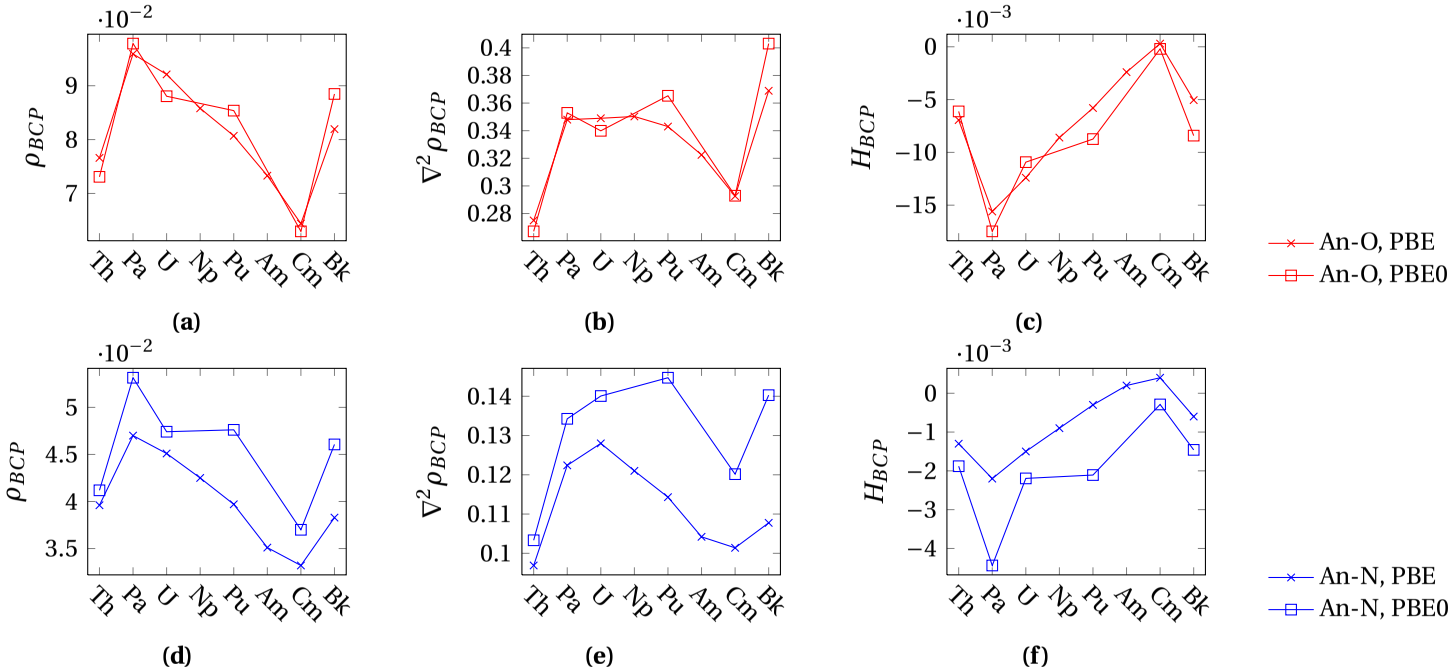

Figure 4.21: QTAIM data for An−O and An−N bond critical points for optimised An(^{Ph}beki)$_4$ structures. All scales are in atomic units.

4.3.6.2 Removing Structural Dependence

The quantities ρ, H and $\nabla^2\rho$ evaluated at bond critical points are strongly affected by the bond length within the same species [84]. To inspect the effect of removing this variable from the data, densities were obtained for the complex with each actinide, at a single geometry. The geometry used was that of the plutonium complex optimised with PBE. Bond critical points were then again found in the density, data for which are shown in figure 4.22.

These calculations exhibit a very small degree of spin contamination in the americium and plutonium complexes with the PBE functional, with the americium complex $\langle S^2 \rangle = 8.7577$ rather than 8.7500, and the plutonium $\langle S^2 \rangle = 6.0063$ rather than 6.0000. The next largest is the curium PBE calculation, with only 12.0016 instead of 12.0000. These spin contaminated elements, especially given that the largest component is annihilated automatically by Gaussian09, go further towards suggesting minor multiconfigurational character around the minima.

These data show that with the same geometry, a steady decrease is seen in BCP density consistent with actinide f orbital contraction with both functionals and in both An-O and An-N bonds. The shift from thorium to protactinium clearly adds more density to the bonding region in both the optimum and this fixed geometry, supporting the uncontroversial statement that thorium gives a more ionic bond than protactinium in this oxidation state, and the following actinides in the series are assumed to have more contracted orbitals.

The trends in the density Laplacian further suggests that protactinium has not only the highest density at the BCP, but also around it, with the lowest curvature. The An−N BCP Laplacian data also suggest a decrease in curvature related to general depletion of density in the bonding region, and a difference between the PBE and PBE0 data in the early actinides is again likely related to the the difference between PBE and PBE0 orbital behaviour. The An−N and An−O H data also suggest that the effect of the d orbitals is key in determining the energy density in these systems, as the largest variations are seen in the series from thorium to neptunium. Although similar trends are shown, the H data for the An−O BCPs are uniformly larger in magnitude, due to the shorter bond.

Overall, these data show how it is important to not ignore the correlation of

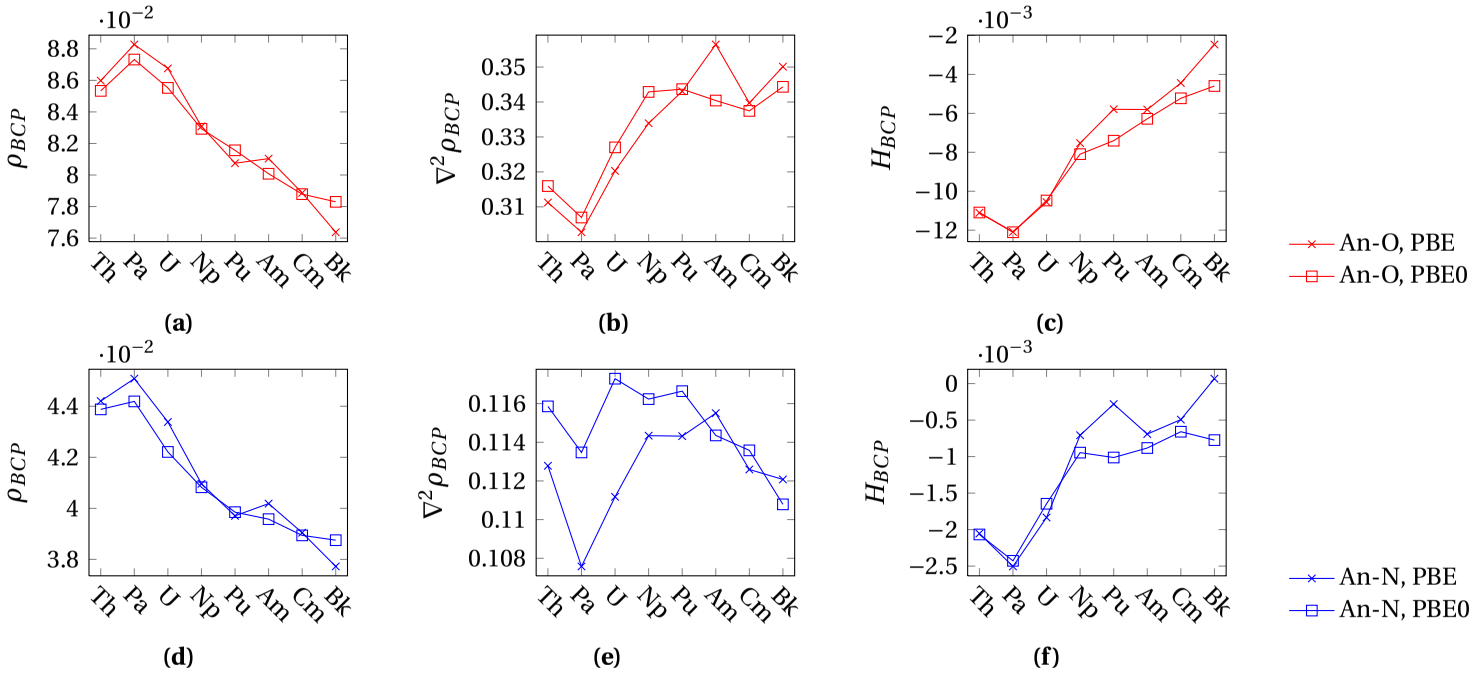

Figure 4.22: QTAIM data for An−O and An−N bond critical points in An(^{Ph}beki)$_4$ each at the optimised PBE Pu(^{Ph}beki)$_4$ geometry. All scales are in atomic units.

BCP data with bond length, and include these in deduction, as unsurprisingly the largest single changes in optimal bond length, e.g. from thorium to protactinium and curium to berkelium, result in large changes in data which are not reproduced if bond lengths are equal.

They also show how despite the actinide contraction reducing the size of the f orbitals, the berkelium appears to obtain a similar contraction in bond length and increase in bonding density and increasing negative magnitude in the total energy density, suggesting increasing covalent character.

4.4 Conclusions

These compounds exhibit many similar behaviours to the tris-Cp complexes, and it seems clear that more degeneracy-based orbital interaction is at work. The NPA data again shows that the d and f orbitals are not simply divided, and that this type of bonding is not compatible with integer occupations portioned neatly.

The valence orbital decomposition shows that, as in the tris-Cp compounds, the actinide f-orbitals fall in energy, mixing most strongly with the highest energy occupied ligand orbitals where they are closest in energy in the curium ^{Ph}beki compound.

QTAIM once again shows us a result that is a little clearer in terms of what to expect from the bonds, giving bond orders and densities consistent with largely ionic bonding with a small covalent component. The delocalisation indices show a lower bond index than with the Cp rings, and the An−O having a bond closer to a covalent bond than the An−N, indicating that the longer An−N bond is likely also weaker.

They also indicate that despite the curium complex's highly mixed orbitals, once again the most mixed compound has the lowest bond indices. This may be due to the higher number of more antibonding and nonbonding orbitals created.

The comparison at fixed geometry demonstrates that while data obtained from QTAIM are obviously dependent on the geometry, they are not determined by it, and effects can be seen and compared regardless of differences in geometry.

This technique would no doubt benefit from a full and in-depth theoretical analysis on a simple system, to fully decompose the molecular orbitals and relate them to the QTAIM behaviour. However, such an additional study was beyond the

scope of this project. Already, however, we see that QTAIM can give results that are not confused by variable occupations like the NPA data, or made much more confusing by competing effects like spin densities.

Again, being able to accurately assess likely bond strengths in solution would be extremely useful in being able to make useful comparison with the experimental equivalents of these data trends, but these are large ligands with strongly charged regions, which make accurate solution modelling extremely challenging.

In the following chapter, an attempt is made to investigate the methods required and gauge how tractable these problems are.

4.5 Publishing Notes

Work included here was published in: David D. Schnaars, Andrew J. Gaunt, Trevor W. Hayton, Matthew B. Jones, Ian Kirker, Nikolas Kaltsoyannis, Iain May, Sean D. Reilly, Brian L. Scott, and Guang Wu. Bonding trends traversing the tetravalent actinide series: Synthesis, structural, and computational analysis of An(IV)(^{Ar}acnac)$_4$ complexes (An = Th, U, Np, Pu; ^{Ar}acnac = ArNC(Ph)CHC(Ph)O; Ar = 3_5−tBu$_2$−C$_6$H$_3$). *Inorganic Chemistry*, 51(15):8557–8566, July 2012.

Chapter 5

Plutonium (IV) Hydration and Hydrolysis

Over the lifetime of nuclear fuel, it typically spends a significant quantity of time exposed to water, which can both leach out soluble ions, and react with the surface. One especially complex case may be found in temporary storage ponds at the Sellafield nuclear fuel storage and processing site, where there exists a large quantity of fuel and cladding waste based on the Magnox design which has decomposed to form liquid and sludge phases. Understanding the solvated behaviour of possible components of such mixtures is vital to their safe management and, hopefully, their eventual conversion into useful products and more economically and safely stored waste.

Unfortunately, solvation is extremely difficult to model accurately, especially in polar solvents such as water. Models such as CPCM and COSMO, which attempt to reproduce solvent effects on a system by embedding it in a surface of charged points or discs, fail to correctly reproduce more complex solvent effects caused by bonding to the solvent[85, 86], and attempts to reproduce these by including small numbers of solvent molecules ("microsolvation") do not correctly reproduce statistical effects inherent in the motion of the molecules. This is especially true when the correct behaviour is to *react* the solvent with the system in question.

The correct determination of speciation and prediction of reactions in solvent requires accurate free energies, which are typically more affected by the addition of the solvent than response properties, especially in charged systems. To correctly model solvent, then, it is necessary to model a large quantity of solvent molecules.

However, correctly modelling large systems quantum mechanically can become extremely expensive computationally. Therefore, periodic systems may be used, to model an infinite quantity of solvent and solute. This has the disadvantage of allowing possible interactions between adjacent cells, but ensures a reasonable depiction of a scale of solvent orders of magnitude larger than the solute system. The statistical effects of a static system need to be eliminated as well, however, so approximations based on averages over a time-dependent model are required. Molecular dynamics provides an approach that can correctly model the motions of atoms in dynamic molecules and thus model a real solvent system to the degree of accuracy required.

This type of system still requires significant computational resource for large solute systems, which is why parametrised force-field based approaches are often used. For actinide solvation in particular, it is only recently that the use of fully quantum mechanical approaches has become widely feasible in this type of scheme – previous work has focused on the construction of hybrid approaches[87], the construction of force fields based on smaller quantum mechanical calculations[88, 89], or the use of previously empirically determined force field parameters [11]. Only recently have fully quantum mechanical molecular dynamics studies of heavy metal hydrates emerged, on uranium (IV) [90] and polonium (IV)[91].

In the present work, both static and dynamic models have been used to investigate the solvation of plutonium (IV) in a model system, which, while limited, should provide a good approximation to experimental conditions in very dilute aqueous solution, which have been previously structurally characterised with Extended X-Ray Absorption Fine Structure measurements (EXAFS, see section 1.3, p23)[92], as well as thermodynamically[93]. Many aspects of this study were informed by a set of studies performed on polonium (IV) hydrate and hydroxide complexes by Ayala et al. [94, 95, 91], as well as studies on strontium (II) hydrates and hydroxides [96, 97].

A significant part of plutonium chemistry that has been neglected in this study is that plutonium (IV) is known to be able to form a colloidal gel through polymerisation at a pH of above approximately 1[2], with a rate dependent on concentration. This is not included due to complexity, and a full exploration of this process using these methods would be a additional significant work in itself. Experimental studies of plutonium (IV) typically use low concentrations, acidic conditions with $HClO_4$,

and filtration of particulates to avoid this [93].

5.1 Molecular Complexes

Initially examining the molecular complexes in isolation allows the prediction of probable candidates for the optimal complex in solution, even if the combination of charged species and continuum solvation methods mean that thermodynamic energies are not expected to be entirely accurate. It also allows the identification of effects which may produce unexpected biases in preferred structure, such as the trans effects shown in the polonium hydroxide complexes [95].

5.1.1 Computational Details

To obtain optimal geometries for the molecular complexes, approximate geometries were created in Avogadro, and the coordinates optimised using version 6.2 of the Turbomole program. The TPSS functional[98] was used, with the resolution-of-the-identity approximation in parallel [99], and with the def2-TZVP basis set[100] on oxygen and hydrogen atoms, and the Stuttgart-Bonn RECP on plutonium atoms [69, 27]. The 'm4' spatial integration grid was used for increased accuracy over the standard 'm3' grid. Stricter SCF and geometry convergence criteria than normal were applied to ensure accurate energies and to obtain better accuracy for the hydrogen positions, for which the potential well may be of low curvature in a sterically unhindered system.The SCF convergence criterion was set to require energy convergence of $< 10^{-9}$ hartree, while the change in energy between geometry steps was required to be $< 10^{-8}$ hartree, and the Cartesian gradient norm was required to be $< 10^{-4}$ au.

Vibrational frequency calculations were performed analytically on converged geometries to ensure all structures were true minima and to obtain temperature-dependent contributions to free energies, and single-point calculations were performed including energetic corrections from COSMO, to approximate the effects of solvation. No scaling was applied to obtained vibrational frequencies used for thermal vibrational energy contributions to the Gibbs free energy and entropy. Scaling factors for TPSS frequencies found to minimise the RMS of the error in the vibrational contribution to the free energy for test sets of molecules are available for many

Pople-style basis sets of similar quality to the basis sets used here, and at 298.15K these scaling factors are all 1.0 to two significant figures [101], suggesting that not scaling should give reasonable results. Turbomole's default radii were used for cavity construction – van der Waals atomic radii scaled up by 1.17.

In several cases, two isomers were found for a particular number of hydroxide and water ligands, and these are shown. When considering these energetically, the approximation devised by Guthrie[102] and also used in a similar study on strontium hydration[97] was applied – if the Gibbs free energy terms of the isomers were found to be within 10 kJ mol^{-1}, an entropic stability contribution of $-RT\ln N \approx 1.72$kJ mol^{-1} for $N = 2$, where N is the number of isomers in this range, was added to the more stable, and that free energy used.

Unfortunately wavefunction output files produced by Turbomole proved incompatible with AIMAll, so the optimised geometries were used in single-point calculations in Gaussian09.a02 and the resultant output files used instead. For this, the SARC basis set[80] was used for the plutonium atom, and the 6-311G** basis for the oxygen and hydrogen atoms. Relativistic effects were included with the scalar Douglas-Kroll-Hess Hamiltonian, and ultrafine grids were applied to ensure accuracy in the core region of the plutonium nucleus. Point nuclei were used with the SARC basis set, as recommended, rather than the default Gaussian nuclei. Output wavefunction files from these calculations were then used with AIMAll to perform QTAIM analysis.

Basis set superposition error was considered somewhat late in the proceedings, and proved to be extremely time-consuming in set-up and configuration to calculate with Turbomole for open-shell systems. Initial tests increasing the hydrate shell for related thorium hydrate complexes suggested that BSSE corrections for this reaction would be a positive shift to the reaction energy of adding a water molecule, of the order of less than 10 $kJmol^{-1}$ and decreasing in magnitude with increasing coordination number. Because these were not analysed for the plutonium complexes for inclusion across all reactions, they are not included in the data quoted.

5.1.2 Hydrates

Hydrates were studied initially, obtaining plausible optimised structures with complexes containing 4-10 waters in the primary solvation shell. Attempts to optimise geometries with 11 and 12 water molecules in the primary shell led to the ejection of water into a secondary shell, while attempts to optimise complexes with fewer water molecules led to SCF convergence problems, and in any case could not be representative of a solvated system.

To ascertain which would be the most stable hydrate complex in solution, the Gibbs free energies for reaction 5.1 were calculated, applying COSMO corrections to gas phase free energies using the approximation shown in eq. 5.2, and are shown in table 5.1. Unsurprisingly, this shows that the dissipation of charge created by adding more waters to a gas phase cluster is favourable for all the hydrate geometries, but, more usefully, it also shows that in COSMO, the optimal complex is correctly identified as eight-coordinate. Structural parameters for water-ligated plutonium, experimentally obtained using EXAFS, give a nearest neighbour distance of 2.39Å in a 'spherical' 8-coordinate complex, obtained in 1M $HClO_4$ [23, 2], while the computationally obtained geometry has a mean bond length of 2.41Å . Full optimisation of the 8-coordinate geometry within a COSMO framework led to a very similar structure with shorter bonds, at a mean bond length of 2.34Å, showing that the geometries obtained with each are somewhat similar, but that the gas-phase optimised geometries may be closer to reality.

$$[\mathrm{Pu(OH_2)}_n]^{4+} + \mathrm{H_2O} \longrightarrow [\mathrm{Pu(OH_2)}_{n+1}]^{4+} \tag{5.1}$$

$$\tilde{G} = G^{\ominus}_{\mathrm{gas}} + \Delta G_{\mathrm{COSMO}}$$

$$\Delta G^{\ominus}_r = \tilde{G}\left([\mathrm{Pu(OH_2)_{n+1}}]^{4+}\right) - \left(\tilde{G}\left([\mathrm{Pu(OH_2)_n}]^{4+}\right) + \tilde{G}\left(\mathrm{H_2O}\right)\right) \tag{5.2}$$

Mean, maximum and minimum Pu−O bond lengths for each of the complexes are shown in figure 5.1. The bond lengths exhibit a gradual lengthening with increased coordination number, and the low-symmetry higher coordination complexes have larger ranges. The 6-coordinate species has a particularly short bond

	$\Delta G_r^{\ominus}$ (kJ mol^{-1})	
No. Waters	In Vacuum	In COSMO
4		
↓	-283.07	-59.95
5		
↓	-263.78	-51.03
6		
↓	-152.85	-12.41
7		
↓	-143.19	-38.72
8		
↓	-99.42	13.28
9		
↓	-53.37	33.33
10		

Table 5.1: Calculated free energies of reaction for the hydrate shell expansion reaction 5.1, at 298K and 1 atm.

and low range because it is highly symmetric, as shown in figure 5.2, and the hydrogen atoms on the water molecules can perfectly 'slot' into place with minimal hindrance. This structure is unlikely to remain in such an interdependent geometry in solution, and thus the reaction energies involving this species may exaggerate its stability.

The 8-coordinate complex can similarly be arranged to symmetrically minimise steric contact, though in this case actually re-optimising with enforced S_8 geometrical symmetry increased the energy of the complex by 4 kJmol^{-1}, while increasing the Pu−O bond length to 2.41Å. While this is very close to the experimental figure, it should still be borne in mind that the optimisation is performed in gas phase, and thus the complex charge distributions should significantly differ between experiment and this calculation, suggesting this level of agreement is probably coincidental.

An additional isomer of the 8-coordinate complex was found, with hydrogen bonds seemingly holding the complex in a geometry half-way between prismatic and antiprismatic (labelled "nonprismatic" in figure 5.2). This has a free energy 9.74 kJ mol^{-1} higher than the antiprismatic form, and thus is included in the entropic contribution corrections.

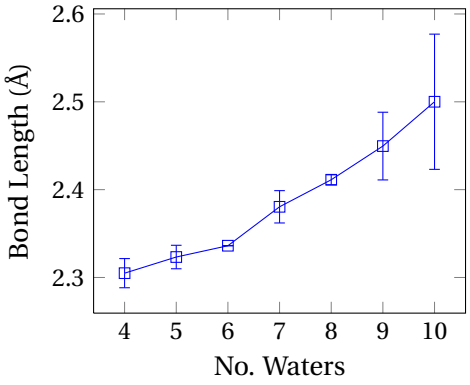

Figure 5.1: Mean optimised Pu−O bond lengths for the plutonium hydrates, $[Pu(OH_2)_n]^{4+}$. Bars indicate the maximum and minimum length.

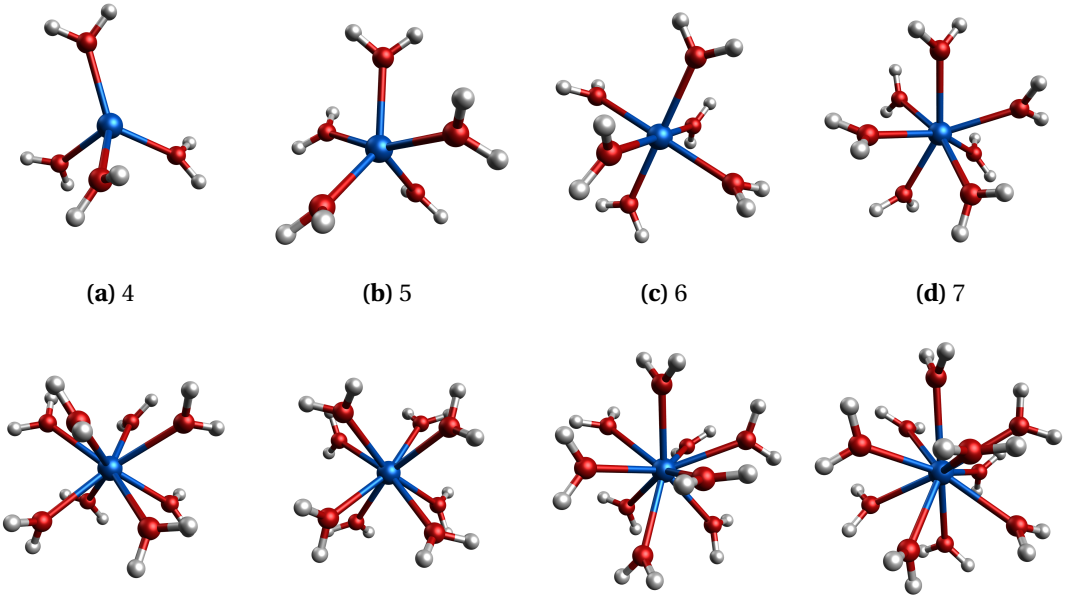

(a) 4 **(b)** 5 **(c)** 6 **(d)** 7

(e) 8 (antiprismatic) **(f)** 8 (nonprismatic)* **(g)** 9 **(h)** 10

Figure 5.2: The optimised geometries of the hydrate complexes, $[Pu(OH_2)_n]^{4+}$, labelled by coordination number. Isomers that are not lowest in energy are marked with an asterisk.

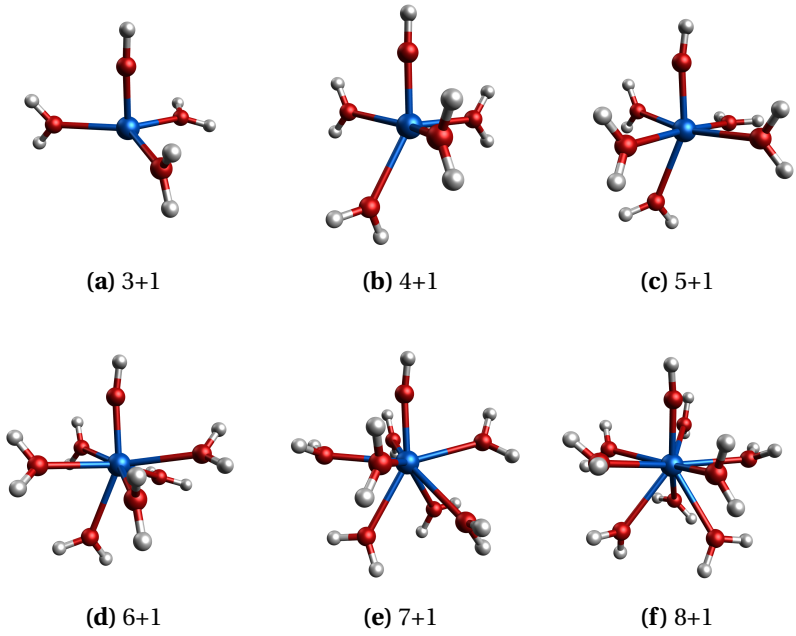

(a) 3+1 **(b)** 4+1 **(c)** 5+1

(d) 6+1 **(e)** 7+1 **(f)** 8+1

Figure 5.3: The optimised geometries of the monohydroxide complexes, $[Pu(OH_2)_n(OH)]^{3+}$, labelled as (n+1).

5.1.3 Hydroxides

The optimised geometries for the hydroxide complexes are shown in figures 5.3,5.4, 5.5, and 5.6, labelled using the notation *n*+*m*, where *n* is the number of coordinating water molecules, and *m* is the number of coordinating hydroxides. Thus, a species $[Pu(OH_2)_3(OH)_2]^{2+}$ would be labelled 3+2 under this scheme. Additional labels have been appended to differentiate isomers, T and C in the systems with two hydroxides, for *trans* and *cis*, and F and M in the systems with three hydroxides, for pseudo-*fac* and pseudo-*mer* – these being not quite as well defined outside an octahedral complex, but approximately used as M being a case where the hydroxides and central plutonium atom all lie approximately on a plane (a *meridial* plane), and F being used where hydroxides are clustered together.

As with the hydrates, attempts to obtain geometries for complexes with coordination numbers larger than those shown led to the ejection of water into a secondary shell – unfortunately, this includes the 5+3 species. Where more than one isomer was found, only those in the energy range considered for the entropic correction, within 10 kJ mol^{-1} of the lowest in energy, are shown. This energetic limit resulted in there being no permutation of water and hydroxide ligands with more than two consid-

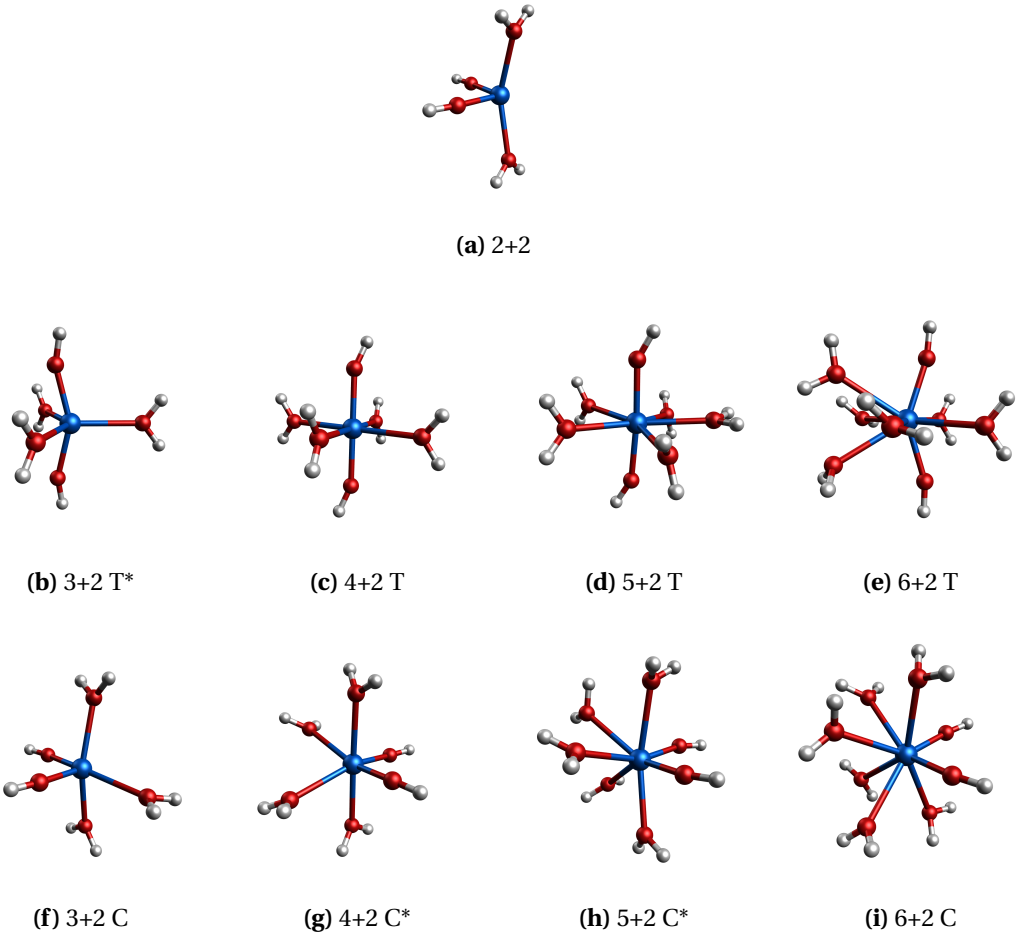

(a) 2+2

(b) 3+2 T* **(c)** 4+2 T **(d)** 5+2 T **(e)** 6+2 T

(f) 3+2 C **(g)** 4+2 C* **(h)** 5+2 C* **(i)** 6+2 C

Figure 5.4: The optimised geometries of the bishydroxide complexes, $[Pu(OH_2)_n(OH)_2]^{2+}$, labelled as (n+2 [C|T]), where C indicates approximately *cis*-hydroxides and T *trans*- where applicable. Isomers that are not lowest in energy are marked with an asterisk.

ered isomers.

In all but one case where a low-lying isomer was found, the complex with the greater angular spread of hydroxides was found to be lower in energy. The 3+2T complex is the exception, although it is unclear as to why – it may be that stability is gained by having an empty space *trans* to one of the hydroxides. As was found in the polonium (IV) mixed water/hydroxide complexes, the geometries show a marked effect on the positioning of water molecules *trans* to hydroxide, and a few common motifs that result from this and similar effects. The extension and angular offset of the Pu−O bond to water *trans* to a hydroxide appears throughout the structures, as well as effects on hydroxides *trans* to each other.

In an attempt to determine the effect the central ion has on this *trans* de-

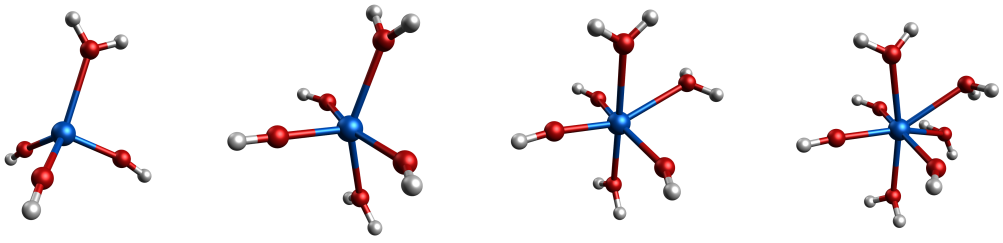

(a) 1+3 **(b)** 2+3 M **(c)** 3+3 M* **(d)** 4+3 M

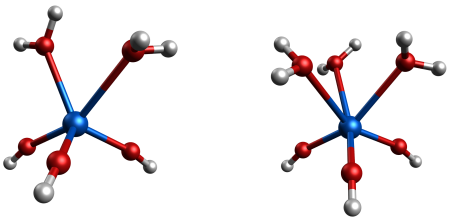

(e) 2+3 F* **(f)** 3+3 F

Figure 5.5: The optimised geometries of the trishydroxide complexes, $[Pu(OH_2)_n(OH)_3]^+$, labelled as (n+3 [F|M]), where F indicates clustered hydroxides and M pseudo-planar hydroxides where applicable. Isomers that are not lowest in energy are marked with an asterisk.

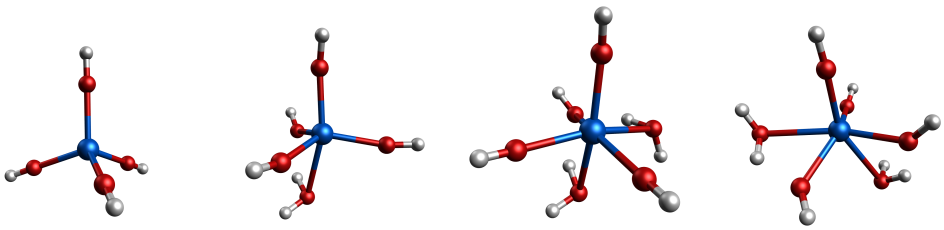

(a) 0+4 **(b)** 1+4 **(c)** 2+4 (waters close) **(d)** 2+4 (waters distant)*

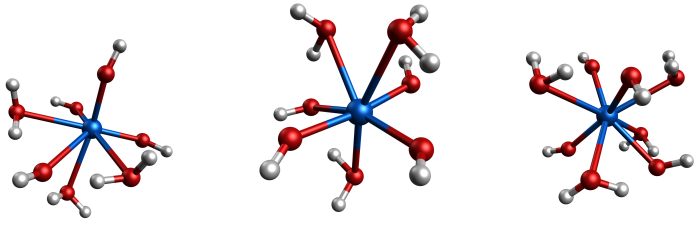

(e) 3+4 (aplanar hydrox.)* **(f)** 3+4 (~*mer.* hydrox.) **(g)** 4+4

Figure 5.6: The optimised geometries of the tetrakishydroxide complexes, $Pu(OH_2)_n(OH)_4$, labelled as (n+4). Isomers that are not lowest in energy are marked with an asterisk.

alignment, the geometry of the 5+1 plutonium complex was reoptimised for several other tetravalent central ions - polonium, reproducing the geometry from the study by Ayala *et al.*, cerium, commonly used as an ionic proxy for plutonium (IV)[103], thorium, an actinide expected to be largely ionic, and uranium, an actinide expected to have more effects from covalency than either plutonium or thorium. Equivalent quality basis sets to those used for plutonium were employed: the def-TZVP basis sets and RECPs for thorium, uranium, and cerium, and def2-TZVP for polonium.

The angle between the *trans* metal-hydroxide and metal-water bonds, as well as the two bond lengths, are shown in table 5.2. The effect acting to reduce the bond angle appears to be strongest in polonium, and weaker in uranium and thorium, which have more diffuse orbitals than cerium and plutonium. Assuming the conclusion from the polonium study is correct – that the effect is largely electrostatic and due to the hydroxide OH dipole, this may imply that a more diffuse central atom dampens the electrostatic effect. A single-point gas-phase calculation was performed in which the uranium centre in the optimised structure of the uranium (IV) 5+1 analogue was replaced with plutonium, and this proved to have an SCF energy only 18 kJ mol^{-1} higher than the optimised plutonium 5+1 structure, showing that the effect of the displacement on that energy is fairly weak, in any case.

A similar geometric distortion effect can be observed in complexes with two hydroxides *trans* – in all examples, the $H-O_h-Pu-O_h-H$ set is nonlinear. Two cases retain the straight O_h-Pu-O_h line but have rotationally symmetric bends on the $Pu-O_h-H$ (4+2, 5+2), while other cases have a nonlinear O_h-Pu-O_h as well as a $H-O_h-Pu$ bend, symmetric about a plane through the plutonium (3+2T, 6+2T, 3+3M, 4+3M, 1+4, 2+4).

Metal	$\angle O_wMO_h$	$r(M-O_h)$ (Å)	$r(M-O_w)$ (Å)
Po	140.6	1.982	2.579
Pu	156.4	1.971	2.429
Ce	164.3	1.969	2.469
U	179.9	1.966	2.449
Th	179.6	2.013	2.542

Table 5.2: Comparison of selected bond lengths and angles (Å, °) in the optimised structures of $[M(OH_2)_5(OH)]^{3+}$, M ∈ {Po, Pu, Ce, U, Th}.

Stepwise energy changes for adding water to a complex, modelled by reaction

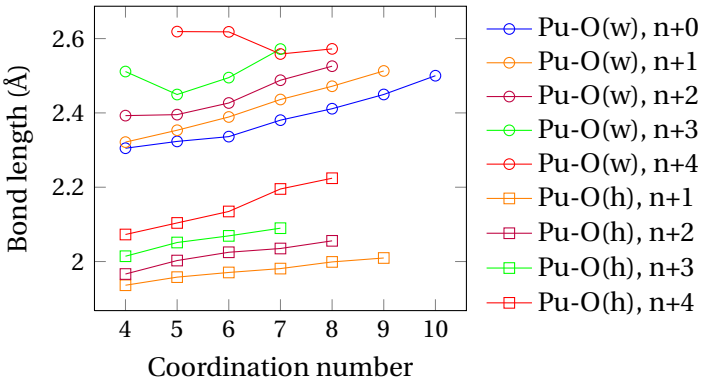

Figure 5.7: Average Pu-O(water) and Pu-O(hydroxide) bond lengths per complex in optimal mixed hydrate/hydroxide complexes.

5.3, and hydrolysis, modelled by reaction 5.4, are shown in tables 5.4 and 5.5 respectively. Following the favourable reaction pathways, the most stable species according to this method appears to be the 6+1 species, $[Pu(OH_2)_6(OH)]^{3+}$. As observed in the polonium (IV) study, and the thorium (IV) study of Tsushima *et al.*, the optimal size of complex at each level of hydrolysis decreases with increasing numbers of hydroxides, at a 1:1 ratio. Each step appears to have a sufficiently large energy change to not expect an equilibrium between significant components of two different complexes.

$$[Pu(OH_2)_n(OH)_m]^{4-m} + H_2O \longrightarrow [Pu(OH_2)_{n+1}(OH)_m]^{4-m} \tag{5.3}$$

$$[Pu(OH_2)_n(OH)_m]^{4-m} + H_2O \longrightarrow [Pu(OH_2)_{n-1}(OH)_{m+1}]^{3-m} + H_3O^+ \tag{5.4}$$

$$\Delta G_r^{\ominus} = \tilde{G}\left([Pu(OH_2)_{n+1}(OH)_m]^{4-m}\right) - \left(\tilde{G}\left([Pu(OH_2)_n(OH)_m]^{4-m}\right) + \tilde{G}\left(H_2O\right)\right) \tag{5.5}$$

$$\Delta G_r^{\ominus} = \left(\tilde{G}\left([Pu(OH_2)_{n-1}(OH)_{m+1}]^{3-m}\right) + \tilde{G}\left(H_3O^+\right)\right) - \left(\tilde{G}\left([Pu(OH_2)_n(OH)_m]^{4-m}\right) + \tilde{G}\left(H_2O\right)\right) \tag{5.6}$$

Using eq. 5.7, it is possible to calculate the pK_a arising from a given reaction energy. Assuming the favoured species are as calculated, summing over a hydrolysis and the subsequent dehydration step should give the overall ΔG of hydrolysis, which can then be converted into a pK_a to compare with experimental values, assuming that this model system represents effectively infinite dilution. The experimental values (from [93]) are presented as $\log K_n^{\circ}$ defined in eq. 5.8, and compared in table 5.3. The results obtained computationally clearly deviate widely from the

	pK_a		
Pathway	Computational	Experimental [93]	Po^{4+} Analogue[91]
8+0 ⟶ 6+1	-10.37	-0.60	-8.3
6+1 ⟶ 4+2	-1.67	-0.03	-1.1
4+2 ⟶ 2+3	8.28	2.88	6.1
2+3 ⟶ 0+4	11.27	6.29	19.6

Table 5.3: Experimental vs calculated hydrolysis pK_a values.

experimental values, but show appropriate trends, and show strong similarities to the data obtained for the polonium ion. This deviation is not unsurprising given the approximations used, unfortunately, especially with the problems of charge in continuum solvent models mentioned previously, and this has been highlighted in other works[85, 86].

$$\mathrm{p}K_a = \frac{\Delta G_r}{RT\ln(10)} \tag{5.7}$$

$$K_n^\circ = \frac{\left[\mathrm{Pu(OH)_n^{4-n}}\right]\left[\mathrm{H^+}\right]}{\left[\mathrm{An^{4+}}\right]} \tag{5.8}$$

	n_{OH}=0	1	2	3	4
CN=4	4+0	3+1	2+2	1+3	0+4
	↓ −59.96	↓ −32.19	↓ −12.77	↓ −1.83	↓ 31.05
5	5+0	4+1	3+2	2+3	1+4
	↓ −51.03	↓ −16.85	↓ −9.82	↓ 7.64	↓ 20.89
6	6+0	5+1	4+2	3+3	2+4
	↓ −12.41	↓ −5.97	↓ 18.73	↓ 35.12	↓ 40.72
7	7+0	6+1	5+2	4+3	3+4
	↓ −38.72	↓ 7.63	↓ 14.61		↓ 41.24
8	8+0	7+1	6+2		4+4
	↓ 13.28	↓ 20.51			
9	9+0	8+1			
	↓ 33.33				
10	10+0				

Table 5.4: Calculated Gibbs free energy changes associated with adding a water ligand to plutonium mixed hydrate/hydroxide complexes in COSMO-simulated solution (reaction 5.5), in kJ mol^{-1}.

	n_{OH}=0		1		2		3		4
CN=4	4+0	$\longrightarrow$ −163.30	3+1	$\longrightarrow$ −45.40	2+2	$\longrightarrow$ 25.74	1+3	$\longrightarrow$ 65.97	0+4
5	5+0	$\longrightarrow$ −135.12	4+1	$\longrightarrow$ −20.90	3+2	$\longrightarrow$ 35.04	2+3	$\longrightarrow$ 95.41	1+4
6	6+0	$\longrightarrow$ −100.934	5+1	$\longrightarrow$ −15.51	4+2	$\longrightarrow$ 54.91	3+3	$\longrightarrow$ 111.3198	2+4
7	7+0	$\longrightarrow$ −94.49	6+1	$\longrightarrow$ 9.18	5+2	$\longrightarrow$ 67.09	4+3	$\longrightarrow$ 121.136	3+4
8	8+0	$\longrightarrow$ −51.58	7+1	$\longrightarrow$ 14.44	6+2				4+4
9	9+0	$\longrightarrow$ −39.91	8+1						
10	10+0								

Table 5.5: Calculated Gibbs free energy changes associated with the hydrolysis of a water ligand on plutonium mixed hydrate/hydroxide complexes in COSMO-simulated solution (reaction 5.4, calculated using eqn. 5.6), in kJ mol^{-1}.

5.1.4 QTAIM

Having obtained a set of complexes spanning a range of coordination numbers and charges for the same elements, and being aware of the approximately exponential dependence of many QTAIM BCP parameters on bond length, the density and total energy density, ρ and H, were obtained for all Pu-O bonds in the structures, and are shown in figures 5.8 and 5.9. It must be noted that these are for the gas-phase densities, rather than densities obtained from calculations including COSMO.

It is apparent from these data that despite the differences in charge and ligation environment between the various complexes, the correlations between bond length and the two quantities inspected remain the same to within a reasonable margin of error. The peculiar shape of the trend in the total energy density H is due to this value being the difference between two exponentially proportional values, the potential and kinetic energy densities. In the shorter bonds, the negative potential energy is dominant, but the kinetic energy decays more slowly, so giving positive total energy density at the BCPs of the longer bonds.

To inspect whether the delocalisation index was similarly insensitive, these were also calculated for the same range of structures. These are shown in figure 5.10. It can be seen that these follow almost the same exponential decay trend as the BCP density, except that there appears to be some deviation in the shorter plutonium-water bonds in the hydrates 4+0 and 5+0, displaying a higher index than the trend would suggest. This may show enhanced covalent bonding behaviour in these under-coordinated structures, where no hydroxide ion can form a shorter bond with the plutonium. Perhaps more surprising is that the delocalisation index bond order analogue in the shortest bonds rises above 1, suggesting that these can be treated as more than singly bonded. This suggests that with the right conditions, this type of bonding interaction could be a lead-in to plutonyl-like Pu-O bond formation with the loss of a proton.

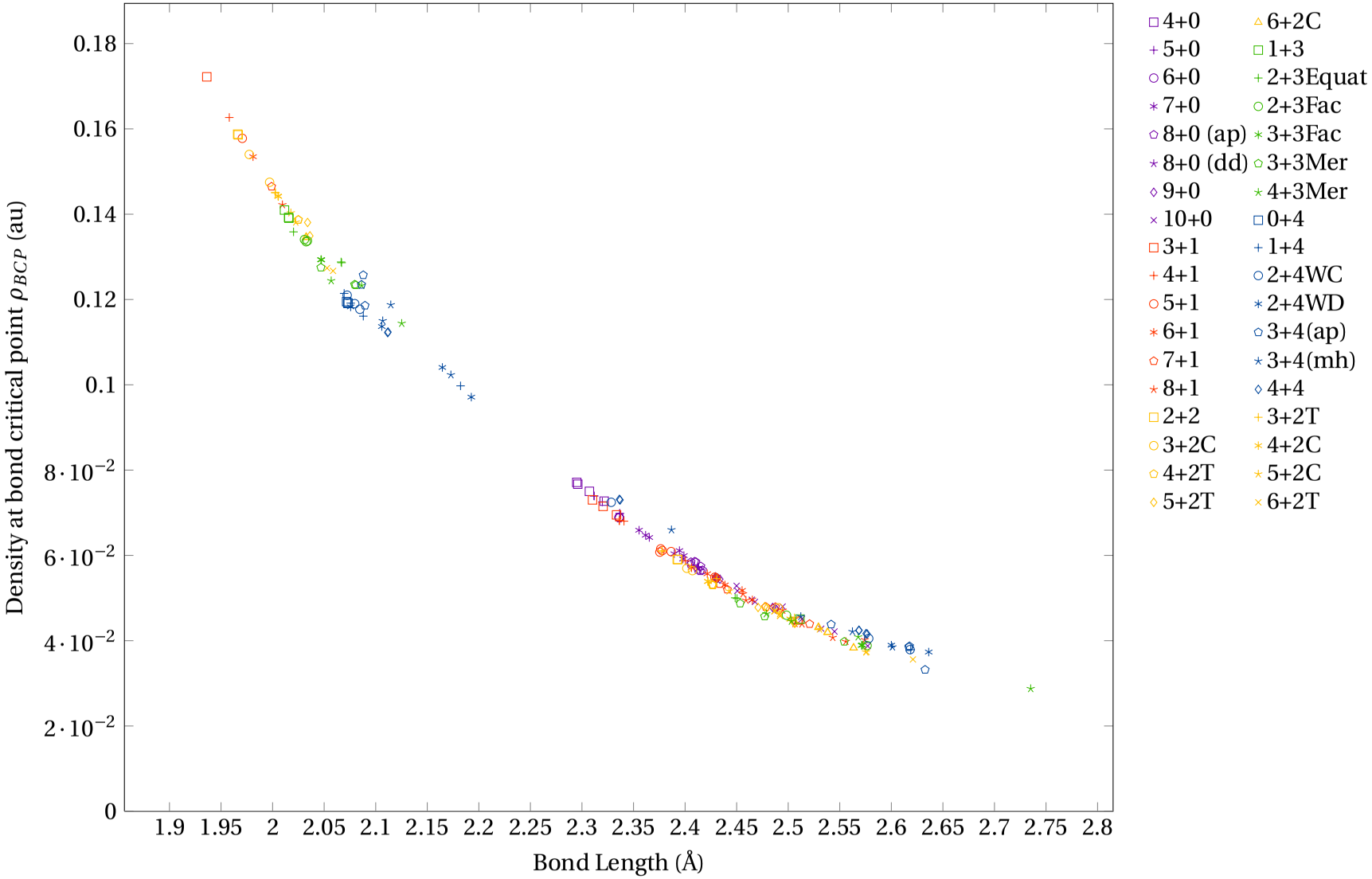

Figure 5.8: Electron density (ρ) at the Bond Critical Points for all plutonium hydrates and mixed hydrate/hydroxide complexes.

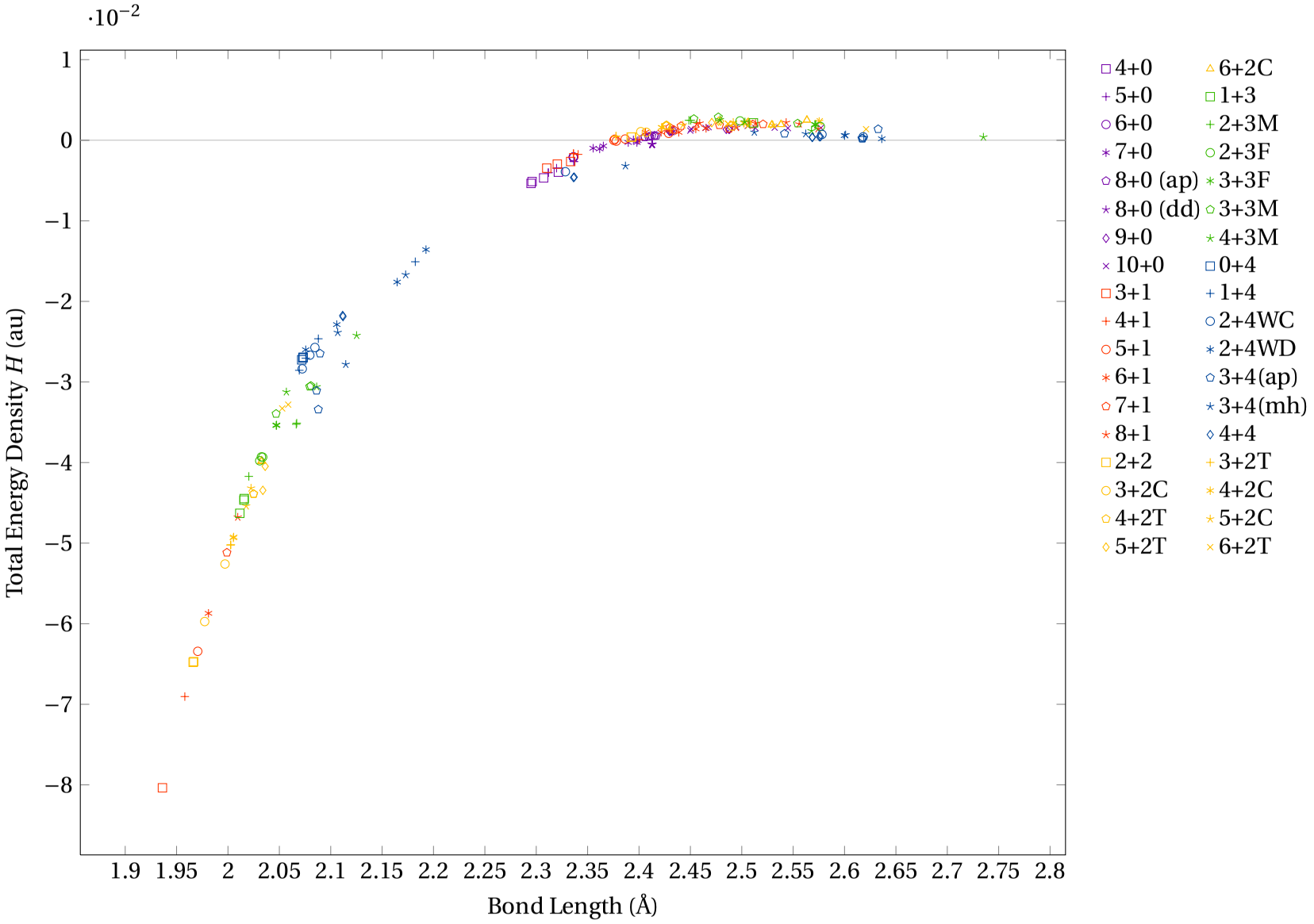

Figure 5.9: Total energy density (H) at the Bond Critical Points for all plutonium hydrates and mixed hydrate/hydroxide complexes.

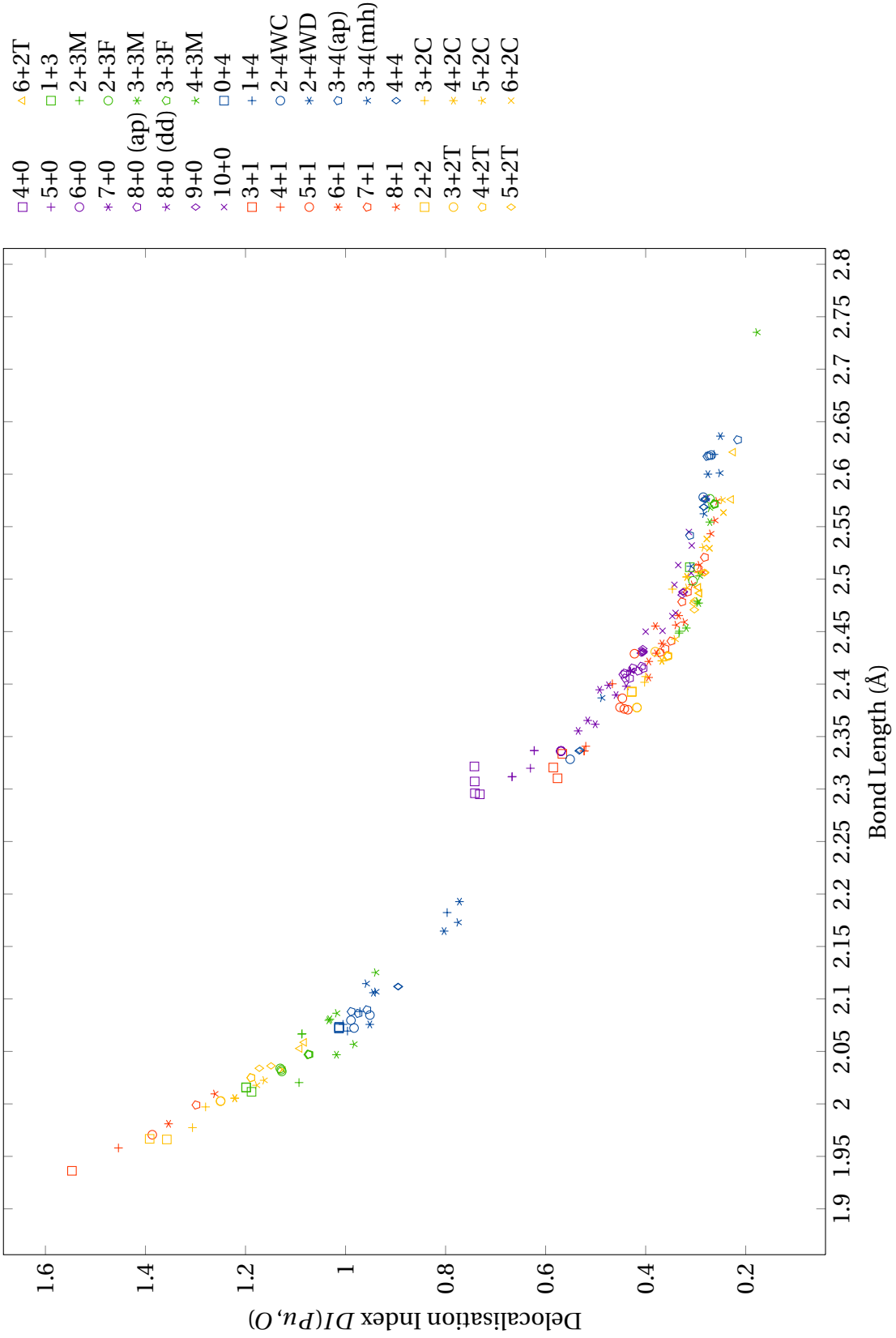

Figure 5.10: Delocalisation index between plutonium and bonding oxygen atoms plotted against bond length for all plutonium hydrates and mixed hydrate/hydroxide complexes.

5.2 Periodic System

The model solvated system comprises an NVT ensemble of one plutonium (IV) ion and 60 water molecules' worth of hydrogen and oxygen atoms.

To obtain cell dimensions, the assumption has been made that the introduction of the plutonium ion does not significantly alter the density of the water. The density of pure water at 25° C (997.0470 kg m^{-3})[104] gives a cube with sides 12.16 Å long. While it is possible to generate more accurate cell dimensions, this would itself involve a molecular dynamics procedure, and the assumption above should not significantly alter the pressure in the cell.

For the starting configurations, the cubic cells were filled with randomised water geometries using the VMD program[50]. Having selected a molecular complex to include, water molecules and protons were then removed or added manually to bring the total number of atoms (including the complex to add) down to $PuO_{60}H_{120}$. A void was then created in the centre, by simply moving atoms, where the molecular complex geometry could be added. This resulted in structures with some atoms being too near to each other near cell boundaries, which were corrected by manually moving these atoms. This doubtless introduces an initial bias in the system, however, it is expected that over sufficiently long simulations, this effect should disappear.

Two systems were created this way, system **A**, which uses as its initial complex the antiprismatic 8-coordinate hydrate (the 8+0 geometry), and **B**, which uses the complex with one water ligand and four hydroxides (the 1+4). The selection of these two configurations was made to enable both to converge to a single geometry if possible, while being far enough from equilibrium that some changes should occur in both.

5.2.1 Computational Details

CASTEP version 5.5.2 was used to perform single-point calculations and the molecular dynamics simulations on the periodic system.

As the TPSS functional used in the previous section is not implemented in the version of CASTEP used, and the use of a hybrid would have dramatically increased the computational expense, the GGA PBE functional [105] was used. This is not

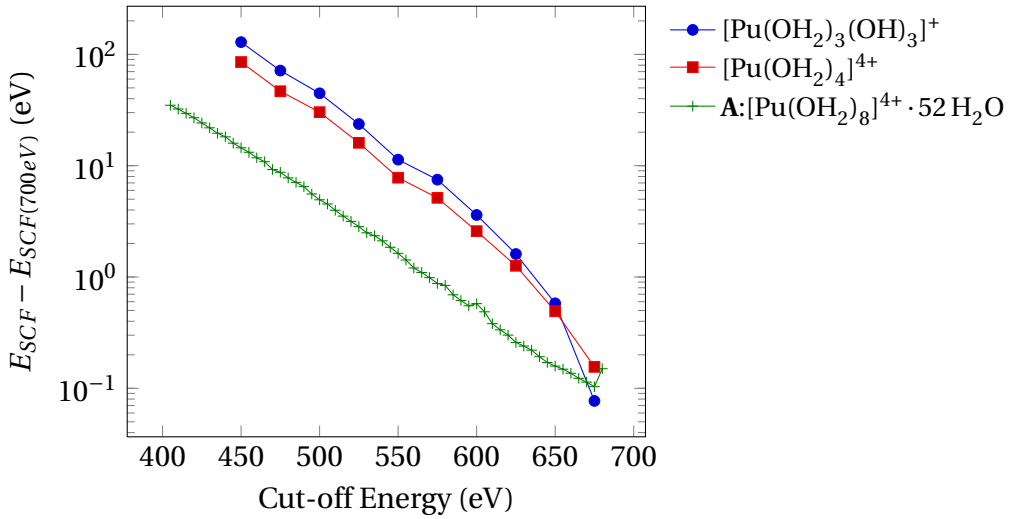

Figure 5.11: Convergence of energy of two molecular plutonium complexes and the initial configuration for system **A** with plane wave basis cut-off energy.

ideal – this functional has been shown to slightly overstructure bulk water[106] – but should still produce reasonable results and treat the plutonium in a consistent fashion [107]. This particular GGA functional was chosen because it is from the same group of functionals as TPSS.

To ensure the plane wave basis set was sufficient to model the plutonium density correctly, a succession of single-point calculations were performed using converged molecular structures from Turbomole, using a range of cut-off energies. Firstly, $[Pu(OH_2)_4]^{4+}$ and $[Pu(OH_2)_4(OH)_3]^+$ were tested to give results from two different regions of the charge and coordination number range. The SCF energy convergence from these is shown in figure 5.11, and demonstrates an acceptable convergence around 600 eV, changing by less than 4 kJ mol^{-1} between 600 and 625 eV cut-offs for both species.

Also shown are similar results computed for the starting configuration for system **A**. As the other two plots show that the plutonium is being treated adequately as this step, this verifies that the system as a whole is being treated in a consistent and sufficiently accurate way. Taking 600 eV as a possible usable value from the previous tests, the SCF energy appears adequately converged with respect to the cut-off energy, displaying only 0.3 kJ mol^{-1} per atom difference from the 700 eV SCF energy.

As previously explained (section 2.1.7, p37), the time step in a molecular dynamics calculation involving water must be short enough to obtain sufficient sam-

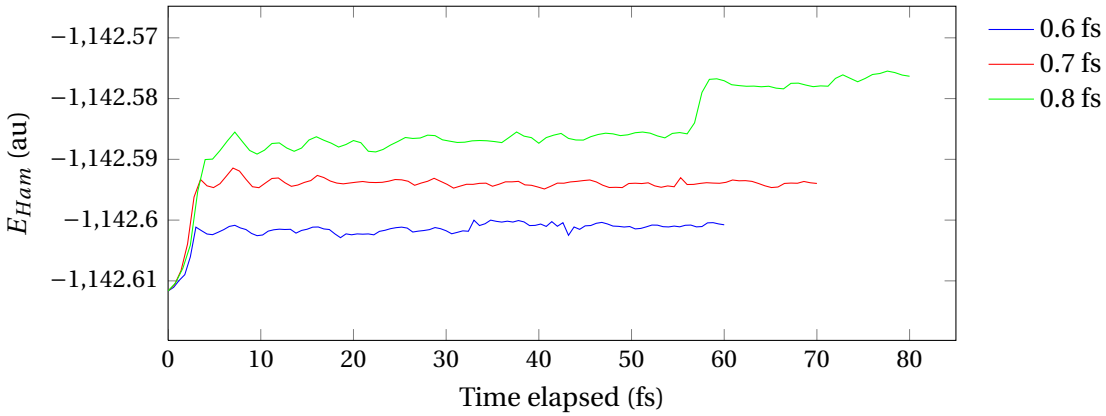

Figure 5.12: Energy of constructed Hamiltonian with time over a 100 time-step simulation of system **A**, for three different time-step lengths.

ples of hydrogen movement. Previous studies in this area have used the Car-Parrinello molecular dynamics technique, which requires much shorter time steps [108], however, for simplicity, and to avoid other problems with the technique when applied to hydrogen atoms, this study uses Born-Oppenheimer molecular dynamics. CASTEP uses a velocity Verlet algorithm [109] for Born-Oppenheimer molecular dynamics, which produces accurate trajectories over fixed time-steps.

To maintain the temperature within the cell, a Nosé-Hoover chain [32] of length 5 was used, set to approximate 298 K.

A small range of time steps were tested for short periods of motion, and the energy of the Nosé-Hoover chain pseudo-Hamiltonian [32] that sums the electronic energy of the system and the energy removed by the thermostat was plotted, as shown in figure 5.12. This pseudo-Hamiltonian is constructed such that it should be conserved over the course of the dynamic simulation [47].

While all three plots contain regions of consistency after the initial relaxation, the sudden increase in energy in the 0.8 fs plot was not fully understood but thought to be due to an undesirable interaction between the timestep and the thermostat configuration, so 0.7 fs was selected for use.

As the number of atoms is held constant over the simulation, maintaining an arbitrary pH is impossible – this and the constant volume mean that the water in the simulation should behave as if at a pH consistent with the plutonium concentration produced by the periodic conditions. Due to the strong effective acidity of the plutonium hydrate complexes combined with the limited cell-size, this is quite a low pH.

With one plutonium atom per 12.16Å-sided cube, this produces a concentration of approximately 0.924 mol dm^{-3}, and with an admittedly distant extrapolation from experimental data (the experimental data being obtained with a concentration of $10^{-8} M$ ^{238}Pu(IV)), this concentration should produce a strongly acidic environment – only taking the first hydrolysis into account, a pH of 0.37 is obtained (see appendix B).

Radial distribution functions and their integrals were computed using the VMD program [50].

5.2.2 Trajectories

Available resources allowed for systems **A** and **B** to be run for 17000 steps each – equivalent to 11.9 picoseconds. While this is a relatively short simulation, it allowed at least gauging of the time-scales involved and general behaviour of the complexes. To illustrate the changes in the first-shell complex and the remainder of the system, the plutonium-oxygen distances for both are shown in figures 5.13 and 5.15.

Unfortunately, the two trajectories do not reach the same first-shell complex. As already noted, the PBE functional has been observed previously as resulting in water that is over-structured as compared to experiment [106], which here may result in increased energetic barriers to reaction, preventing one of the systems reaching the thermodynamically most stable complex or maintaining stiff cavities over the limited time simulated.

System **A** appears to undergo one hydrolysis event (8+0 → 7+1), very near the beginning of the simulation (around 400 fs), which can be observed in expanded figure 5.14 as the shortening of one of the Pu−O distances in the inner sphere. This is then shortly followed, as per the predictions made by the study of the molecular complexes, by a single water leaving the first solvation shell (7+1 → 6+1), at around 1500-1700 fs. The resultant 6+1 complex, predicted as being the most stable configuration, then survives for the remainder of the simulation.

The 6+1 complex that forms in the dynamic simulation, however, differs in geometry from the gas-phase optimum. Shown in figure 5.17a, with the plutonium-hydroxide considered as an axis, the gas phase structure can be considered to have 5 approximately equatorial water ligands, and one axial water approximately *trans*

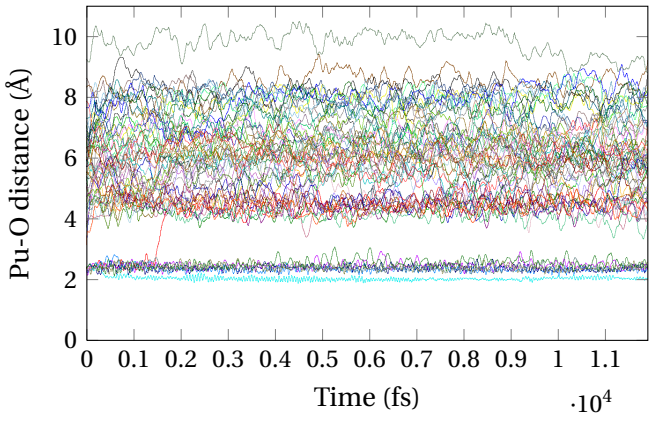

Figure 5.13: Pu-O distances over the whole trajectory of system **A** for the molecular dynamics simulation.

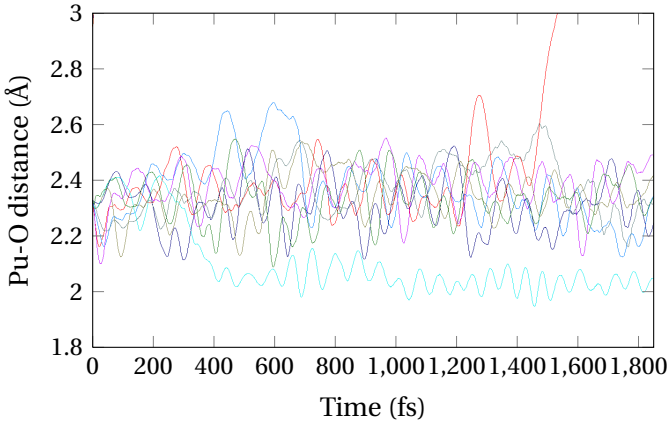

Figure 5.14: An expanded view of the primary solvation shell for Pu-O distances over the initial trajectory of system **A** for the molecular dynamics simulation, showing the single Pu-O distance reduction as a result of hydrolysis (~400fs), and the dehydration event (~1500fs).

to the hydroxide. Conversely, the dominant structure in the dynamic simulation, a representative form of which is shown in figure 5.17b (chosen randomly), can be considered as having two water ligands in axial positions with 4 water and 1 hydroxide ligands equatorial. To determine the scale of energy difference between these two forms, this structure was extracted, and only the hydrogen atom positions optimised in a COSMO field. This yielded a structure, shown in figure 5.17c, only 22 kJ mol^{-1} higher in electronic energy than the optimum gas phase structure, indicating that the water ligands are likely relatively mobile around the plutonium centre.

System **B**, started from a highly hydrolysed structure, quickly undergoes two definitive water recombination events (1+4 → 2+3 → 3+2), the first almost immediately at approximately 270 fs, and the second around 790 fs. The first is followed by

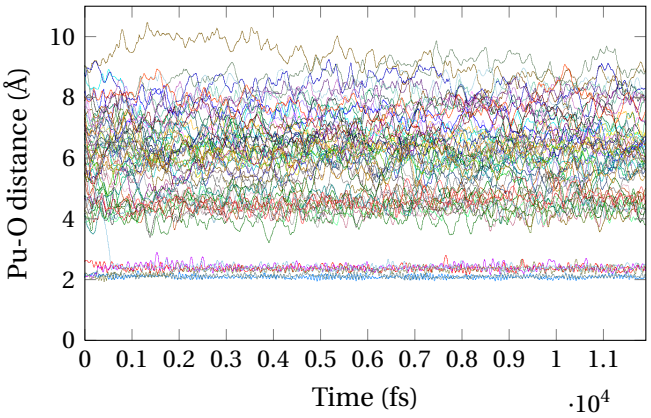

Figure 5.15: Pu-O distances over the whole trajectory of system **B** for the molecular dynamics simulation.

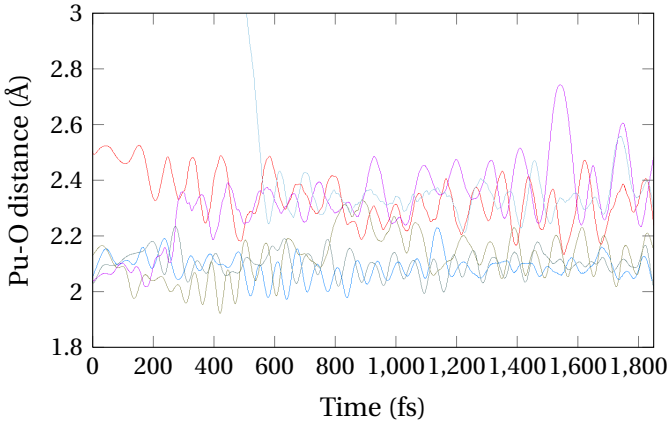

Figure 5.16: An expanded view of the primary solvation shell for Pu-O distances over the initial trajectory of system **B** for the molecular dynamics simulation, showing the two hydrolysis events (~290 and ~790 fs), and the shell expansion (~400fs).

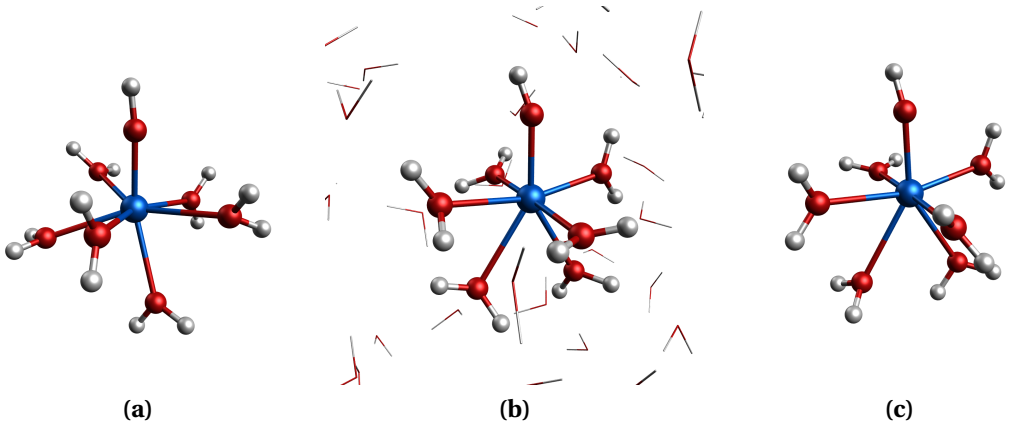

Figure 5.17: For comparison: the previously shown gas phase 6+1 structure (a) (at a slightly different angle for better comparison), a sample structure extracted from the system **A** molecular dynamics simulation at 11.28 fs (step 14100) (b), and the same structure with hydrogen atomic positions optimised in COSMO (c).

the addition of a water molecule to the solvation shell (3+2 → 4+2) at around 400 fs and taking about 150 fs to complete, which can be observed in the expanded figure 5.16. The molecular complex reaction energies predict the resulting structure as still being unstable, and correspondingly the second recombination creates a stable complex with two *trans* hydroxides and four waters (4+2T), but with a hydroxide pair geometry more closely resembling the 3+2T isolated complex (see figure 5.18a). This species persists for the remainder of the simulation. Although the primary shell plutonium-oxygen distances vary somewhat over the remaining time, no further coordination changes take place in the primary solvation shell of the plutonium or the oxygen atoms therein.

As with the snapshot of system **A**, the geometry of the complex was taken and the hydrogen positions optimised in COSMO, giving the geometry shown in figure 5.18c. This appears to be a local minimum due to the energetic barrier associated with reorienting the water molecules to allow the hydrogens that lie in the same plane as the water ligand oxygens to move to an axial alignment like the others. The resulting slight steric void may then be responsible for the difference in hydroxide hydrogen positioning.

As with the hydrogen-optimised structure from system **A**, this structure shows a small increase in energy with respect to the equivalent molecular complex, being 34 kJ mol^{-1} higher in electronic energy including COSMO contributions.

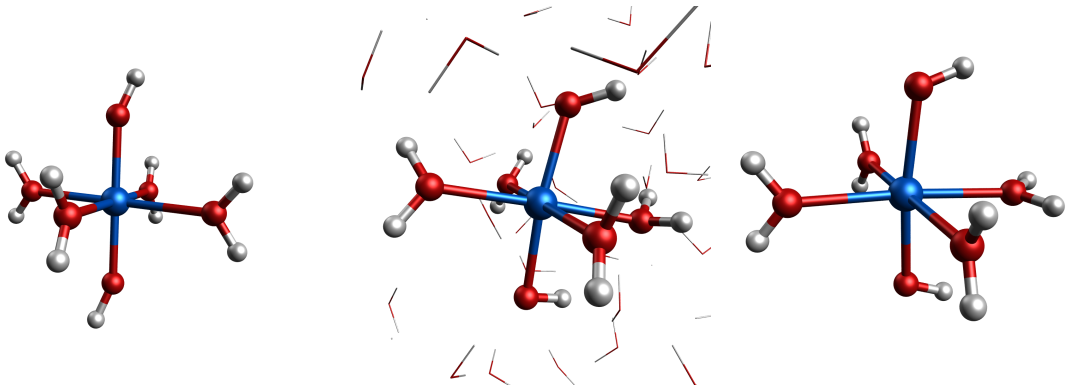

(a) **(b)** **(c)**

Figure 5.18: For comparison: the previously shown gas phase 4+2T structure (a), a sample structure extracted from the system **B** molecular dynamics simulation at 11.28 fs (step 14100) (b), and the same structure with hydrogen atomic positions optimised in COSMO (c).

5.2.3 RDFs

The peaks of the simulation Pu-O radial distribution functions can be compared with the gas phase complex geometries to obtain an approximate measure of how representative bond lengths may be – although as system **B** spent less time in the final state, it is expected that the shortest plutonium-oxygen peak may be between the value for the 4+2T and the 3+3M value. The RDF plots for systems **A** and **B** are shown in figures 5.19 and 5.20, respectively. The peaks in the RDFs each show two clearly defined distances in the primary shell radius, reflecting the Pu-O hydroxide and water distances, and these are compared with the gas complex equivalents of the final configurations in table 5.6.

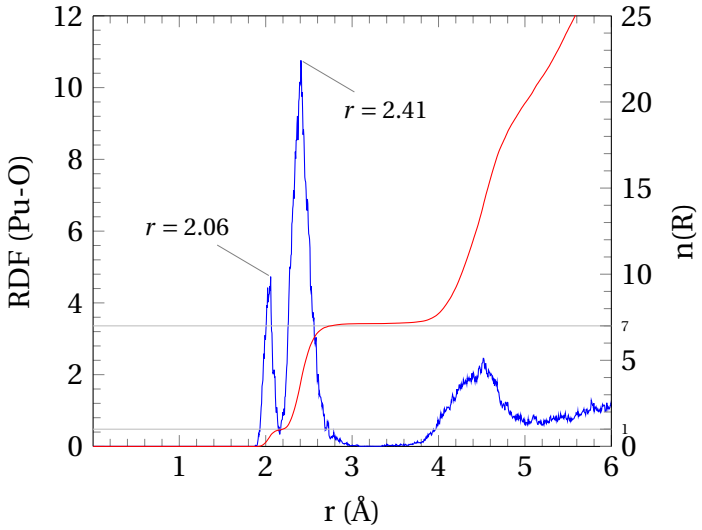

Figure 5.19: Plutonium-oxygen RDF and integration for system **A**.

Complex	Bond	Gas Phase r_{Pu-O} (Å) (av.)	RDF Peak r_{Pu-O} (Å)
6+1 / **A**	Pu−OH	1.981	2.058
	Pu−OH_2 (av.)	2.436	2.408
4+2T / **B**	Pu−OH (av.)	2.025	2.103
	Pu−OH_2 (av.)	2.426	2.373

Table 5.6: Comparison between RDF peaks and gas phase complex bond lengths in structures comparable to the final MD coordination – system **A** and 6+1, and system **B** and 4+2T.

This comparison shows a similar result for the two sets – a slight increase of the plutonium-hydroxide bond distance, and a slight decrease of the corresponding plutonium-water distance. This is unsurprising: given the addition of thermalisation, it is expected that mean bond lengths should lengthen slightly, however,

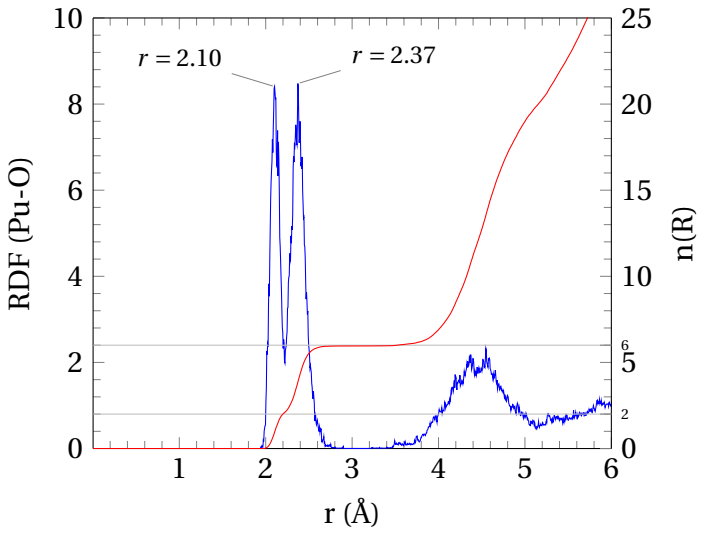

Figure 5.20: Plutonium-oxygen RDF and integration for system **B**.

the gas-phase structures suggest that longer plutonium-water distances are correlated with shorter plutonium-hydroxide distances, which would then suggest that the thermal vibration of the plutonium-hydroxide bond allows the waters to, on average, be shorter. Regardless, the differences are on the order of hundredths of an Angstrom, which suggests that the gas phase structural parameters are reasonable approximations to those found in a dynamical environment. The largest difference occurs in the more flexible bond type, the plutonium-water bond, in system **B**, which is to be expected due to the larger changes over the course of the simulation as compared to **A**.

Despite the larger changes, the RDF integrations for both systems clearly reflect the dominant species for the first solvation shell, showing 1 closer ligand and 6 more distant ones in system **A**, and 2 closer and 4 more distant in **B**. As in the distance plots in figures 5.13 and 5.15, the separation between first and second solvation shell is well defined, and there is really insufficient solvent to express definition beyond that in the second shell. What is present suggests a more weakly defined second shell, with around 11-14 water molecules, following the approximate $< 2:1$ ratio that could be expected due to hydrogen bonding.

5.3 Conclusions

Combined primary solvation cluster/continuum techniques appear to produce reasonable hydrolysis and dehyration stability trends for plutonium mixed hydrox-

ide/water complexes, in comparison with similar studies on analogous polonium compounds and the little available experimental data. The correlation between increasing degrees of hydrolysis and dehydration noted in other species is reproduced, and the optimal water-only complex is identified as 8-coordinate with no asphericity, in agreement with EXAFS data. A significant *trans* effect is noted in complexes including hydroxide ligands.

QTAIM analysis of these complexes shows that the differences between the density characteristics for the bond critical point of a Pu−OH and a Pu−OH_2 bond of the same length are small in commonly considered metrics. More accurate probing of density across the bonding region might reveal useful trends, but the limited nature of the data obtained here mostly serves to confirm the strong dependence on bond length.

Molecular dynamics techniques appear to reproduce hydrolysis and solvation shell changes expected from the results of the cluster calculations, but require several orders of magnitude greater computational expense. The techiques used here, however, must be expanded on to obtain energetic data – with longer, more parametrically tested simulations, and enhanced sampling methods that guarantee a wider coverage of the potential surface, and allow the reliable recreation of energies with respect to variables, such as the metadynamics simulation of uranium (IV) performed very recently [90]. It must additionally be borne in mind that the absence of counter-ions can affect results obtained using these periodic techniques, and especially the solvation shells of the ions – weak associations between anions and cations can cause additional ordering of the solvent and thus cause structural formations not observed in this type of system. Individual oxygen atoms do not appear to travel significantly, and ordinary water exchange is not observed over the course of the simulations. At this stage, however, it is not possible to tell whether this is due to the short time period covered by the simulations, a limitation in the approximations of the DFT methods used, or the properties of the real system.

Clearly this is merely an initial stage for many paths of investigation, however, the work presented thus far is the limit of the scope of this study.

Chapter 6

General Conclusions

Clearly there are general trends visible in many metrics commonly associated with bonding, going from thorium to curium, and some of these metrics suggest interaction beyond simple ionic attraction between metal and ligand. Trends shown vary between techniques, with some suggesting that non-ionic M-L interactions are significantly increased in americium and curium compounds of each of the series studied. However, evidence from topological density analysis suggests that this interaction does not necessarily lead to enhanced metal-ligand bonding in these systems. Orbital forms of the various valence orbitals suggest that the part of the interaction which is enhanced may be primarily M−L non- or anti-bonding in character, which leads to false positives in methods which primarily look for orbital mixing and expect to be able to ascribe that to bonding.

It is clear that despite general correlations between QTAIM bonding-related data and bond length, such as those demonstrated here for a range of Pu-O bond lengths, differences between actinide complexes at a fixed geometry are indicative of the trends in the optimised structures for the systems studied.

It is the hope of the author that future work may be able to correlate the quantitative data obtained from QTAIM strongly with an experimentally measurable value directly associated with M−L bonding energy, and that future molecular dynamics simulations may aid in this endeavour, using more computationally expensive methods that can obtain wide energy surfaces.

Additionally, current reference data for these QTAIM techniques in actinides are not widespread. As more data become available and cross-comparable, the techniques become more valuable to understand and quantitatively analyse bonds in

other systems – one of the key parts of the initial work performed for the cited work on $AnCp_4$ systems [73] involved performing QTAIM analysis on a range of organic and inorganic systems, to obtain a scale to base obtained results for the target systems against. There are a number of other analysis techniques based on topological density analysis, including ELF and ELI-D, but QTAIM appears to be conceptually the simplest. This should aid in the spread of use of techniques based on it and make it easier to relate data obtained with it to work in other fields of chemistry, which is, after all, one of the main aims of computational chemistry.

Regardless of the state of these analysis techniques, however, molecular dynamics has an important role to play in the prediction of behaviour of actinide species in extraction environments, which, with more simulational effort, could be instrumental in the design of new extractant systems.

Appendix A

Data used to Construct Graphs

The following tables contain all data used in a graph in the preceding chapters, arranged by figure index.

	Mean r_{An-C} (Å)	
An	$AnCp_3$	$AnCp_4$ [73]
Th	2.800	2.894
Pa	*2.769*	2.848
U	2.737	2.841
Np	*2.739*	2.832
Pu	2.741	2.832
Am	2.755	2.863
Cm	2.768	2.888

Table A.1: Mean actinide-carbon bond lengths for $AnCp_3$ and $AnCp_4$ (from [73], and the interpolated bond lengths (in italics) used for the complexes for which optimal geometries could not be obtained. Used in figure 3.3.

Method	Th	Pa	U	Np	Pu	Am	Cm
Mulliken, PBE	-0.078	-0.197	-0.106	0.078	0.227	0.390	-0.001
Mulliken, PBE0	-0.054	-0.141	0.003	0.108	0.227	0.352	0.111
QTAIM, PBE	-0.288	-0.412	-0.267	-0.086	0.054	0.227	-0.129

Table A.2: Deviation from formal integer spin (Δ Spin) on the actinide shown by Mulliken analysis and integration of the QTAIM basins, in the $AnCp_3$ complexes. (Mulliken data taken from the all-electron calculations in G09.) Used in figure 3.8.

	Func.	Th	Pa	U	Np	Pu	Am	Cm
ρ_{BCP}	PBE	0.0384	0.0397	0.0404	0.0387	0.0375	0.0354	0.0342
	PBE0	0.0385	0.0400	0.0401	0.0391	0.0376	0.0356	0.0342
$\nabla^2\rho_{BCP}$	PBE	0.0961	0.1000	0.1104	0.1142	0.1145	0.1117	0.1068
	PBE0	0.0974	0.1005	0.1150	0.1169	0.1166	0.1128	0.1083
H_{BCP}	PBE	-0.00293	-0.00293	-0.00284	-0.00208	-0.00156	-0.00090	-0.00095
	PBE0	-0.00311	-0.00328	-0.0028	-0.00241	-0.00173	-0.00113	-0.00109

Table A.3: QTAIM bond critical point data plots for An-C bonds in $AnCp_3$. All quantities are in atomic units. Used in figure 3.9.

An	Th	Pa	U	Np	Pu	Am	Cm
$Q(\Omega_{An})$	1.803	1.782	1.791	1.707	1.638	1.577	1.708

Table A.4: Net charge obtained by integrating the density within the actinide QTAIM atomic basin in the density of the $AnCp_3$ complexes obtained with PBE. Used in figure 3.11.

An	Th	Pa	U	Np	Pu	Am	Cm
$\sum DI(An,C)$	3.62	4.18	4.01	3.77	3.68	3.41	3.03

Table A.5: The totalled delocalisation indices for the An-C bonding interactions in each $AnCp_3$ system, calculated with the PBE functional. Used in figure 3.12.

Isodensity	Th	Pa	U	Np	Pu	Am	Cm
0.0004	226.1	198.1	161.6	156.3	154.4	156.4	152.3
0.001	205.4	182.8	154.8	150.7	148.9	150.0	146.7
0.002	188.3	169.8	147.4	144.3	142.5	143.0	140.0

Table A.6: Volume of the QTAIM actinide atomic basin in $AnCp_3$ calculated with PBE, bounded by successive isodensity envelopes. All values are in atomic units. Used in figure 3.13.

Ligand	Bond	Th	Pa	U	Np	Pu	Am	Cm	Bk
^{Ar}acnac(expt.)	An-N	2.706		2.667		2.557			
	An-O	2.316		2.258		2.177			
^{Ar}acnac	An-N					2.732			
	An-O					2.236			
^{Ph}acnac	An-N	2.763	2.665	2.670	2.702	2.708	2.729	2.764	2.716
	An-O	2.284	2.180	2.182	2.208	2.230	2.254	2.293	2.206
^{Ph}beki	An-N	2.730	2.637	2.636	2.652	2.671	2.718	2.728	2.676
	An-O	2.316	2.215	2.223	2.247	2.262	2.291	2.339	2.241
^{Ph}beki(PBE0)	An-N	2.708	2.587	2.606		2.586		2.684	2.585
	An-O	2.334	2.210	2.240		2.246		2.349	2.210

Table A.7: Average An−N and An−O bond length comparisons for actinide complexes with the ^{Ar}acnac ligand, measured experimentally, and the complexes optimised computationally with PBE with ligands ^{Ar}acnac, ^{Ph}acnac, and ^{Ph}beki, and the ^{Ph}beki complexes optimised with PBE0. All figures are in Å. Used in figures 4.3 and 4.6.

	PBE		PBE0	
	An-O	An-N	An-O	An-N
Th	0.000291	0.000981	0.001562	0.002404
Pa	0.000521	0.000668	-0.002569	-0.009154
U	-0.000578	0.001094	-0.000694	-0.001205
Np	-0.009561	0.069004	–	–
Pu	-0.001195	0.001162	-0.000494	-0.00147
Am	0.004814	-0.017728	–	–
Cm	-0.000593	-0.00385	0.074213	0.16594
Bk	0.003227	0.001049	-0.001288	0.001425

Table A.8: The difference between the sets of bond distances for the two pairs of ligands in the ^{Ph}beki complexes. Sign is preserved to show correlation. All units are Å. Used in figure 4.7.

	Δ Spin Density			
An	^{Ph}acnac Mul. PBE	^{Ph}beki Mul. PBE	^{Ph}beki Mul. PBE0	^{Ph}beki QTAIM PBE0
Th	0	0	0	0
Pa	-0.5873	-0.4431	-0.5622	-0.666
U	-0.1836	-0.0688	-0.0235	-0.024
Np	0.2036	0.2579	–	–
Pu	0.4839	0.5142	0.1932	-0.000
Am	0.7247	0.7967	–	–
Cm	0.8489	0.8826	1.0127	0.795
Bk	-0.8513	-0.8410	-0.2552	-0.175

Table A.9: Deviation from formal integer spin on the actinide shown in the Mulliken spin density and the QTAIM spin density data, in the An(^{Ph}acnac)$_4$ and An(^{Ph}beki)$_4$ complexes. Used in figure 4.12.

	Mulliken Spin				
An	O	C_O	C_{back}	C_N	N
Th	0	0	0	0	0
Pa	-0.0085	0.0734	-0.0235	0.0756	-0.0018
U	-0.0293	0.0485	-0.0220	0.0501	-0.0200
Np	-0.0411	0.0296	-0.0256	0.0272	-0.0384
Pu	-0.0572	0.0240	-0.0299	0.0217	-0.0587
Am	-0.0633	0.0187	-0.0613	0.0239	-0.0757
Cm	-0.0315	-0.0032	-0.0930	0.0273	-0.0758
Bk	0.0623	-0.0182	0.05485	-0.011	0.0888

Table A.10: Mulliken spin for atoms on the central ligand loop, averaged over the four ligands, in the $An(^{Ph}beki)_4$ systems calculated with PBE. Used in figure 4.13.

	Mulliken Spin				
An	O	C_O	C_{back}	C_N	N
Th	0	0	0	0	0
Pa	-0.0136	0.1094	-0.0475	0.1115	-0.0119
U	-0.0225	0.0383	-0.0206	0.0443	-0.0268
Pu	-0.0255	0.0198	-0.0160	0.0183	-0.0365
Cm	-0.0480	0.0093	-0.1237	0.0592	-0.1077
Bk	0.0329	-0.0108	0.0186	-0.0037	0.0184

Table A.11: Mulliken spin for atoms on the central ligand loop, averaged over the four ligands, in the $An(^{Ph}beki)_4$ systems calculated with PBE0. Used in figure 4.14.

	Δ Spin	
An	$An(^{Ph}beki)_4$	AnO_2
Th	0	0
Pa	-0.4431	-0.0652
U	-0.0688	-0.0509
Np	0.2579	-0.0170
Pu	0.5142	-0.0145
Am	0.7967	-0.0631
Cm	0.8826	0.2064
Bk	-0.8410	-0.4824

Table A.12: Deviation from formal integer spin on the actinide shown in the Mulliken spin density, in the $An(^{Ph}beki)_4$ complexes as compared with the actinide dioxide[82]. Used in figure 4.15.

	Natural Populations				
An	7s	7p	6d	5f	Q_{An}
Th	0.21	0.30	1.07	0.70	1.62
Pa	0.22	0.34	1.24	0.72	1.36
U	0.21	0.34	1.16	0.99	1.14
Np	0.22	0.34	1.08	1.11	1.13
Pu	0.23	0.34	1.00	1.18	1.20
Am	0.23	0.32	0.93	1.11	1.39
Cm	0.16	0.22	0.90	1.10	1.43
Bk	0.27	0.35	0.98	0.60	1.69

Table A.13: NPA actinide charges (Q_{An}) and deviations from formal occupations (Δ Occ) in the An(^{Ph}beki)$_4$ complexes, using the PBE functional. Note that this assumes all actinide (IV) ions are formally $6d^0$. Used in figures 4.16a and 4.16b.

	Natural Populations				
An	7s	7p	6d	5f	Q_{An}
Th	0.19	0.29	0.87	0.08	1.97
Pa	0.21	0.32	1.28	0.22	1.93
U	0.20	0.31	0.91	0.65	1.61
Pu	0.23	0.35	0.97	0.65	1.53
Cm	0.22	0.31	0.68	0.98	1.68
Bk	0.26	0.36	1.00	0.34	1.91

Table A.14: NPA actinide charges (Q_{An}) and deviations from formal occupations (Δ Occ) in the An(^{Ph}beki)$_4$ complexes, using the PBE0 functional. Note that this assumes all actinide (IV) ions are formally $6d^0$. Used in figures 4.17a and 4.17b.

		Deloc. Index	
An	Q_{An}	An-O	An-N
Th	2.87	0.44	0.25
Pa	3.02	0.61	0.34
U	2.67	0.54	0.30
Pu	2.60	0.52	0.32
Cm	2.25	0.39	0.25
Bk	2.58	0.51	0.28

Table A.15: Actinide charges and delocalisation indices for the An−O and An−N basins (averaged over the four ligands), with the PBE0 functional. Used in figure 4.19.

	Pu-O(w)					Pu-O(h)			
CN	n+0	n+1	n+2	n+3	n+4	n+1	n+2	n+3	n+4
4	2.30	2.32	2.39	2.51	–	1.94	1.97	2.01	2.07
5	2.32	2.35	2.40	2.45	2.62	1.96	2.00	2.05	2.10
6	2.34	2.39	2.43	2.49	2.62	1.97	2.02	2.07	2.13
7	2.38	2.44	2.49	2.57	2.56	1.98	2.04	2.09	2.20
8	2.41	2.47	2.53	–	2.57	2.00	2.06	–	2.22
9	2.45	2.51	–	–	–	2.01	–	–	–
10	2.50	–	–	–	–	–	–	–	–

Table A.16: Average Pu-O(water) and Pu-O(hydroxide) bond lengths per complex in optimal mixed hydrate/hydroxide complexes. $n+m$ indicates a complex with n water ligands and m hydroxide ligands. Used in figure 5.7.

Appendix B

Calculations

Calculation of the pH of a Given Plutonium Solution

Making the approximation that only the first hydrolysis occurs, the equilibrium constant is related to the concentrations at equilibrium thus:

$$K = \frac{[Pu(OH)]\,[H_3O]}{[Pu]} \tag{B.1}$$

(Charges have been omitted for clarity.) Using the $\log K'$ for the first hydrolysis of plutonium (IV) obtained in [93], -0.45, and an initial plutonium concentration (c_0), it is then possible to obtain a quadratic expression, the positive root of which expresses the equilibrium concentration of H_3O^+ (c_+) assuming the system initially contained pure water. For the concentration 0.924 mol dm^{-3} used in the periodic system, this gives:

$$c_+^2 + K'c_+ - K'c_0 = 0 \tag{B.2}$$

which is then soluble to obtain a single positive root, and thus a concentration of $[H_3O]^+$, *ca.* 0.4220 mol dm^{-3}. Taking the negative $\log_{10}$, this equates to a pH of approximately 0.37 – extremely acidic.

Appendix C

Colophon

This document was set in the Utopia typeface using LaTeX and BibTeX, composed with the TeXmaker editor. The PGFplots package was used to set the majority of graphs, with a small number (those having many thousands of data points) being rendered using the gnuplot package and then having axes overlaid using PGFplots. For display, molecular orbitals were converted to cube files, passed into the Avogadro molecular visualisation tool for conversion into splined surfaces, and then rendered using the POVRay ray-tracer. Hydrogenic orbitals were rendered directly from *ab initio* isosurfaces in POVRay.

Bibliography

[1] Nikolas Kaltsoyannis and Peter Scott. *The f elements*. OUP, 1999.

[2] David L. Clark, Siegfried S. Hecker, Gordon D. Jarvinen, and Mary P. Neu. *The Chemistry of the Actinide and Transactinide Elements – Vol. 2 – Plutonium*. Springer, 2006.

[3] Helen Steele and Robin J. Taylor. A Theoretical Study of the Inner-Sphere Disproportionation Reaction Mechanism of the Pentavalent Actinyl Ions. *Inorganic Chemistry*, 46(16):6311–6318, July 2007.

[4] P. Pyykkö. Dirac-Fock One-Centre Calculations Part 8. The 1Σ States of ScH, YH, LaH, AcH, TmH, LuH and LrH. *Physica Scripta*, 20(5-6):647+, January 2007.

[5] Andrew Kerridge, Rosemary Coates, and Nikolas Kaltsoyannis. Is Cerocene Really a Ce(III) Compound? All-Electron Spin-Orbit Coupled CASPT2 Calculations on $M(\nu^8-C_8H_8)_2$ (M = Th, Pa, Ce). *Journal of Physical Chemistry A*, 113(12):2896–2905, March 2009.

[6] Michael L. Neidig, David L. Clark, and Richard L. Martin. Covalency in f-element complexes. *Coordination Chemistry Reviews*, May 2012.

[7] Peter G. Edwards, Mary Harman, Michael B. Hursthouse, and Julian S. Parry. The synthesis and crystal structure of the thorium tetraphosphido complex, $Th[P(CH_2CH_2PMe_2)_2]_4$, an actinide complex with only metal-phosphorus ligand bonds. *Journal of the Chemical Society, Chemical Communications*, (19):1469–1470, 1992.

[8] Kieran I. M. Ingram, Matthew J. Tassell, Andrew J. Gaunt, and Nikolas Kaltsoyannis. Covalency in the f element-chalcogen bond. Computational studies of $M[N(EPR_2)_2]_3$ (M = La, Ce, Pr, Pm, Eu, U, Np, Pu, Am, Cm; E = O, S, Se, Te; R = H, Pr-i, Ph). *Inorganic Chemistry*, 47(17):7824–7833, September 2008.

[9] Jessie L. Brown, Skye Fortier, Richard A. Lewis, Guang Wu, and Trevor W. Hayton. A complete family of terminal uranium chalcogenides, $[U(E)(NSiMe3_2)_3]^+$ (e = o, s, se, te). *Journal of the American Chemical Society*, 134(37):15468–15475, August 2012.

[10] Marina Porchia, Franco Ossola, Gilberto Rossetto, Pierino Zanella, and Nicola Brianese. Synthesis of triscyclopentadienyl(triphenylgermyl)uranium and facile isonitrile insertion into the uranium-germanium bond. *Journal of the Chemical Society, Chemical Communications*, (8):550–551, 1987.

[11] Slimane Doudou, Krishnamoorthy Arumugam, David J. Vaughan, Francis R. Livens, and Neil A. Burton. Investigation of ligand exchange reactions in aqueous uranyl carbonate complexes using computational approaches. *Physical Chemistry Chemical Physics*, 13(23):11402–11411, 2011.

[12] Daniel Rios, Maria del Carmen Michelini, Ana F. Lucena, Joaquim Marçalo, and John K. Gibson. On the Origins of Faster Oxo Exchange for Uranyl(V) versus Plutonyl(V). *Journal of the American Chemical Society*, 134(37):15488–15496, September 2012.

[13] Kevin S. Boland, Steven D. Conradson, Alison L. Costello, Andrew J. Gaunt, Stosh A. Kozimor, Iain May, Sean D. Reilly, and David D. Schnaars. Stabilising pentavalent actinides-visible-near infrared and X-ray absorption spectroscopic studies of the utility of the $[(Np_3W_4O_{15})(H_2O)_3(MW_9O_{33})_3]^{18-}$ (M = Sb, Bi) structural type. *Dalton Transactions*, 41(7):2003–2010, 2012.

[14] David M. King, Floriana Tuna, Eric J. L. McInnes, Jonathan McMaster, William Lewis, Alexander J. Blake, and Stephen T. Liddle. Synthesis and Structure of a Terminal Uranium Nitride Complex. *Science*, 337(6095):717–720, August 2012.

[15] R.B. Matthews, K.M. Chidester, C.W. Hoth, R.E. Mason, and R.L. Petty. Fabrication and testing of uranium nitride fuel for space power reactors. *Journal of Nuclear Materials*, 151(3):345, 1988.

[16] E.A. Kotomin, Yu.A. Mastrikov, S.N. Rashkeev, and P. Van Uffelen. Implementing first principles calculations of defect migration in a fuel performance code for un simulations. *Journal of Nuclear Materials*, 393(2):292 – 299, 2009.

[17] David P. Mills, Fabrizio Moro, Jonathan McMaster, Joris van Slageren, William Lewis, Alexander J. Blake, and Stephen T. Liddle. A delocalized arene-bridged diuranium single-molecule magnet. *Nature Chemistry*, 3(6):454–460, June 2011.

[18] Qing-Jiang Pan, Grigory A Shamov, and Georg Schreckenbach. Binuclear Uranium(VI) Complexes with a 'Pacman'İ Expanded Porphyrin: Computational Evidence for Highly Unusual Bis-Actinyl Structures. *Chemistry - A European Journal*, 16(7):2282–2290, 2010.

[19] Jeffrey D. Rinehart, T. David Harris, Stosh A. Kozimor, Bart M. Bartlett, and Jeffrey R. Long. Magnetic Exchange Coupling in Actinide-Containing Molecules. *Inorganic Chemistry*, 48(8):3382–3395, April 2009.

[20] Tori Z Forbes, J. . Gregory McAlpin, Rachel Murphy, and Peter C Burns. Metal–Oxygen Isopolyhedra Assembled into Fullerene Topologies. *Angewandte Chemie*, 120(15):2866–2869, 2008.

[21] Els van Besien, Kristine Pierloot, and Christiane Gorller-Walrand. Electronic spectra of uranyl chloride complexes in acetone: a CASSCF/CASPT2 investigation. *Physical Chemistry Chemical Physics*, 8(37):4311–4319, 2006.

[22] Th Kowall, F. Foglia, L. Helm, and A. E. Merbach. Molecular Dynamics Simulation Study of Lanthanide Ions Ln^{3+} in Aqueous Solution Including Water Polarization. Change in Coordination Number from 9 to 8 along the Series. *Journal of the American Chemical Society*, 117(13):3790–3799, April 1995.

[23] S. D. Conradson, K. D. Abney, B. D. Begg, E. D. Brady, D. L. Clark, C. den Auwer, M. Ding, P. K. Dorhout, F. J. Espinosa-Faller, P. L. Gordon, R. G. Haire, N. J. Hess, R. F. Hess, D. W. Keogh, G. H. Lander, A. J. Lupinetti, L. A. Morales, M. P. Neu, P. D. Palmer, P. Paviet-Hartmann, S. D. Reilly, W. H. Runde, C. D. Tait, D. K. Veirs, and F. Wastin. Higher Order Speciation Effects on Plutonium L-3 X-ray

Absorption Near Edge Spectra. *Inorganic Chemistry*, 43(1):116–131, January 2004.

[24] P. Hohenberg and W. Kohn. Inhomogeneous electron gas. *Phys. Rev.*, 136:B864–B871, 1964.

[25] Frank Jensen. *Introduction to Computational Chemistry*. Wiley, 2 edition, December 2006.

[26] Markus Reiher. Relativistic Douglas-Kroll-Hess theory. *WIREs Comput Mol Sci*, 2(1):139–149, 2012.

[27] Xiaoyan Cao, Michael Dolg, and Hermann Stoll. Valence basis sets for relativistic energy-consistent small-core actinide pseudopotentials. *The Journal of Chemical Physics*, 118(2):487–496, 2003.

[28] W. Kohn and L. J. Sham. Self-consistent equations including exchange and correlation effects. *Phys. Rev.*, 140:A1133–A1138, 1965.

[29] John P. Perdew and Karla Schmidt. Jacob's ladder of density functional approximations for the exchange-correlation energy. *AIP Conference Proceedings*, 577(1):1–20, 2001.

[30] Osamu Sugino and Roberto Car. *Ab Initio* molecular dynamics study of first-order phase transitions: Melting of silicon. *Physical Review Letters*, 74:1823–1826, March 1995.

[31] Hendrik Buiteveld, J. H. M. Hakvoort, and M. Donze. Optical properties of pure water. *Proceedings of SPIE*, 2258(1):174–183, October 1994.

[32] G. L. Martyna, M. L. Klein, and M. Tuckerman. Nosé-Hoover chains: The canonical ensemble via continuous dynamics. *J. Chem. Phys.*, 97:2635–2645, 1992.

[33] A. Klamt and G. Schuurmann. COSMO: a new approach to dielectric screening in solvents with explicit expressions for the screening energy and its gradient. *Journal of the Chemical Society, Perkin Transactions 2*, (5):799–805, 1993.

[34] Yu Takano and K. N. Houk. Benchmarking the Conductor-like Polarizable Continuum Model (CPCM) for Aqueous Solvation Free Energies of Neutral and Ionic Organic Molecules. *Journal of Chemical Theory and Computation*, 1(1):70–77, November 2004.

[35] R. S. Mulliken. Electronic Population Analysis on LCAO[Single Bond]MO Molecular Wave Functions. *The Journal of Chemical Physics*, 23(10):1833–1840, 1955.

[36] Richard F. W. Bader. *Atoms in Molecules: A Quantum Theory (International Series of Monographs on Chemistry)*. Oxford University Press, USA, June 1994.

[37] AIMAll (Version 12.11.09), Todd A. Keith, TK Gristmill Software, Overland Park KS, USA, 2012, URL: http://aim.tkgristmill.com/.

[38] Claire V. J. Skipper, Tuan K. A. Hoang, David M. Antonelli, and Nikolas Kaltsoyannis. Transition Metal Hydrazide-Based Hydrogen-Storage Materials: the First Atoms-In-Molecules Analysis of the Kubas Interaction. *Chemistry - A European Journal*, 18(6):1750–1760, 2012.

[39] Louis J. Farrugia and Hans M. Senn. Metal-Metal and Metal-Ligand Bonding at a QTAIM Catastrophe: A Combined Experimental and Theoretical Charge Density Study on the Alkylidyne Cluster $Fe_3(\mu-H)(\mu-COMe)(CO)_{10}$. *Journal of Physical Chemistry A*, 114(51):13418–13433, December 2010.

[40] Alan E. Reed, Robert B. Weinstock, and Frank Weinhold. Natural population analysis. *The Journal of Chemical Physics*, 83(2):735–746, 1985.

[41] Aurora E. Clark, Jason L. Sonnenberg, P. Jeffrey Hay, and Richard L. Martin. Density and wave function analysis of actinide complexes: What can fuzzy atom, atoms-in-molecules, Mulliken, Løwdin, and natural population analysis tell us? *The Journal of Chemical Physics*, 121(6):2563–2570, 2004.

[42] G. te Velde, F.M. Bickelhaupt, S.J.A. van Gisbergen, C. Fonseca Guerra, E.J. Bartends, J.G. Snijders, and T. Ziegler. Chemistry with adf. *J. Comp. Chem.*, 22:931, 2001.

[43] ADF 2010, SCM, Theoretical Chem., Vrije Univeriteit, Amsterdam, The Netherlands, URL: http://www.scm.com/.

[44] M. J. Frisch, G. W. Trucks, H. B. Schlegel, G. E. Scuseria, M. A. Robb, J. R. Cheeseman, G. Scalmani, V. Barone, B. Mennucci, G. A. Petersson, H. Nakatsuji, M. Caricato, X. Li, H. P. Hratchian, A. F. Izmaylov, J. Bloino, G. Zheng, J. L. Sonnenberg, M. Hada, M. Ehara, K. Toyota, R. Fukuda, J. Hasegawa, M. Ishida, T. Nakajima, Y. Honda, O. Kitao, H. Nakai, T. Vreven, J. A. Montgomery, Jr., J. E. Peralta, F. Ogliaro, M. Bearpark, J. J. Heyd, E. Brothers, K. N. Kudin, V. N. Staroverov, R. Kobayashi, J. Normand, K. Raghavachari, A. Rendell, J. C. Burant, S. S. Iyengar, J. Tomasi, M. Cossi, N. Rega, J. M. Millam, M. Klene, J. E. Knox, J. B. Cross, V. Bakken, C. Adamo, J. Jaramillo, R. Gomperts, R. E. Stratmann, O. Yazyev, A. J. Austin, R. Cammi, C. Pomelli, J. W. Ochterski, R. L. Martin, K. Morokuma, V. G. Zakrzewski, G. A. Voth, P. Salvador, J. J. Dannenberg, S. Dapprich, A. D. Daniels, Ö. Farkas, J. B. Foresman, J. V. Ortiz, J. Cioslowski, and D. J. Fox. Gaussian 09 Revision A.1. Gaussian Inc. Wallingford CT 2009.

[45] Rick A. Kendall and Herbert A. Früchtl. The impact of the resolution of the identity approximate integral method on modern ab initio algorithm development. *Theoretical Chemistry Accounts: Theory, Computation, and Modeling (Theoretica Chimica Acta)*, 97(1-4):158–163, October 1997.

[46] TURBOMOLE V6.4 2012, a development of University of Karlsruhe and Forschungszentrum Karlsruhe GmbH, 1989-2007, TURBOMOLE GmbH, since 2007; URL: http://www.turbomole.com/.

[47] S. J. Clark, M. D. Segall, C. J. Pickard, P. J. Hasnip, M. J. Probert, K. Refson, and M.C. Payne. First principles methods using CASTEP. *Z. Kristall.*, 220:567–570, 2005.

[48] Marcus Hanwell, Donald Curtis, David Lonie, Tim Vandermeersch, Eva Zurek, and Geoffrey Hutchison. Avogadro: An advanced semantic chemical editor, visualization, and analysis platform. *Journal of Cheminformatics*, 4(1):17, 2012.

[49] Persistence of Vision Pty. Ltd., Persistence of Vision Raytracer (version 3.6), URL: http://www.povray.org/, 2004.

[50] W Humphrey, A Dalke, and K Schulten. VMD – Visual Molecular Dynamics. *Journal of Molecular Graphics*, 14:33–38, 1996.

[51] Guido van Rossum and Frank L Drake (ed). *Python Reference Manual*. PythonLabs, 2001.

[52] Bash (Bourne Again Shell), Free Software Foundation, URL: http://www.gnu.org/software/bash/.

[53] L. T. Reynolds and G. Wilkinson. π-cyclopentadienyl compounds of uranium-IV and thorium-IV. *Journal of Inorganic and Nuclear Chemistry*, 2:246–253+, 1956.

[54] Nikolas Kaltsoyannis and Bruce E. Bursten. Electronic structure of f^1 lanthanide and actinide complexes. Part 2. Non-relativistic and relativistic calculations of the ground state electronic structures and optical transition energies of $[Ce(\eta-C_5H_5)_3]$, $[Th(\eta-C_5H_5)_3]$ and $[Pa(\eta-C_8H_8)_2]$. *Journal of Organometallic Chemistry*, 528:19–33+, 1997.

[55] Kenneth L. Nash. A Review of the Basic Chemistry and Recent Developments in Trivalent f-Elements Separations. *Solvent Extraction and Ion Exchange*, 11(4):729–768, May 1993.

[56] Mark P. Jensen and Andrew H. Bond. Comparison of Covalency in the Complexes of Trivalent Actinide and Lanthanide Cations. *Journal of the American Chemical Society*, 124(33):9870–9877, July 2002.

[57] Mathieu Roger, Noémi Barros, Thérèse Arliguie, Pierre Thuéry, Laurent Maron, and Michel Ephritikhine. $U(SMes\cdot)_n$, (n = 3, 4) and $Ln(SMes\cdot)_3$ (Ln = La, Ce, Pr, Nd) – Lanthanide(III)/Actinide(III) Differentiation in Agostic Interactions and an Unprecedented η3 Ligation Mode of the Arylthiolate Ligand, from X-ray Diffraction and DFT Analysis. *Journal of the American Chemical Society*, 128(27):8790–8802, June 2006.

[58] Andrew J. Gaunt, Brian L. Scott, and Mary P. Neu. U(IV) Chalcogenolates Synthesized via Oxidation of Uranium Metal by Dichalcogenides. *Inorganic Chemistry*, 45(18):7401–7407, August 2006.

[59] Laurence Petit, Laurent Joubert, Pascale Maldivi, and Carlo Adamo. A Comprehensive Theoretical View of the Bonding in Actinide Molecular Complexes. *Journal of the American Chemical Society*, 128(7):2190–2191, February 2006.

[60] Jerzy Narbutt and Wojciech P. Oziminski. Selectivity of bis-triazinyl bipyridine ligands for americium(iii) in Am/Eu separation by solvent extraction. Part 1. Quantum mechanical study on the structures of BTBP complexes and on the energy of the separation. *Dalton Transactions*, 41(47):14416–14424, 2012.

[61] Nikolas Kaltsoyannis. Does Covalency Increase or Decrease across the Actinide Series? Implications for Minor Actinide Partitioning. *Inorganic Chemistry*, June 2012.

[62] Bruce E. Bursten and Richard J. Strittmatter. Cyclopentadienyl-Actinide Complexes: Bonding and Electronic Structure. *Angewandte Chemie - International Edition*, 30(9):1069–1085, September 1991.

[63] Ionut Prodan, Gustavo Scuseria, and Richard Martin. Covalency in the actinide dioxides: Systematic study of the electronic properties using screened hybrid density functional theory. *Physical Review B*, 76(3):033101+, July 2007.

[64] Udo Radius and Frank Breher. To Boldly Pass the Metal-Metal Quadruple Bond. *Angewandte Chemie International Edition*, 45(19):3006–3010, 2006.

[65] Kai K. Lange, E. I. Tellgren, M. R. Hoffmann, and T. Helgaker. A Paramagnetic Bonding Mechanism for Diatomics in Strong Magnetic Fields. *Science*, 337(6092):327–331, July 2012.

[66] Santiago Alvarez, Roald Hoffmann, and Carlo Mealli. A Bonding Quandary – or – A Demonstration of the Fact That Scientists Are Not Born With Logic. *Chemistry - A European Journal*, 15(34):8358–8373, 2009.

[67] F. Cortesguzman and R. Bader. Complementarity of QTAIM and MO theory in the study of bonding in donor?acceptor complexes. *Coordination Chemistry Reviews*, 249(5-6):633–662, March 2005.

[68] I. Mayer. Charge, bond order and valence in the AB initio SCF theory. *Chemical Physics Letters*, 97(3):270–274, May 1983.

[69] W. Küchle, M. Dolg, H. Stoll, and H. Preuss. Energy-adjusted pseudopotentials for the actinides. Parameter sets and test calculations for thorium and thorium monoxide. *Journal of Chemical Physics*, 100(10):7535–7542, 1994.

[70] Björn O. Roos, Roland Lindh, Per-Åke Malmqvist, Valera Veryazov, and Per-Olof Widmark. New relativistic ANO basis sets for actinide atoms. *Chemical Physics Letters*, 409(4-6):295–299, June 2005.

[71] R. Krishnan, J. S. Binkley, R. Seeger, and J. A. Pople. Self-consistent molecular orbital methods. XX. A basis set for correlated wave functions. *Journal of Chemical Physics*, 72(1):650–654, 1980.

[72] Dominique Guillaumont. Quantum Chemistry Study of Actinide(III) and Lanthanide(III) Complexes with Tridentate Nitrogen Ligands. *Journal of Physical Chemistry A*, 108(33):6893–6900, July 2004.

[73] Matthew J. Tassell and Nikolas Kaltsoyannis. Covalency in $AnCp_4$ (An = Th-Cm): a comparison of molecular orbital, natural population and atoms-in-molecules analyses. *Dalton Transactions*, 39(29):6719+, 2010.

[74] R. D. Shannon. Revised effective ionic radii and systematic studies of interatomic distances in halides and chalcogenides. *Acta Crystallographica Section A*, 32(5):751–767, September 1976.

[75] P. Macchi. Chemical bonding in transition metal carbonyl clusters: complementary analysis of theoretical and experimental electron densities. *Coordination Chemistry Reviews*, 238-239:383–412, March 2003.

[76] Ian Kirker and Nikolas Kaltsoyannis. Does covalency really increase across the 5f series? A comparison of molecular orbital, natural population, spin and electron density analyses of $AnCp_3$ (An = Th-Cm; Cp = $\eta_5-C_5H_5$). *Dalton Transactions*, 40(1):124+, 2011.

[77] David D. Schnaars, Andrew J. Gaunt, Trevor W. Hayton, Matthew B. Jones, Ian Kirker, Nikolas Kaltsoyannis, Iain May, Sean D. Reilly, Brian L. Scott, and Guang Wu. Bonding trends traversing the tetravalent actinide series: Synthesis, structural, and computational analysis of An(IV)(^{Ar}acnac)$_4$ complexes (An = Th, U, Np, Pu; ^{Ar}acnac = ArNC(Ph)CHC(Ph)O; Ar = 3,5−tBu$_2$−C$_6$H$_3$). *Inorganic Chemistry*, 51(15):8557–8566, July 2012.

[78] David D. Schnaars, Enrique R. Batista, Andrew J. Gaunt, Trevor W. Hayton, Iain May, Sean D. Reilly, Brian L. Scott, and Guang Wu. Differences in actinide metal-ligand orbital interactions: comparison of U(IV) and Pu(IV) beta-ketoiminate N,O donor complexes. *Chemical Communications*, 47(27):7647+, 2011.

[79] Stefan G. Minasian, Jamin L. Krinsky, and John Arnold. Evaluating *f*-Element Bonding from Structure and Thermodynamics. *Chemistry - A European Journal*, 17(44):12234–12245, October 2011.

[80] Dimitrios A. Pantazis and Frank Neese. All-Electron Scalar Relativistic Basis Sets for the Actinides. *Journal of Chemical Theory and Computation*, 7(3):677–684, February 2011.

[81] Alexey A. Sokol, Samuel A. French, Stefan T. Bromley, Catlow, Huub J. J. van Dam, and Paul Sherwood. Point defects in ZnO. *Faraday Discussions*, 134:267–282, 2007.

[82] Ionut Prodan and Gustavo E Scuseria. Private Communication, 2011.

[83] Chérif F. Matta, Jesús Hernández-Trujillo, Ting-Hua Tang, and Richard F. W. Bader. Hydrogen–Hydrogen Bonding: A Stabilizing Interaction in Molecules and Crystals. *Chemistry - A European Journal*, 9(9):1940–1951, 2003.

[84] S. Jenkins and I. Morrison. The chemical character of the intermolecular bonds of seven phases of ice as revealed by ab initio calculation of electron densities. *Chemical Physics Letters*, 317(1-2):97–102, January 2000.

[85] Josefredo R. Pliego and José M. Riveros. Theoretical Calculation of pK_a Using the Cluster-Continuum Model. *Journal of Physical Chemistry A*, 106(32):7434–7439, July 2002.

[86] Casey P. Kelly, Christopher J. Cramer, and Donald G. Truhlar. Adding Explicit Solvent Molecules to Continuum Solvent Calculations for the Calculation of Aqueous Acid Dissociation Constants. *Journal of Physical Chemistry A*, 110(7):2493–2499, February 2006.

[87] Ivan Infante, Bas van Stralen, and Lucas Visscher. A QM/MM study on the aqueous solvation of the tetrahydroxouranylate $[UO_2(OH)_4]^{2+}$ complex ion. *Journal of Computational Chemistry*, 27(11):1156–1162, 2006.

[88] Daniel Hagberg, Gunnar Karlström, Björn O. Roos, and Laura Gagliardi. The Coordination of Uranyl in Water – A Combined Quantum Chemical and Molecular Simulation Study. *Journal of the American Chemical Society*, 127(41):14250–14256, September 2005.

[89] Daniel Hagberg, Eugeniusz Bednarz, Norman M. Edelstein, and Laura Gagliardi. A Quantum Chemical and Molecular Dynamics Study of the Coordination of Cm(III) in Water. *Journal of the American Chemical Society*, 129(46):14136–14137, October 2007.

[90] Raymond Atta-Fynn, Donald F. Johnson, Eric J. Bylaska, Eugene S. Ilton, Gregory K. Schenter, and Wibe A. de Jong. Structure and Hydrolysis of the U(IV), U(V), and U(VI) Aqua Ions from Ab Initio Molecular Simulations. *Inorganic Chemistry*, 51(5):3016–3024, February 2012.

[91] Regla Ayala, Riccardo Spezia, Rodolphe Vuilleumier, José M. Martínez, Rafael R. Pappalardo, and Enrique Sánchez Marcos. An Ab Initio Molecular Dynamics Study on the Hydrolysis of the Po(IV) Aquaion in Water. *The Journal of Physical Chemistry B*, 114(40):12866–12874, October 2010.

[92] Steven D. Conradson, Ilham Al Mahamid, David L. Clark, Nancy J. Hess, Eric A. Hudson, Mary P. Neu, Phillip D. Palmer, Wolfgang H. Runde, and C. Drew Tait.

Oxidation state determination of plutonium aquo ions using X-ray absorption spectroscopy. *Polyhedron*, 17(4):599–602, January 1998.

[93] Volker Neck and J. I. Kim. Solubility and hydrolysis of tetravalent actinides. *Radiochimica Acta*, 89(1_2001):1+, January 2001.

[94] Regla Ayala, José M. Martínez, Rafael R. Pappalardo, Adela Muñoz Páez, and Enrique Sánchez Marcos. Po(IV) Hydration: A Quantum Chemical Study. *Journal of Physical Chemistry B*, 112(17):5416–5422, May 2008.

[95] Regla Ayala, José M. Martínez, Rafael R. Pappalardo, Adela Muñoz Páez, and Enrique Sánchez Marcos. General Quantum-Mechanical Study on the Hydrolysis Equilibria for a Tetravalent Aquaion: The Extreme Case of the Po(IV) in Water. *Journal of Physical Chemistry B*, 113(2):487–496, January 2009.

[96] A. Kerridge and N. Kaltsoyannis. The coordination of Sr2+ by hydroxide: a density functional theoretical study. *Dalton Transactions*, 40(42):11258–11266, 2011.

[97] Andrew Kerridge and Nikolas Kaltsoyannis. Quantum Chemical Studies of the Hydration of Sr^{2+} in Vacuum and Aqueous Solution. *Chemistry - A European Journal*, 17(18):5060–5067, 2011.

[98] Viktor N. Staroverov, Gustavo E. Scuseria, Jianmin Tao, and John P. Perdew. Comparative assessment of a new nonempirical density functional: Molecules and hydrogen-bonded complexes. *The Journal of Chemical Physics*, 119(23):12129–12137, 2003.

[99] Malte Von Arnim and Reinhart Ahlrichs. Performance of parallel TURBOMOLE for density functional calculations. *Journal of Computational Chemistry*, 19(15):1746–1757, 1998.

[100] Florian Weigend and Reinhart Ahlrichs. Balanced basis sets of split valence, triple zeta valence and quadruple zeta valence quality for H to Rn: Design and assessment of accuracy. *Physical Chemistry Chemical Physics*, 7(18):3297–3305, 2005.

[101] Jeffrey P. Merrick, Damian Moran, and Leo Radom. An Evaluation of Harmonic Vibrational Frequency Scale Factors. *Journal of Physical Chemistry A*, 111(45):11683–11700, October 2007.

[102] J. Peter Guthrie. Use of DFT Methods for the Calculation of the Entropy of Gas Phase Organic Molecules – An Examination of the Quality of Results from a Simple Approach. *Journal of Physical Chemistry A*, 105(37):8495–8499, August 2001.

[103] M. V. Zamoryanskaya and B. E. Burakov. Feasibility Limits in Using Cerium as a Surrogate for Plutonium Incorporation in Zircon, Zirconia and Pyrochlore. *MRS Online Proceedings Library*, 663, 2000.

[104] M. Tanaka, G. Girard, R. Davis, A. Peuto, and N. Bignell. Recommended table for the density of water between 0 řC and 40 řC based on recent experimental reports. *Metrologia*, 38(4):301+, March 2003.

[105] John P. Perdew, Kieron Burke, and Matthias Ernzerhof. Generalized Gradient Approximation Made Simple. *Physical Review Letters*, 77(18):3865–3868, October 1996.

[106] I-Chun Lin, Ari P. Seitsonen, Ivano Tavernelli, and Ursula Rothlisberger. Structure and Dynamics of Liquid Water from ab Initio Molecular Dynamics – Comparison of BLYP, PBE, and revPBE Density Functionals with and without van der Waals Corrections. *Journal of Chemical Theory and Computation*, May 2012.

[107] Samuel O. Odoh and Georg Schreckenbach. Theoretical Study of the Structural Properties of Plutonium(IV) and (VI) Complexes. *Journal of Physical Chemistry A*, 115(48):14110–14119, October 2011.

[108] Douglas A. Gibson, Irina V. Ionova, and Emily A. Carter. A comparison of Car-Parrinello and Born-Oppenheimer generalized valence bond molecular dynamics. *Chemical Physics Letters*, 240(4):261–267, June 1995.

[109] W. C. Swope, H. C. Andersen, P. H. Berens, and K. R. Wilson. A computer-simulation method for the calculation of equilibrium-constants for the for-

mation of physical clusters of molecules - application to small water clusters. *J. Chem. Phys.*, 76:637–649, 1982.